Hadron Single- and Multiparticle Measurements to Search for Phase Transitions in Ultrarelativistic Pb+Pb Collisions

A Dissertation Presented

by

Mikhail Leonidovich Kopytine

to

The Graduate School

in Partial Fulfillment of the Requirements

for the Degree of

Doctor of Philosophy

in

Physics

State University of New York
at
Stony Brook

August 2001

State University of New York
at Stony Brook

The Graduate School

Mikhail Leonidovich Kopytine

We, the dissertation committee for the above candidate for the Doctor of Philosophy degree, hereby recommend acceptance of the dissertation.

Prof. Barbara Jacak (Thesis Advisor)
SUNY at Stony Brook

Prof. Robert McCarthy (Committee Chair)
SUNY at Stony Brook

Prof. Edward Shuryak
SUNY at Stony Brook

Dr. Dmitri Kharzeev
BNL

This dissertation is accepted by the Graduate School.

Graduate School

Abstract of the Dissertation

Hadron Single- and Multiparticle Measurements to Search for Phase Transitions in Ultrarelativistic Pb+Pb Collisions

by

Mikhail Leonidovich Kopytine

Doctor of Philosophy

in

Physics

State University of New York at Stony Brook

2001

Hadron production in the 158 A GeV/c Pb+Pb collisions at the CERN SPS is studied in the NA44 Experiment. Yields and differential distributions of K^+, K^-, π^+, π^- in transverse kinetic energy and rapidity are measured around the center-of-mass rapidity. A considerable enhancement of K^+ production per π is observed, as compared to $p+p$ collisions at this energy. To illustrate the importance of secondary hadron rescattering as an enhancement mechanism, we compare strangeness production at the SPS and AGS with predictions of the transport model RQMD.

A Si pad array covering pseudorapidity $1.5 < \eta < 3.3$ is used for an event-by-event study of the interactions. We apply a multiresolution analysis, based on a Discrete Wavelet Transformation, to probe the texture of particle distributions event-by-event, allowing simultaneous localization of features in space and scale. Scanning a broad range of multiplicities, we search for signals of clustering and of critical behaviour in the power spectra of local density

fluctuations. The data are compared with detailed simulations of detector response, using heavy ion event generators, and with a reference sample created via event mixing. An upper limit is set on the probability and magnitude of dynamical fluctuations.

Contents

List of Figures . . . . . **xiii**

List of Tables . . . . . **xv**

Acknowledgements . . . . . **xvi**

1 Introduction **1**

1.1 Multiparticle production and the strong interaction: a prehistory of the relationship 1

1.2 Relativistic collisions of heavy ions 2

2 The NA44 Experiment **5**

2.1 The General Concept 5

2.2 Beam 6

2.3 Target 7

2.4 Trigger 7

2.4.1 Valid beam condition (VB) and beam counting 8

2.4.2 Trigger detector of charged particle multiplicity ($T0$) . 8

2.4.3 Multiplicity trigger ($MUL1$) 9

2.4.4 Cherenkov veto trigger ($\bar{C}1 \cdot \bar{C}2$ and $\bar{C}2$) 9

2.4.5 Use of the trigger modes 10

2.5 Scalers 10

2.6 The Si pad detector 11

2.7 Spectrometer "optics" and acceptance. 13

2.8 Means of particle identification 13

2.8.1 Tracking and time of flight 13

2.8.2 The Cherenkov counters 16

2.8.3 The Uranium Calorimeter (UCAL) 16

2.9 Readout and Data Acquisition 17

3 Technique of the NA44 single particle analysis **19**
3.1 Acceptance correction 19
3.1.1 Introduction and definitions 19
3.1.2 How to extract the one-dimensional distributions . . . 21
3.1.3 Corrections for the inefficient hodoscope slats 23
3.1.4 Acceptance correction for the non-identified tracks 24
3.1.5 Imperfections of the acceptance correction and the effects thereof 24
3.1.6 Collimator-related uncertainties 25
3.2 Determination of the trigger centrality 26
3.2.1 The problem of absolute normalization 27
3.2.2 Role of T0 28
3.2.3 Role of *MUL1* 29
3.2.4 General idea of the procedure 30
3.2.5 How to use the Si pad array 30
3.2.6 Si – spectrometer acceptance matching 33
3.2.7 $dN/d\eta$ matching: Si vs spectrometer 34
3.2.8 Runs with Cherenkov veto 37
3.2.9 Correction for the consequences of radiation damage in Si 38
3.2.10 Results, systematic uncertainties, and conclusions. . . . 41
3.3 Track identification 44
3.3.1 Double beam cut 44
3.3.2 Track confidence level cut 44
3.3.3 Pad Chamber in the trigger 45
3.4 Pion identification 46
3.4.1 Time of flight in pion identification 46
3.4.2 UCAL calibration 47
3.4.3 Correcting for the electron veto inefficiency. 49
3.4.4 Counting pions in the strong field setting. 50
3.5 Kaon identification 51
3.5.1 Time of flight in kaon identification. 52
3.5.2 Correcting for pion/electron veto inefficiency 53
3.6 Summary of the systematic uncertainties 56

4 Inclusive single particle results for π and K. Their meaning. 57

4.1 Strangeness as a deconfinement signature 57

4.2 Hadrochemistry 59

4.3 Subtleties and controversies related to the strangeness signature 60

4.4 What the data say 61

4.5 Conclusion from NA44 strangeness measurements 70

5 Technique for event-by-event multiparticle texture analysis using the NA44 Si pad array 71

5.1 Data sample and data reduction 72

5.2 δ-electrons and the Si detector 73

5.3 Amplitude calibration of the Si channels 74

5.4 Geometrical alignment of the detector 78

5.4.1 Formulation of the problem 78

5.4.2 Solution 79

5.5 Cross-talk analysis 83

5.5.1 Sources of cross-talk 83

5.5.2 Channel wiring and numbering 83

5.5.3 The covariance matrix approach 84

5.5.4 Cross-talk evaluation: results and discussion 87

5.5.5 Cross-talk correction for the multiplicity 89

5.5.6 The double differential multiplicity distribution 91

5.6 Discrete Wavelet Transform power spectrum analysis of local fluctuations 93

5.6.1 The power spectrum – a way to accumulate texture information 93

5.6.2 Static and dynamic texture. Event mixing as a way to subtract the static contribution. 95

5.7 Analysis of background effects 97

5.7.1 Sources of background 97

5.7.2 Background subtraction 98

5.8 GEANT-based Monte Carlo simulation of the detector response 99

5.9 Systematic errors 100

6 Results of the event-by-event multiparticle texture analysis and their meaning **104**
6.1 The DWT texture correlation 104
6.2 The multifireball event generator. 107
6.2.1 Physics 108
6.2.2 Mathematics. 111
6.3 Sensitivity of the method 112
6.4 Discussion: First Order Phase Transition 114
6.5 Discussion: Second Order Phase Transition 116

7 Conclusions **118**

A Re-calibrating UCAL to correct for the light absorbtion. . **126**

B Subtracting background effects in the DWT power spectra. 128

C Calculus of covariances **130**

D Generating sequences of random numbers with a fixed sum. 131

List of Figures

2.1 The NA44 spectrometer during the Pb beam running. The T0 and the Si pad array are in the target area and are too small to be seen on this scale. The target area is shown in Fig. 2.2 . . . 6

2.2 NA44 multiplicity detector complex: a) the lead target, the Si pad array and the T0 scintillators; b) the setup exposed to a simulated RQMD Pb+Pb event. 12

2.3 Acceptance area of the NA44 spectrometer in the laboratory rapidity y and transverse momentum p_T. Top: in the weak field mode; bottom: in the strong field mode. 14

2.4 Means of particle identification in the weak field settings . . . 15

2.5 Means of particle identification in the strong field settings . . 15

3.1 Understanding the collimator-related uncertainty in the acceptance-corrected pion dN/dy. The horizontal bars show the extent of the fiducial p_y window used. In this plot, other corrections were fixed at the values they had when the study was undertaken. 26

3.2 dN/dy distributions for negative hadrons: solid and open points – from NA49 measurements [41]; the histogram – from RQMD events of comparable centrality. 32

3.3 Determination of the trigger centrality by matching the Si and spectrometer multiplicity data. The multiplicity comparison is done withing the same multiplicity classes based on T0 amplitude, see text. 35

3.4 Left: correlation between $dN/d\eta$ obtained by charged track counting in the spectrometer and fired pad counting in the Si, found to be the best for a particular spectrometer setting. Right: positions of the multiplicity bins of the left plot along the "diagonalized" and normalized T0 amplitude. 36

3.5 χ^2/NDF between actual correlations and the one expected on the basis of acceptance simulation, vs the number of points involved, for three different centralities. 37

3.6 Illustration of the Si radiation damage correction algorithm in case of the 4GeV negative low angle setting, 4% centrality sample. From left to right, from top to bottom: SI ADC sum vs number of hits for the left and right parts of the detector in the valid beam run, with the non-interaction cut shown by the solid line; non-interaction cut on T0 signals in the valid beam run ; distribution of the number of Si noise hits in the valid beam run with the non-interaction cut; the "dirty" number of charged tracks in the physics run; the "purified" number of charged tracks. See text of Subsection 3.2.9 40

3.7 Comparison of the average charged track multiplicities measured independently by the left and right sides of the Si detector in the runs with different field sign. See text of Subsection 3.2.10. 42

3.8 Track confidence level distribution in the positive strong field, high angle, pion trigger setting. Top: confidence level distribution in X. Bottom: confidence level distribution in Y. 45

3.9 $N(\bar{C}2)/N(C2)$ (see text of subsection 3.4.3) as a function of $UCHAD/UCEM$ for the weak field, high angle, positive polarity setting. 50

3.10 Correcting for the Cherenkov veto inefficiency in the strong field case, 4% most central events. The number of rejected kaons is evaluated by subtracting the clean pion m^2 line shape scaled by a proper multiplier Υ. $+$ = all vetoed tracks $dN_{lost}/\,dm^2$; $\diamond$ = ratio of the pure pion line $dN_{clean,light}/\,dm^2$ to the "all vetoed tracks" distribution, $\circ$(also in the insert) = $dN(K+p)_{lost}/\,dm^2$ obtained as "all vetoed tracks" minus Υ - scaled pion line (see Eq. 3.31). The shaded histogram shows the m^2 distribution of K/p tracks which were not vetoed. 55

4.1 Measured transverse kinetic energy distributions of positive and negative kaons for the 4% and 10% most central of Pb+Pb collisions. Two spectrometer angle settings meet at $m_T - m = 0.35$ GeV. The fits follow the form $1/m_T\, dN/\,dm_T \propto exp(-m_T/T)$, where $m_T = (m^2 + p_T^2)^{1/2}$. y ranges of the fits are given in Table 2 and are indicated by the horizontal errorbars in the inserts. RQMD predictions for $|y - y_{CM}| < 0.6$ (i.e., within NA44 acceptance) are shown as histograms. 63

4.2 Comparison of measured charged kaon and pion yields with RQMD predictions. The vertical error bars indicate statistical and systematic errors, added in quadrature; the horizontal ones – y boundaries of the acceptance used for p_T integration in each spectrometer setting. Open symbols represent spectrometer settings whose y position is shown mirror-reflected around midrapidity (2.92); their solid analogs – the actual settings. RQMD: solid line – standard mode, dashed line – no rescattering. 65

4.3 K/π ratios in symmetric systems at midrapidity $|y - y_{CM}| \leq |y_{proj} - y_{targ}|/8$. The solid line shows full solid angle K/π in $p + p$ collisions from the interpolation [59]. The data points from other experiments result from an interpolation in y to the midrapidity interval. The E866 data points [60] are also interpolated in the number of participants, for comparison with the SPS data. 66

4.4 Comparison of measurements with RQMD predictions: K^+/π^+ ratio in the specified rapidity interval around mid-rapidity, as a function of the product of pion and proton dN/dy, obtained in the same rapidity interval, in symmetric collisions. $\diamond$ – E866 AuAu, $\bullet$ – NA44 SS, $\circ$ – NA44 PbPb. RQMD: solid line – standard mode, dashed line – no rescattering. 67

5.1 A typical calibration fit. Channel 1. 74

5.2 Example of a monitoring plot used in the course of the analysis to understand the alignment procedure and the alignment quality. The color (or gray level) corresponds to the pad multiplicity. No misalignment correction is applied. The horizontal lines connect centers of the pads with $\Delta_{i,j}$ sufficiently small for the pairs to be used in formula 5.20 (compare with Fig. 5.3). Run 3192. The δ-contaminated part of the detector is not shown. 80

5.3 Another example of a monitoring plot used in the course of the analysis to understand the alignment procedure and the alignment quality. The color (or gray level) corresponds to the pad occupancy. A misalignment correction is applied. One can see how both the acceptances of the pads and their (double differential !) multiplicities are modified. The horizontal lines connect centers of the pads with $\Delta_{i,j}$ sufficiently small for the pairs to be used in formula 5.20 (compare with Fig. 5.2). Run 3192. The δ-contaminated part of the detector is not shown. 81

5.4 Alignment results for run 3192. The axes show detector's offsets in X and Y in cm. MIGRAD (see [79]) minimization converged at point $(X, Y) = (0.110 \pm 0.019, 0.031 \pm 0.009)$ cm. The dotted lines cross at the estimated minimum. The contour and the errorbar estimates quoted correspond to the unit deviation of the function from the minimum. 82
5.5 Covariance matrix cov(a_i,a_j) of the Si pad array in run 3192. The color scale is logarithmic, units are MeV^2. The matrix is symmetric. Increased elements next to the main diagonal indicate the adjacent neighbour cross-talk. Non-uniform overall landscape is due to the beam offset and the beam's geometrical profile. The white diagonals represent the autocorrelation discussed in subsection 5.5.3. The "cross" in the middle corresponds to dead channels. 85
5.6 A distribution of the covariance matrix elements. Run 3192. Information on the cross-talk magnitude is in the distance between the third and fourth peaks (counting from left). 87
5.7 A distribution of the covariance matrix elements, that represent correlations between adjacent channels. Run 3192. Same binning as on Fig. 5.6; on that figure, this is seen as the third peak. 88
5.8 An example of a pathological event in the Si pad array. Top panel: the amplitude array. Sector number – horizontal axis, ring number – vertical axis. The δ-free acceptance, used in the analysis, is limited to sectors from 9 through 24. Sector 11 is affected by cross-talk. Sector 25 is dead. Bottom panel: amplitude distribution from this event only. It looks quite normal. The pedestal peak is fine, single and double hit peaks are clearly seen. 90
5.9 A distribution of the covariance matrix elements, that represent correlations between adjacent *inner* channels of sectors. Matrix elements involving dead channels are not shown. Run 3192. . 91
5.10 Double differential multiplicity distributions of charged particles plotted as a function of azimuthal angle ζ (with different symbols representing different rings) and of pseudorapidity η (with different symbols representing different sectors). The ζ and η are in the *aligned* coordinates. 92
5.11 Power spectra of 7×10^3 events in the multiplicity bin $326 < dN/d\eta < 398$. ◯ – true events, △ – mixed events, □ – the average event. 95

6.1 Multiplicity dependence of the texture correlation. ◯ – the NA44 data, • – RQMD. The boxes show the systematic errors vertically and the boundaries of the multiplicity bins horizontally; the statistical errors are indicated by the vertical bars on the points. The rows correspond to the scale fineness m, the columns – to the directional mode λ (which can be diagonal $\zeta\eta$, azimuthal ζ, and pseudorapidity η). 105
6.2 Confidence coefficient as a function of the fluctuation strength. RMS_{mix} denotes $\sqrt{\langle P^{\lambda}(1)^2_{mix} - \langle P^{\lambda}(1)_{mix}\rangle^2\rangle}$. This is the coarsest scale. 106
6.3 dN/dy distribution of charged particles in the multifireball event generator in four *individual events* with different number of fireballs: △ – 2 fireballs, □ – 4 fireballs, ◇ – 8 fireballs, ◯ – 16 fireballs. One can see how the texture becomes smoother as the number of fireballs increases. We remind the reader that the detector's active area covers 2π azimuthally and pseudorapidity 1.5 to 3.3. In general, acceptance limitations make it more difficult to detect dynamic textures. 109
6.4 dN/dy from negative hadrons obtained in 5% most central events of the multifireball event generator with different clustering parameter N_{ch}/fireball. 111
6.5 Coarse scale η texture correlation in the NA44 data, shown by ◯ (from the top right plot of Figure 6.1), is compared with that from the multifireball event generator for three different fireball sizes. Detector response is simulated. The boxes represent systematic errorbars (see caption to Fig. 6.1). 113

List of Tables

2.1 Threshold momenta (GeV/c) of common charged particles for $C1$ and $C2$. 10

2.2 Functions of the Cherenkov detectors in the trigger for various momentum settings 10

3.1 Parameters of the multi-temperature fits to the transverse kinetic energy distributions of pions. See Section 3.1.2, Eq. 3.15. The fitting range is $0 < k_T < 1.5GeV$ 23

3.2 The estimated fraction of events that do not create tracks in the spectrometer. It has been obtained according to the Poissonian law, $P(0) \simeq \exp(-2P(2)/P(1)$, based on the DST information. 29

3.3 RQMD-generated factors for acceptance matching. The following acceptance intervals were used. For the Si: $\eta_{min} = 1.5$, $\eta_{max} = 3.3$. For the spectrometer: in the low angle setting, $\eta_{min} = 3.6$, $\eta_{max} = 4.4$. In the high angle setting, $\eta_{min} = 2.6$, $\eta_{max} = 3.1$. 34

3.4 Radiation damage correction. The factors listed here are applied directly to dN/dy. 41

3.5 Trigger centrality c of the physics settings. 43

3.6 Corrections for the PC in the trigger. "1" is used when PC was not part of the trigger. See section 3.3.3. 46

3.7 Summary of conditions used to identify a track as a π (PID cuts). The "$4\pi^-$high" setting was split in two because of different hodoscope calibrations. The a and b parameters are used to specify a slat-dependent hodoscope cut: $H3TOF < H3SLAT \times a + b$, where $H3TOF$ is time-of-flight, $H3SLAT$ is the slat number. Words "see text" refer to Subsection 3.4.4. The fields are left blank when a device was not used to apply a cut for the π identification. 47

3.8 Multiplicative corrections to the π yields related to the process of particle identification for the samples of top 10% and top 4% centrality. 51
3.9 Summary of conditions used to identify a track as a K (PID cuts). The "$8K^+$high" setting was split in two because of different hodoscope calibrations. The a and b parameters are used to specify a slat-dependent hodoscope cut: $H3TOF < H3SLAT \times a + b$, where $H3TOF$ is time-of-flight, $H3SLAT$ is the slat number. The fields are left blank when a device was not used to apply a cut for the π identification. 52
3.10 Corrections to the K yields related to the process of particle identification for the samples of top 10% and top 4% centrality. 53
3.11 Summary of fractional systematic errors to the normalized yields. Positive kaons in the weak field high angle spectrometer setting are chosen as "representative". Maximum and minimum uncertainties indicate the range; the overall systematic uncertainty was evaluated for each setting separately. 56

4.1 Inverse slope parameters T. 62
4.2 Particle distributions in rapidity for top 4% centrality. Every spectrometer setting provides an independent measurement. Settings overlapping in y are listed separately. Statistical and systematic errorbars are added in quadrature to form $\sigma(\,dN/\,dy)$ listed. 62

5.1 Data used in the Si analysis. 72
5.2 Sources of background texture (dynamic and static) and their treatment. The irreducible remainder estimate is quoted for diagonal texture correlation in the $326 < dN/\,d\eta < 398$ bin, and is expressed in the units of $\sigma^2/\langle dE_{MIP}\rangle^2$; see text for information on how it was obtained. 101

Acknowledgements

It is a pleasure to record here my gratitude to my thesis advisor, Professor Barbara Jacak, for the education, attention, support and inspiration I have been receiving from her during these years in the NA44 Experiment. I am grateful to Nu Xu for presenting an inspiring example of how to make an intellectual quest the highest priority in the ramified activities a modern experimentalist is engaged in, and to John Sullivan and Hubert van Hecke who exemplified professionalism. It goes without saying that the entire NA44 Collaboration (spokesperson Hans Bøggild, contact person Achim Franz), including people who contributed to its success before my time, shares credit for this work. I acknowledge the help received from Jerry Dodd in my work on the Uranium Calorimeter and the Si pad array, and Michael Murray's helpful information on various issues in the single particle analysis. Discussions and arguments with Ian Bearden were a good school of scientific communication. The faculty and staff members of the Stony Brook Relativistic Heavy Ion group, such as Tom Hemmick, Axel Drees, and Vlad Pantuev, without being NA44 members, had nevertheless a significant impact on my education, which I am pleased to acknowledge. Being at Stony Brook, I enjoyed the privilege to communicate with members of the renown Nuclear Theory group. It was Edward Shuryak who suggested the idea of the sensitivity study with the multifireball event generator. Conversations with Madappa Prakash must be noted for their fine enlightening value. During the second part of this thesis project which dealt with an innovative analysis technique, we received support (in form of discussions, advise, or sometimes just encouragement) from Nikos Antoniou, Igor Dremin, Edward Shuryak, Mikhail Stephanov, and Tom Trainor.

Chapter 1

Introduction

1.1 Multiparticle production and the strong interaction: a prehistory of the relationship

The history of multiparticle production as a concept dates back to 1930s, according to the accounts left by the contemporaries [1, 2]. In 1936 the Auger electron-photon showers, now known as extended air showers, were discovered, but the cascade theory of Bhabha and Heitler did not yet exist. It seemed probable that all the shower electrons are produced at very high energy in a single act. Wataghin[3] and Heisenberg [4] speculated that the quantum field theory might have a limit of validity and would break down at distances shorter than a certain value, which was supposed to be a hypothetical universal unit of length. For the energies beyond that limit, a strong growth of the interaction with increasing energy, such that the *perturbation theory would no longer hold*, would result in the multiparticle production in a single act. Once the Auger shower was interpreted as an electromagnetic cascade process, this idea was completely forgotten. This was before discovery of a pion (G.Lattes *et al.*, 1947), and little was known at that time about the field where this idea is relevant indeed – the physics of the strong, or hadronic interaction. However, the mental pattern that links multiparticle production and non-perturbative phenomena, established then, has survived up to now and its presence can be seen in the modern studies of strong interaction in the collisions of heavy nuclei.

1.2 Relativistic collisions of heavy ions

An ultrarelativistic collision of heavy ions presents a phenomenon whose most interesting features are conditioned by the large multitude of degrees of freedom involved, and yet offer an opportunity for the fundamental physics of the strong interaction to manifest itself. From a particle physicist's point of view, "Relativistic Heavy Ions are a complicated mess raised to the power of a complicated mess" (a statement ascribed to D. Perkins). Particle physicists are used to comparing their experimental measurements with predictions obtained from perturbative theories (electro-weak theory or perturbative QCD). However, the most interesting aspects of strong interaction can not be described perturbatively. Luckily, perturbative expansion is not the only successful problem-solving technique in quantum physics. An approach with a somewhat complimentary area of success is the quasi-classical (WKB) approximation. Therefore, in order to address phenomena undescribable perturbatively, it is only natural to turn to systems which look like "a complicated mess", but (due to the large size and high excitation of the system) are quasi-classical.

The very notion of a phase transition in such systems (a subject of intense experimental and theoretical investigation) is of (quasi)macroscopic, multiparticle nature. On the theoretical side, the multiparticle, quasi-macroscopic, quasi-classical view favours statistical, thermodynamical, or hydrodynamical descriptions. The choice of an adequate description is a particularly challenging problem since the conditions (size, energy density, identities of the particles) of the system change dramatically over a short interval of time. At the end of this dramatic change, the hadronic interactions cease and the system *freezes out* in a state of free expansion. The measurements are performed long after that.

The macroscopic quantities that figure in the interpretation sections of experimental papers (temperature T, chemical potential μ, velocity of collective flow) are derived (often in a model-dependent way, under simplifying assumptions, including that of equilibrium) from single- and double-particle observables – spectra, radius parameters obtained from the Hanbury-Brown – Twiss (HBT for short) interferometry[25], and yields. Truly multiparticle observables, defined on an event-by-event basis, are of paramount interest.

By *event-by-event* (EbyE for short) we will mean the kind of analysis where the quantity(ies) of interest can be extracted from a single event. Event mixing can be used to create artificial events which retain certain reproducible morphological features of real events, especially those arising due to effects related to the process of measurement, and are devoid of physical correlations.

In Spring 1999, when we started an event-by-event analysis in NA44 (presented in Chapters 5 and 6), certain examples of EbyE analyses in high energy hadron collisions existed in cosmic ray works [5, 2, 6], in *pp* collisions at ISR [7], and in the reaction plane determination and elliptic flow [8, 9, 10] analyses in heavy ion collisions. The recently published event-by-event analyses of the SPS [1] $Pb + Pb$ data either deal with a few events [11] or analyze properties of a large ensemble of events by comparing different ensemble averages based on a single observable (transverse momentum p_T) [12]. In the first case [11], the path taken is essentially that of imaging, with the question of accumulation of feature information from large sets of events remaining open. In the second case [12], the difficulty lies in the fact that the ensemble averages (such as any RMS global fluctuation) on a set of *post-freeze-out* events can hardly be regarded as representative of a *pre-freeze-out* history of those events, due to the dramatic non-stationarity of the open system, with a consequent lack of ergodicity. More importantly, any symmetry breaking breaks ergodicity as well [13], thus causing any ergodicity-based measure to lose logical ground and become hard to interpret precisely when it is expected to signal a QCD phase transition.

Therefore, we prefer to concentrate on *texture*, or *local fluctuation* observables, where a single event is self-sufficient to determine its own fluctuation content. The idea to search for critical behaviour in particle distributions in rapidity y [14, 15] was inspired by a Ginzburg-Landau type of multihadron production theory [14], where the hadronic field probability amplitude $\Pi(y)$ plays the role of an order parameter in a hadronization transition. Naturally, enhanced correlations of hadrons in y at the critical point would manifest critical fluctuations in the order parameter. Recently, Stephanov *et al.* [16] revitalized the interest in the topic by pointing to the possibility for a second order QCD phase transition point to be found under certain initial conditions within the reach of the today's experiments, emphasising the importance of scanning a broad range of energies and impact parameters and of critical fluctuations as a signature to look for.

Chapters 5 and 6 present a power spectrum analysis of event texture in pseudorapidity η and azimuthal angle ζ (2D) [2], based on a Discrete Wavelet Transformation (DWT)[17], and performed on a number of large event ensembles [3] sampled according to their multiplicity, thereby studying the impact

[1] SPS – Super Proton Synchrotron, located at CERN

[2] we denote azimuthal angle by ζ to reserve ϕ and ψ for the wavelet functions

[3] ... this is not the first DWT power spectrum analysis performed on experimental

parameter dependence of the observables. DWT quantifies contributions of different ζ and η scales into the overall event's texture, thus testing the possible large scale enhancement – a classical [18] experimental signature of patterns formed in the vicinity of a critical point. A DWT-based power spectrum estimator is known [19] to overcome the problems of finite size and varying mean density of a sample.

While considering the texture analysis a fascinating topic with a promising future, we paid the due tribute of respect to the more traditional single particle observables. This part of work was chronologically the first (1996-1999); its methods and results are covered in chapters 3 and 4. We concentrated on the measurement of charged pions and kaons in $Pb + Pb$ collisions at SPS. One of the signatures of the deconfinement phase transition is enhancement of strangeness (discussed in Section 4). Interactions between liberated gluons in the deconfined phase are predicted [20, 21, 22] to enhance the rate of strangeness production compared to the non-QGP scenarios. Being the lightest strange hadrons, kaons are expected to dominate the strange sector by virtue of canonical thermodynamics [23]. The observed kaon multiplicity yields information about the mechanism of strangeness production, hadronization and subsequent evolution in the hadron gas, before the gas becomes sufficiently dilute that the interactions cease. Inelastic hadronic rescattering can enrich the strangeness content of the system [24]. We will report the yields and distributions of charged kaons and pions measured by the NA44 Experiment, and discuss implications of these data on the physics of the above-mentioned hadronic processes.

---

data in the physics of high energy hadron collisions – to my knowledge, the first one was performed on a couple of JACEE cosmic ray events in work [6]. The scarce event statistics left the feature eduction potential of the DWT power spectrum underutilized. Another difference from our case is that only a 1D pseudorapidity-bound DWT was used in that work.

Chapter 2

The NA44 Experiment

2.1 The General Concept

In the design of fixed target heavy ion experiments, one can distinguish two opposite stratagems:

- Emphasize quality of a given set of measurements (resolution, cleanliness of particle identification). Sacrifice broadness of scope in order to fully concentrate on the selected measurements.
- Emphasize broadness of scope (acceptance, variety of identifiable particles). Sacrifice quality of measurements (resolution, quality of particle identification).

A clear awareness of one's stratagem, readiness to counteract its drawbacks and fully utilize its strengths is an essential prerequisite of success. The choice of a stratagem (or, in a mixed case, choice of a proportion of the mix) is driven by the experiment's goals. The goals of the NA44 Experiment have been:

- Hanbury-Brown–Twiss (for short, HBT) interferometry[25] with pions, kaons and protons, reaching a formulation as complex as 3D.
- Single particle spectra of pions, kaons, protons, antiprotons, deuterons, antideuterons, and even tritons. In particular, a study of low p_T features of the spectra around midrapidity.
- Measurements of the abundances of the above mentioned particles.

Thus ordered, the goals entail the design concept of an experiment, which follows the first stratagem: *a focusing spectrometer.* Focusing magnetic field provides for excellent momentum resolution, but can be effective only in a narrow

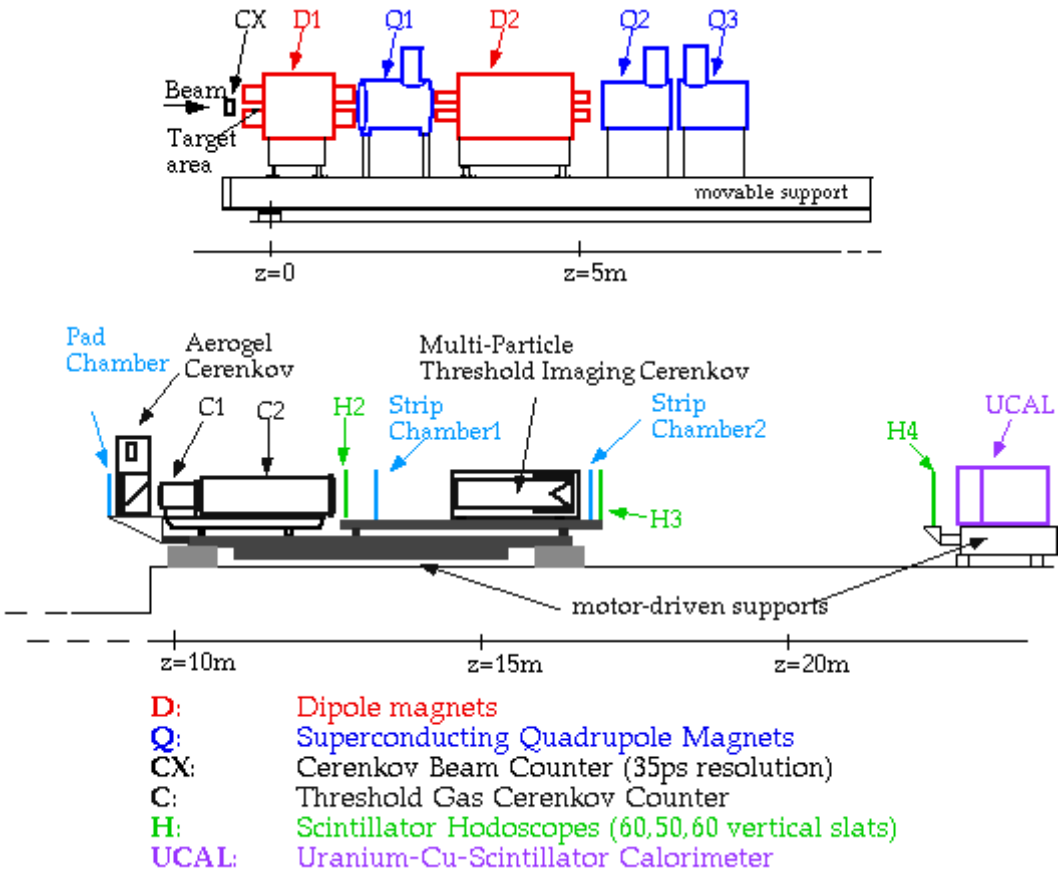

Figure 2.1: The NA44 spectrometer during the Pb beam running. The T0 and the Si pad array are in the target area and are too small to be seen on this scale. The target area is shown in Fig. 2.2

region of phase space. Hence the smallness of track multiplicity that enables clean particle identification using the relatively simple techniques based on time-of-flight and Cherenkov radiation.

2.2 Beam

The CERN SPS (Super Proton Synchrotron) delivered spills of Pb^{82+} ions accelerated up to the 158 GeV/c/nucleon momentum. NA44 was located in the H4 beam line. Geometrically, the Pb beam had a rectangular, vertically elongated cross-section of about 1mm×2mm [28]. The equipment for beam profile scanning was provided by the SPS, located in the beam channel and

included scintillating filaments and gas detector chambers. The beam was coming in 5 s long spills (bursts), and was collimated to obtain an intensity of, typically, several million particles per spill.

2.3 Target

In the Pb run, we used Pb targets made in the shape of a 1cm diameter disk of 1.15 g/cm^2 or 2.3 g/cm^2 thickness. Interaction probability in the target can be estimated, scaling the known [27] nuclear inelastic cross-section ($\sigma(pPb) = 1.77\ barn$) in proportion to the number of primary collisions between individual participants (1 for p, 208 for Pb): [1]

$$\frac{\sigma(PbPb)}{\sigma(pPb)} = \left(\frac{2 \times 208^{\frac{1}{3}}}{1^{\frac{1}{3}} + 208^{\frac{1}{3}}}\right)^2 \approx 2.93 \tag{2.1}$$

When the interaction cross-section σ is known, the interaction probability is $\sigma N_A d/\mu$, where d is target thickness in g/cm^2, N_A is the Avogadro's number, and μ is molar mass of the material in g/mol. For the two target thicknesses mentioned, the interaction probabilities would be, respectively, 1.7 and 3.4 %.

2.4 Trigger

The art of experiment is to make the equipment answer as accurately as possible the questions we ask, while being as insensitive as possible to what we deem irrelevant. Ability to identify the difference between what can be made irrelevant and what can not depends on the knowledge previously acquired, and is among the experimentalist's most precious qualifications. The purpose of a trigger is to allow the experiment to focus on the selected topic. An hierarchy of trigger conditions is maintained. In its turn, the hardware *trigger* (i.e. the permission to record the information from the equipment) itself forms the preliminary stage for a more complex off-line analysis. Its negative consequences can not be overcome off-line, but can only be corrected for, in which process the richness and complexity of the above-mentioned hierarchy plays the crucial role.

[1] With the normalization technique actually used, the accuracy of this estimate does not affect the accuracy of the normalized particle yields, and the estimate is given here for orientation only.

How important is the issue of a trigger ? The SPS delivers spills of particles with given momentum to the target. A typical duration of a spill is about 5 s, during which about 4×10^6 particles cross the target. A typical NA44 run used for single particle analysis lasts for about 100 spills, and records a tape with about 4×10^4 events. Having an interaction in the target is therefore roughly two orders of magnitude more frequent an event than writing a selected event to the tape. This means that by virtue of the NA44 trigger, these 4×10^4 events can be easily collected so that each of them contains a proton or a kaon, or a pion pair, or at least one charged particle of any identity. With some change in the numbers, but without difficulty, samples of kaon and proton pairs for correlation analysis can be obtained. This section explains how this is possible.

2.4.1 Valid beam condition (VB) and beam counting

A gaseous Cherenkov beam counter [29] and a geometrical veto scintillation counter provided a positive indication of a beam particle's passage through the target. This indication constituted the simplest possible form of an NA44 trigger, known as the *valid beam trigger*. The beam counter provided a 35 ps accurate start time reference for subsequent time of flight measurements via scintillating hodoscopes (see section 2.8.1). The beam count, provided by this detector, was needed to convert particle counts in the spectrometer into average particle yield for a given event centrality.

2.4.2 Trigger detector of charged particle multiplicity ($T0$)

Nuclei can collide at various impact parameters. To study the physics of phaser transitions, the maximal volume is desired. Consequently, experiments select collisions with small impact parameters, i.e. "central" or head-on collisions of nuclei. For higher centrality (or smaller impact parameter), the number of nucleons interacting increases, as does the multiplicity of produced particles. Selecting events with high particle multiplicity selects more central collisions.

To characterize event multiplicity and to implement multiplicity trigger, NA44 has a plastic scintillator counter positioned 3 cm downstream of the target and known as T0. It consists of two parts, each in shape of a rectangular parallelepiped $3\times12\times15$ mm, placed symmetrically around a vertical plane passing along the beam line trough the center of the target, with a 3 mm gap

between them. T0 covers $1.4 \leq \eta \leq 3.7$ for an η-dependent fraction of azimuthal angle, $0.22 \leq \Delta\phi/2\pi \leq 0.84$ respectively. Each half of the detector is equipped with two photomultiplier tubes (PMTs) for optical readout of scintillations. Signals from both halves of T0 are required to pass a discriminator threshold to form a *centrality trigger*. Normally, the discriminator thresholds are set so that the probability of a centrality trigger for an interaction event did not exceed 15%. In such events, there are over three hundred charged particles in the T0 acceptance.

2.4.3 Multiplicity trigger (*MUL1*)

It may happen that even though the T0 centrality trigger is present, the spectrometer (primarily due to the azimuthal narrowness of its acceptance) gets no reconstructable tracks, and the event is of no use for the analysis. In the Pb beam period, the tracking device of the limiting acceptance is the pad chamber. For this reason, since 1995, we require a hit in the pad chamber along with at least one hit slat in each of the scintillation hodoscopes H2 and H3 ($MUL1 \cdot PC$). To analyze correlations among identical particles, NA44 triggers on double track multiplicity. In this work, by *multiplicity trigger* a requirement of at least a *single* track is always meant.

2.4.4 Cherenkov veto trigger ($\bar{C}1 \cdot \bar{C}2$ and $\bar{C}2$)

In the high energy nucleon collisions, the majority of emitted particles are pions. In NA44, the product of the valid beam, centrality and multiplicity triggers provides a sample of events, strongly dominated by single pions. Measurements of kaons and protons, especially the HBT-correlation studies, require a dedicated trigger. It is implemented by vetoing events with noticeable emission of Cherenkov light in the medium with specially selected refraction index. By vetoing such events, one is able to get rid of the light particles, because

1. the Cherenkov photons of frequency ω are emitted by the medium when the charged particle's velocity v exceeds the phase velocity of electromagnetic waves with frequency ω in that medium: $v > c/n(\omega)$, where $n(\omega)$ is the refraction index;

2. momenta of the different particles in the detector's acceptance are made nearly equal by the spectrometer optics, so that the differences in the velocity arise solely because of the particle mass.

Detector	Gas	Pressure, atm.	e	π	K	p
$C1$	Freon 12 (CCl_2F_2)	2.7	6.6×10^{-3}	1.8	6.4	12.1
$C2$	$N_2/Ne, 85\%/15\%$	1.3	19×10^{-3}	5.2	18.3	34.8

Table 2.1: Threshold momenta (GeV/c) of common charged particles for $C1$ and $C2$.

$< p >$ GeV/c	$< (p- < p >)^2 >^{\frac{1}{2}}$ GeV/c	function in the trigger $C1$	$C2$	Trigger mode
4.1	0.4	ignored	ignored	no Cherenkov bias
4.1	0.4	veto	veto	π/e veto
7.7	0.6	ignored	ignored	no Cherenkov bias
7.8	0.7	ignored	veto	π/e veto

Table 2.2: Functions of the Cherenkov detectors in the trigger for various momentum settings

NA44 has two Cherenkov threshold detectors, known as $C1$ and $C2$. The information on their thresholds and functions in the trigger, collected in tables 2.1 and 2.2, illustrates their use.

2.4.5 Use of the trigger modes

The data points for published single particle distributions come from the $VB \cdot T0 \cdot PC \cdot MUL1$ trigger mode, complimented in case of Cherenkov veto by either $\bar{C}1 \cdot \bar{C}2$ or $\bar{C}2$ for collection of K/p samples (see subsection 2.4.4). For each setting of the spectrometer's angle and magnetic field, the data was taken with and without the Cherenkov veto, to understand the effect of the latter. $VB \cdot T0$ and $VB \cdot PC \cdot MULT1$ data is instrumental in understanding the effect of $T0$ and $PC \cdot MULT1$ on the multiplicity of the sample.

2.5 Scalers

During a run, a number of electronics registers (*scalers*) would be used to count particular events, being reset at the beginning of every spill. Their information is essential for setting up and maintaining the optimal running conditions, and for obtaining probabilities of physically meaningful events (e.g., creation of a kaon in the $Pb + Pb$ collision) from the data. In particular, the experimentalist needs to know the number of beam particles crossing the

target over the time of observation [2]. Some fraction of the time, the data acquisition system is busy handling the incoming information and the new data can not be recorded. The triggers may be presented, but not accepted. This is the *dead time* of the experiment, and it can be large for some trigger conditions. The $SCBCL$ scaler records beam counter coincidences over the live-gated time. Alternatively, one can count beam counter coincidences continuously and, knowing the ratio of presented/accepted triggers, correct the beam count for the dead time.

2.6 The Si pad detector

The Si pad array, installed 10cm downstream from the target inside the first dipole magnet, measures ionization energy loss of charged particles (dE/dx) in its 512 300 μm thick Si pads. The detector covers $1.5 \leq \eta \leq 3.3$ and 2π azimuthally. Radially, the pads are arranged to be fragments of 16 rings with equal pseudorapidity coverage (see Fig.2.2). Azimuthally, they constitute 32 sectors with equal angular coverage. δ-electrons, produced by the Pb nuclei of the beam especially copiously in the target, are swept away to one side by the magnetic field of the first dipole ($\approx 1.6T$ in the strong field setting). Because the energy spectrum of δ-electrons is dominated by low energies, this sweeping effect of the field leaves the other half relatively clean and useful for multiplicity analysis. The amplitudes are read out by AMPLEX [30] and digitized by C-RAMS (later DRAMS [31], see Section 2.9). By *occupancy* μ of a Si pad [3] we will mean the average number of tracks hitting the pad:

$$\mu = \sum_{i=0}^{\infty} w_i i, \tag{2.2}$$

where w_i is probability of having i hits in the pad. Typically, in the central trigger runs, the occupancy is somewhat above 1[4].

The charge collection time for a 300 μm path length in the Si is typically 10-20 ns [33]. AMPLEX has 600 to 800 ns peaking time [30]. Duration of

[2]The acceptance is narrow and not every event produces tracks in the spectrometer!

[3]μ is defined for each pad in a sample of events.

[4]An estimate for orientation: for Poissonian distribution of hits, $\mu = 1$ means that probability of having 1 or more hits is $1 - P(0) = 1 - exp(-1) \approx 0.63$, i.e. the detector, in fact, is merely semi-occupied.

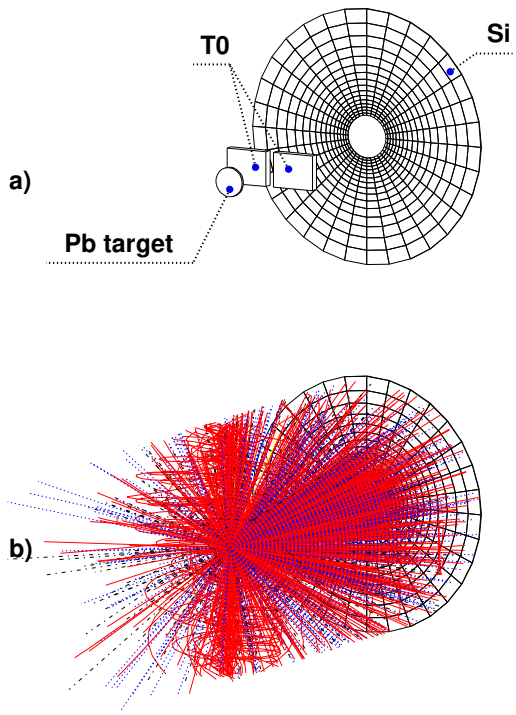

Figure 2.2: NA44 multiplicity detector complex: a) the lead target, the Si pad array and the T0 scintillators; b) the setup exposed to a simulated RQMD Pb+Pb event.

an SPS spill was about 4.7 s, and NA44 was typically operating at (2-4)$\times 10^6$ beam particles per spill. The thickest Pb target used had 0.034 interaction probability for the Pb beam. Therefore, the typical rate of minimum bias interactions was always below 31 kHz, i.e. on average 32 μs per interaction, and pile-up was highly unlikely.

The data from the detector was used in the texture analysis of the hadron production (using the data recorded in 1994), and in the analysis of meson production in the Pb+Pb collisions to normalize particle yields (the 1995 data). In the latter case, the same detector was used in its second running period, so that radiation damage was noticeable. In both cases, more information on the detector and its characteristics will be given in the appropriate sections.

2.7 Spectrometer "optics" and acceptance.

A magnet system of two dipoles and three superconductive focusing quadrupoles, together with a tracking complex (a pad chamber, three highly segmented scintillation hodoscopes H2, H3, H4 and two strip chambers, see Fig.2.1) provides momentum resolution of 0.2% or better for all spectrometer settings. The quadrupoles allow for two modes of focusing – vertical and horizontal. The distinction between them plays a role in HBT analysis; in the single particle analysis the horizontal mode has always been used. The spectrometer accepts charged particles of a single charge at a time. The magnet system is mounted on a rotating platform and was operated at two angular positions (44 and 131 mrad). The data analyzed are taken with two different field strengths. In the weak field mode, spectrometer accepts charged tracks in the momentum range of $3.3 < p < 5.1$ GeV/c, and of $6.3 < p < 9.7$ GeV/c in the strong field mode. These two field modes are often called "the 4 GeV/c" and "the 8 GeV/c" settings, respectively. Location of the acceptance area in rapidity y and transverse momentum p_T varies with field strength, arm angle, and particle mass, as is shown on Fig. 2.3. For K and π, the acceptances are located within one unit of y around the center-of-mass rapidity of the SPS $PbPb$ system ($y_{CM} = 2.92$) [5].

The magnitude of the spectrometer's acceptance is largely restricted by the factor $\Delta\phi/2\pi$ (typically around 0.02) representing narrowness of the azimuthal coverage. Within the spectrometer's acceptance at $p_T = 0.4$ GeV/c for a midrapidity pion, the remaining factors would amount to about 0.5. In the low angle setting during the Pb run, a tungsten collimator (the so called "jaws") was introduced into the magnet system in order to reduce the multiplicity of tracks in the spectrometer. Its effect on the acceptance has been computed via Monte Carlo and corrected for in the analysis. A more detailed discussion of these issues will be given in Section 3.1.

2.8 Means of particle identification

2.8.1 Tracking and time of flight

Three highly segmented scintillating hodoscopes (H2, H3 [34], H4) and three multiwire proportional chambers (MWPC) with cathode-segment read-

[5] Their peculiar "banana" shape in the p_T and y variables is due to the constraint, imposed on p_T and p_z by constancy of momentum p : ${p_T}^2 + {p_z}^2 = p^2 = const$, and, differentiating, from $dp/\,dy = 0$ one gets $dp_T/\,dy = -p_z E/p_T < 0$.

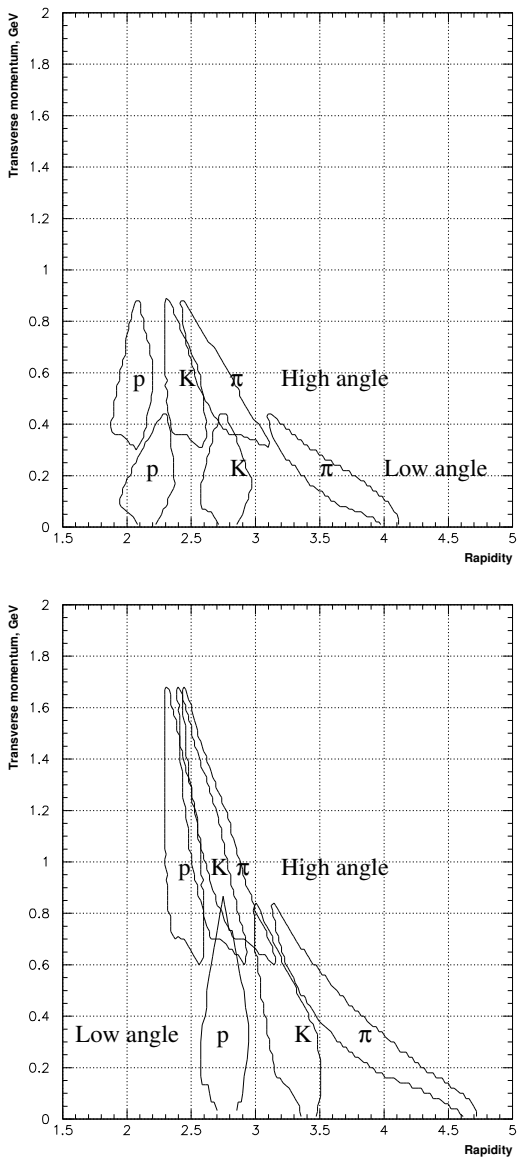

Figure 2.3: Acceptance area of the NA44 spectrometer in the laboratory rapidity y and transverse momentum p_T. Top: in the weak field mode; bottom: in the strong field mode.

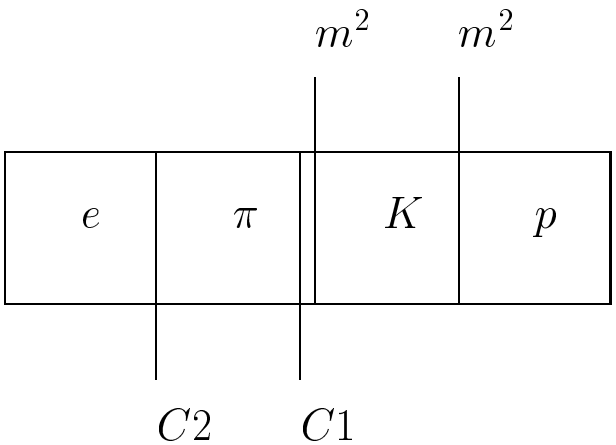

Figure 2.4: Means of particle identification in the weak field settings

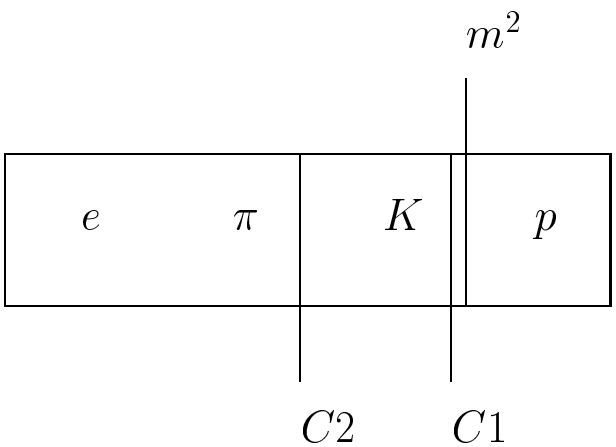

Figure 2.5: Means of particle identification in the strong field settings

out (a pad chamber, PC, and two strip chambers, SC1 and SC2, each having a plane of vertical and a plane of horizontal strips) form the tracking system[6] (see Fig. 2.1). In NA44, magnets and tracking detectors are separated in space so that tracks of charged particles are straight. There are no tracking detectors in the target area before the magnets.

Time of flight measurements with accuracy not worse than 100 ps are performed via H2, H3 [34], with the Cherenkov beam counter (described above in section 2.4.1) being the source of the start time reference with 35 ps accuracy.

[6]With '94 and '95 data, H4 was not yet used in the offline analysis.

The hodoscopes are segmented along the momentum-sensitive coordinate (i.e. horizontally) into vertical slats, sufficiently narrow so as to be able to detect particle pairs with momentum difference of $50MeV/c$ at $p = 10GeV/c$ in different slats. The scintillation light is read out from top and bottom of each slat by two PMTs, so that sensitivity to the vertical coordinate is gained from the comparison (though rendered obsolete with the addition of the strip chambers for the Pb running).

The NA44 MWPCs measure ionization energy losses of charged particles in the 50%/50% Ar/C_2H_6 gas mixture. Primary ionization is "amplified" in the process of avalanche ionization in the highly non-linear electrostatic field near the 20 μm anode wire. A cloud of charge, drifting under the influence of field, induces electrical pulses on the electrodes. The cathode is split into rectangular pieces, read out by separate channels of AMPLEX [30] chips. Normally, the same avalanche results in measurable inductions on several (4-8) channels, so that one can talk, in a sense, of an "image" of the avalanche, reconstructable off-line with good resolution: the required RMS of 2-3 hundred μm along the direction of the anode wire has been easily achieved. More details about NA44's MWPCs are found in [35].

2.8.2 The Cherenkov counters

The use of Cherenkov counters for particle identification and the principles of their operation have already been described in section 2.4.4. More information on the inefficiencies associated with the Cherenkov vetoing will be given in sections 3.4 and 3.5.

2.8.3 The Uranium Calorimeter (UCAL)

NA44 uses nine stacks of a fine-sampling Uranium/Copper/scintillator Calorimeter with wavelength shifter readout, originally designed [32] for the AFS experiment at ISR. Each stack is sub-divided into six towers. Each tower has two sections, read out separately: a 6 radiation lengths ($6X_0$) long electromagnetic one, and a 3.8 absorption lengths ($3.8\lambda_I$) long hadronic absorber. Each section is read out by two PMTs collecting light from two light guides that cover left and right flanks of the section. [7] Two characteristic features of

[7] By mid 1990s, after the long years of service, the scintillator's transparency became reduced by radiation damage to a level which severely undermined independence of the signal on the impact position along the face of the stack. I had to correct for that problem – more on this in section 3.4.

this device are

- nearly identical response to charged and neutral pions [8] (not required by NA44)
- self-calibration by measuring fission signal.

NA44 uses UCAL for e/π separation. In particular, in this analysis UCAL was used to determine how many pions are lost due to the Cherenkov electron veto in the trigger (see subsection 3.4.3). This is possible due to the longitudinal separation of the tower into electromagnetic and hadronic sections. The electromagnetic showers tend to have a predominant contribution from the electromagnetic section. Due to the low track multiplicity in the spectrometer, the UCAL's granularity is sufficient to associate tracks with towers.

2.9 Readout and Data Acquisition

The NA44 data acquisition trigger has been described in detail in Section 2.4. Our readout and data acquisition system is described in [36]. NA44 used both CAMAC (Computer Automated Measurement And Control) and VME (Versa Module Eurocard) standards. There were 760 channels read out via CAMAC and a variable number of channels [9] read out via VME C-RAMS (CAEN Readout for Analog Multiplexed Signal). Typically, about 1000 channels were read out per event. The T0, the event scalers, the H2, H3 and H4[10] TDCs and ADCs, the Cherenkov's counters' ADCs, and the UCAL ADCs were read out via CAMAC. The silicon ADCs, the TIC[11], and the pad and strip chambers were read out by the VME C-RAMS. After the 1994 run, the C-RAMS were replaced by DRAMS[31]. The speed of the DAQ (data acquisition) was limited by the CAMAC modules, which required about 4 μs per channel and thus 3 ms per event.

[8] In UCAL, 1-10 MeV neutrons from the nuclear break-ups in hadronic showers do not go unnoticed but induce fissions. These fissions contribute to the measured signal, thus rising it to a level typical for an electromagnetic cascade caused by decay products of a π^0 of the same energy.

[9] due to zero suppression

[10] Before the Pb run, H1 was replaced by a pad chamber, but the nomenclature for the rest of the hodoscopes was not changed

[11] this multichannel Threshold Image Cherenkov detector does not play any role in this analysis and I give no special description of it. Its design and operation are described in [37].

CASCADE[38] (CERN Architecture and System Components for an Adaptable Data acquisition Environment) – a distributed multiple-platform real-time data acquisition system developed at CERN – was chosen as the control software and hardware for the NA44 DAQ.

The DAQ hardware included a VME interrupt module CES RCB 8087 'CORBO', a Fast Intelligent Controller, FIC for short (CES FIC 8234, a Motorola 68040 single processor VME board), an HP-715/80 workstation connected to the FIC via Ethernet, an X-terminal and an STD (Summit Tape Drive) to record the data. The CORBO would accept inputs from the NA44 triggers and the SPS start-of-burst and end-of-burst and transfer them to the FIC via the VME bus. The FIC ran CASCADE event building software under its own OS-9/68K operating system and had 20MB of temporary memory to store the NA44 events during the bursts. Between the bursts, the data would be written to the STD tape. The maximum event rate under normal running conditions was about 120Hz, and the typical size of an event was 5-8 kB. The HP workstation was used as a file server for the FIC, and performed the tasks of run control and event monitoring.

Chapter 3

Technique of the NA44 single particle analysis

In this chapter I discuss the problems of the off-line data analysis: acceptance correction, trigger centrality determination, cleanliness and efficiency of particle identification, and conclude with a summary review of sources of systematic errors to the single particle yields and distributions. Introductory discussion of particle identification has been given in section 2.8.

3.1 Acceptance correction

I start with acceptance correction because this is a problem whose solution does not depend on the information presented in the rest of this chapter. On the other hand, a procedure to determine the trigger centrality, reported in section 3.2, involves an acceptance correction.

3.1.1 Introduction and definitions

The total energy E and a three-dimensional vector of momentum $\vec{p}$ of a particle, emitted in an interaction, along with that particle's internal quantum numbers (mass m, charge, spin, strangeness, baryon number, etc), carry important information about the dynamics of the interaction. The simplest way to analyze this information is by using statistical distributions of particles with respect to various kinematical variables, derived from its Minkowski energy-momentum four-vector $(E, \vec{p})$. Among such variables are

- transverse momentum $p_T = \sqrt{p_x^2 + p_y^2}$,
- transverse energy $m_T = \sqrt{p_T^2 + m^2}$,
- transverse kinetic energy $k_T = m_T - m$,

- rapidity $y = 1/2 \ln((E + p_z)/(E - p_z))$,
- pseudorapidity $\eta = -\ln(\tan(\theta/2))$, where θ is zenith angle.

It is a popular practice to use m, p_T, y and azimuthal angle ϕ instead of $(E, \vec{p})$, because in the former set of variables three (m, p_T, ϕ) are Lorentz-invariant with respect to translations along the z axis, whereas y is Lorentz-transformed by a simple addition of a number, so that Δy is Lorentz-invariant.

In particle physics, one uses the notion of a differential cross-section of particle production [1]

$$\frac{E\, d^3\sigma}{dp^3} \tag{3.1}$$

With our preferred set of kinematical variables, one notices that

$$\frac{E\, d^3\sigma}{dp^3} = \frac{E\, d^3\sigma}{d\phi p_T\, dp_T\, dp_z} = \frac{d^3\sigma}{d\phi p_T\, dp_T\, dy} = \frac{d^3\sigma}{d\phi m_T\, dm_T\, dy} \tag{3.2}$$

Whatever reference is chosen to measure ϕ, in practice one will see a set of interaction events averaged over all possible azimuthal orientations of the colliding system, unless one's experiment is more sensitive to some of them than to others. For experiments which do not distinguish azimuthal orientations (like NA44), nature performs a Monte-Carlo integration of Eq. 3.1 over ϕ, and one is left with

$$\frac{d^2\sigma}{m_T\, dm_T\, dy}. \tag{3.3}$$

It may be more direct to talk about

$$\frac{d^2N}{m_T\, dm_T\, dy}, \tag{3.4}$$

[1] The reason to choose *this* Lorentz-invariant combination of quantities is the fact that differential cross-section of an interaction of particles A and B with an arbitrary number of secondaries (indexed by f) in the final state is given by [39]

$$d\sigma = ((2S_A + 1)(2S_B + 1)4j)^{-1} \times \sum_{S_i, S_f} |M|^2 \Big(\prod_f \frac{{dp_f}^3}{2E_f (2\pi)^3}\Big) (2\pi)^4 \delta^4(p_A + p_B - \sum_f p_f)$$

where j is an invariant flux, S_A, S_B, S_f are spin quantum numbers, and $|M|^2$ is the squared modulus of the invariant amplitude of the process. Therefore Eq. 3.1 represents the $|M|^2$ integrated over the phase space of the non-observed particles, with certain coefficients.

N being the number of particles of given identity emitted in an interaction event. What one measures however is

$$\frac{d^2n}{m_T\, dm_T\, dy} = A(y, m_T)\frac{d^2N}{m_T\, dm_T\, dy}, \tag{3.5}$$

where $A(y, m_T)$ is an *acceptance function.* $A(y, m_T) < 1$ due to experimental inefficiencies. Technically, $A(y, m_T)$ is represented in the analysis by a TURTLE[40]-based Monte Carlo simulation procedure and takes into account the effects of focusing and analyzing optics of the spectrometer as well as tracking efficiency and decays:

$$MC_{output} = MC_{input}A(y, m_T) \tag{3.6}$$

The output from the single particle analysis will be presented in form of 1D distributions, or integrals of Eq. 3.4:

$$\frac{dN}{dy} = \int_m^\infty \frac{d^2N}{dy\, dm_T}\, dm_T, \quad \frac{dN}{m_T\, dm_T} = \int_{y_{min}}^{y_{max}} \frac{d^2N}{dy m_T\, dm_T}\, dy \tag{3.7}$$

3.1.2 How to extract the one-dimensional distributions

Acceptance of the NA44 spectrometer is discussed in section 2.7 and presented on Fig. 2.3. The $1/m_T\, dN/\, dm_T$ spectra fall with m_T and their shapes within the NA44 acceptance can be justifiably fit [93] by a single $\exp(-m_T/T)$. The T will be referred to as a *temperature parameter* or a *slope parameter.* In determining $dN/\, dy$ and $1/m_T\, dN/\, dm_T$ for kaons and pions we use spectrometer settings, or portions thereof, with $\Delta y = 0.2 - 0.6$. The slope parameters do not depend appreciably on y within this small range. [2] Then the double differential multiplicity can be factorized [3] as

$$\frac{d^2N}{dy\, dm_T} = B(y)T(m_T) \tag{3.8}$$

[2]This is supported by the existing data [41] on the change of $< p_T >$ with y for primary negative hadrons. As y goes from 3.4 to 3.9, $< p_T >$ drops from ≈ 0.382 GeV/c to ≈ 0.378 GeV/c, i.e. by $\approx 1\%$. Such an effect will not be visible due to other larger error bars.

[3]$B(y)$ and $T(m_T)$ are defined by Eq. 3.8 itself. Either one of them therefore can contain an arbitrary multiplier. For our goals, this ambiguity is irrelevant, as will be clear from the way $B(y)$ and $T(m_T)$ enter Eq. 3.13 and Eq. 3.14.

In parallel to the equations (3.7), for the observable particle counts one can define

$$\frac{dn}{dy} = \int_m^\infty \frac{d^2n}{dy\,dm_T}\,dm_T \tag{3.9}$$

$$\frac{dn}{dm_T} = \int_{y_{min}}^{y_{max}} \frac{d^2n}{dy\,dm_T}\,dy \tag{3.10}$$

(Technically speaking, they are projections of 2D histograms.) Integration of Eq. 3.5 assuming that Eq. 3.8 holds yields

$$\frac{dn}{dy} = B(y)\int_m^\infty T(m_T)A(y,m_T)\,dm_T \tag{3.11}$$

If Eq. 3.8 is true, $dN/\,dy$ from Eq. 3.7 can be rewritten as

$$\frac{dN}{dy} = B(y)\int_m^\infty T(m_T)\,dm_T \tag{3.12}$$

Eliminating $B(y)$, we conclude the "theoretical justification" for what is known as a 1D acceptance correction:

$$\frac{dN}{dy} = \frac{dn}{dy}\frac{\int_m^\infty T(m_T)\,dm_T}{\int_m^\infty T(m_T)A(y,m_T)\,dm_T} \tag{3.13}$$

Similarly, for the m_T spectrum we get

$$\frac{dN}{dm_T} = \frac{dn}{dm_T}\frac{\int_{y_{min}}^{y_{max}} B(y)\,dy}{\int_{y_{min}}^{y_{max}} B(y)A(y,m_T)\,dy} \tag{3.14}$$

Similar equations can be obtained for p_T or k_T. In principle, one needs to know $B(y)$ and $T(m_T)$ in order to determine the true shape of m_T spectrum and $dN/\,dy$. In practice, for pions $B(y)$ was taken to be a Gaussian with $\sigma = 1.4$ [4] centered at mid-rapidity; for kaons – a Gaussian with $\sigma = 1.1$. [5] For the

[4]This is the σ of the pion distribution according to RQMD and also the σ of the NA49's h^- [41] distribution. My attempts to determine this parameter from our own pion data led me to conclude that this can only be done with accuracy as poor as 50% because of narrowness of our coverage in y. The result however is consistent with NA49 and RQMD. This remark applies to the kaons too.

[5]As in RQMD.

T_i, GeV	w_i (π^+)	w_i (π^-)
0.06	$(0.43 \pm 0.12) \times 10^{-1}$	$(0.51 \pm 0.17) \times 10^{-1}$
0.10143	$(0.25 \pm 0.11) \times 10^{-1}$	$(0.76 \pm 0.24) \times 10^{-1}$
0.14286	$(0.1 \pm 0.2) \times 10^{-2}$	$(0. \pm 0.19) \times 10^{-2}$
0.18429	$(0.185 \pm 0.06) \times 10^{-1}$	$(0.6 \pm 0.7) \times 10^{-2}$
0.22571	$(0.53 \pm 0.06) \times 10^{-1}$	$(0.76 \pm 0.04) \times 10^{-1}$
0.26714	$(0.48 \pm 0.2) \times 10^{-2}$	$(0.4 \pm 0.6) \times 10^{-3}$
0.30857	$(0.1 \pm 0.2) \times 10^{-3}$	$(0. \pm 0.4) \times 10^{-3}$
0.350	$(0.2 \pm 0.4) \times 10^{-3}$	$(0. \pm 0.2) \times 10^{-3}$
χ^2/NDF	88./66	87./66

Table 3.1: Parameters of the multi-temperature fits to the transverse kinetic energy distributions of pions. See Section 3.1.2, Eq. 3.15. The fitting range is $0 < k_T < 1.5GeV$

acceptance correction in y, I used

$$1/m_T \, dN/ \, dm_T = \sum_{i=1}^{8} w_i \exp(-m_T/T_i) \tag{3.15}$$

Here w_i are 8 variable parameters, T_i are fixed "temperatures". For pions, all 8 parameters were used (see Table 3.1); for kaons, good fits could be obtained with only one T parameter (see Table 4.1). The original idea of fitting the pion $mT - m$ distributions with the multi-temperature formula 3.15 to test sufficiency of a simple statistical description with a single temperature and a chemical potential, by transforming the $mT - m$ spectrum into a "temperature spectrum". The pion spectra seem to be dominated by a temperature component around 200 MeV.

3.1.3 Corrections for the inefficient hodoscope slats

Some slats of H2 and H3 have had low signal because of bad coupling between the light guide and the phototube. For these slats the separation between the pedestal and the 1 MIP peak was so small that they might only "fire" part of the time. A Monte Carlo inefficiency correction procedure [6] was used to correct for that. It was based on efficiency monitoring carried out off-line run-by-run. The efficiency of suspect channels in a particular run was calculated by comparison of its bin content with two neighboring ones.

[6] due to Michael Murray

The number of tracks in a run would be recorded. The overall efficiency of a channel throughout a series of runs used in the analysis would be calculated as a weighted average efficiency. The total loss of efficiency due to the slat malfunction was of the order of few percent. The same procedure corrected for the "dead" slats.

3.1.4 Acceptance correction for the non-identified tracks

In the task of finding the centrality of the physics trigger settings (discussed in section 3.2), the problem of obtaining $dN/d\eta$ of the spectrometer for comparison with the Si pad array arose. Technically, the solution was facilitated by the (quite artificial !) trick of assigning a pion mass to every particle regardless of its identity, then fitting the so obtained "k_T" distribution by the multitemperature formula 3.15 and extrapolating [7] for every setting from $p_T = 0$ to $p_T = \infty$ to get $dN/d\eta$.

3.1.5 Imperfections of the acceptance correction and the effects thereof

Due to inaccuracies of our knowledge of the geometrical positions of the equipment in the hall and of the magnitude and configuration of the magnetic field, the acceptance correction is imperfect. It is less reliable on the edges. Typically, when looking at either dN/dy or k_T spectra from a single setting with sufficiently fine binning one sees points on the edges of acceptance that deviate sharply from the overall pattern. These points must not be included in the fiducial cut area. [8] A sharp non-constancy of dN/dy, inconsistent between different settings, would indicate that a wrong $T(m_T)$ was used.

Acceptance correction to the m_T or p_T spectra includes information about shape of the dN/dy distribution. Therefore any uncertainty in the dN/dy shape results in an uncertainty of the slope. In quantifying the uncertainty, the first step was to derive the error propagation factor to convert the uncertainty of the dN/dy width into uncertainty of the inverse slope T. I describe the dN/dy with a Gaussian whose width I denote by σ_G. MC was run with two

[7] here the artificial mass assignment is equivalent to changing the integration variable within the integral and does not change the result

[8] The resulting y ranges are listed in Table 4.2.

widths of input dN/dy: $\sigma_{G1} = 1.1$ and $\sigma_{G2} = 0.5$. The slopes were extracted in the two cases and compared, the error-propagation factor was found to be[9]

$$dT/dW = (T(\sigma_{G1}) - T(\sigma_{G2}))/(\sigma_{G1} - \sigma_{G2})$$

It is : for 8 GeV/c high angle: $-52MeV$, for 4 GeV/c high angle: $-117MeV$. The problem however is to characterize the uncertainty of our knowledge of the W. This has been done in the following (somewhat arbitrary !) way: I say that with "3σ" (99.7%) confidence level, the Gaussian kaon dN/dy distribution has W parameter between 0.8 and 1.4. [10] Then, one can derive and propagate the "1σ" uncertainty. The resulting uncertainty in the inverse slope can be found in Table 4.1. It dominates the total systematic error, even though smaller additional uncertainties are possible due to other sources.

3.1.6 Collimator-related uncertainties

Due to the crucial role played by the single-channel Cherenkov devices, the charged track multiplicity has to be kept low. In preparation for the Pb beam, the need of limiting the spectrometer's acceptance in the low p_T setting was realized. The problem was solved by installing a tungsten alloy (90% W, 6% Ni, 4% Cu) collimator ("jaws") in the magnetic channel of the spectrometer, between D1 and Q1 (see Fig. 2.1). Orientation of the collimator corresponds to the focusing setting and is horizontal in the singles data. In order to cut off the tails of the particle distribution where the particles momenta might be affected by interaction with the collimator, a cut on the vertical component of momentum p_y has been applied. The TURTLE[40]-based Monte Carlo simulation available during my work on the singles analysis used to deviate from the experimental data in its prediction of the peak position in p_y, shifting it in the positive direction by $\approx$ 2.5 MeV/c. I studied dependence of the acceptance corrected dN/dy of various particles on the position of a narrow p_y window, in which the samples were collected. The sliding window cut study showed that, as the window slid towards the negative p_y, the dN/dy would increase due to the "emptiness" of MC acceptance, not balanced out by the data. For the positive p_y, an abnormal decrease would be observed. In between these two regimes, a narrow zone of relative independence of dN/dy on the p_y cut position would be found. Such a behaviour (see Fig. 3.1) is characteristic

[9]assuming that the dependence of the apparent inverse slope T on the width is smooth enough so that it can be inter- and extrapolated by the two points.

[10]The somewhat arbitrarily chosen number here is 99.7%.

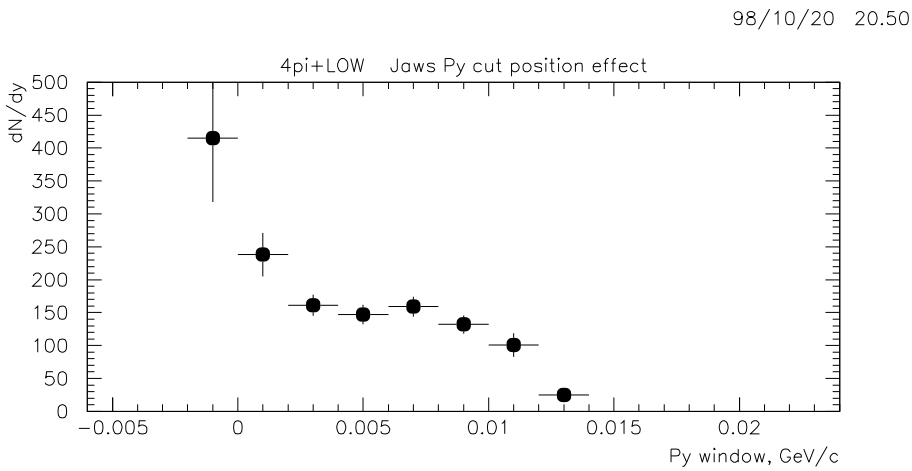

Figure 3.1: Understanding the collimator-related uncertainty in the acceptance-corrected pion dN/dy. The horizontal bars show the extent of the fiducial p_y window used. In this plot, other corrections were fixed at the values they had when the study was undertaken.

of situations with a misplaced acceptance. The remedy is to avoid any of the edges, by limiting the acceptance to the middle zone. The p_y ranges so chosen are listed in Tables 3.7 and 3.9.

3.2 Determination of the trigger centrality

In NA44, the trigger-level centrality selection combines T0 multiplicity discrimination with the inherent centrality-biasing effect of the narrow midrapidity acceptance of the spectrometer. This makes the centrality normalization of the particle yields in this experiment particularly difficult. (The nature of the problem will be explained in Subsection 3.2.1.) In the present work, centralities of the physics settings were determined from 1995 data using the Si pad array *multiplicity*, via a method developed by the author to respond to the specific challenges of this particular experiment and a particular data set. In this method, the trigger centralities play the role of "calibration constants" that ensure consistency of the absolutely normalized spectrometer and Si data. Apart from the normalization factors themselves, this section provides justification of the method and gives a reasonable amount of technical background information.

3.2.1 The problem of absolute normalization

In nature, the probability for two nuclei to collide with impact parameter between b and $b + db$ grows linearly with b, and majority of the collisions are peripheral. In the experiment, the events to be recorded are selected by a trigger which is sensitive to the event centrality via multiplicity of the emitted particles. A trigger can be described by its probability density of selecting an event of certain total multiplicity. In reality, this probability density will never have a sharp edge, and the poorer the equipment, the more smeared will the edge be. It is therefore best to characterize the centrality trigger by giving the functional form of the total multiplicity distribution it produces. If this form is identical for two triggers, we will say that they belong to the same *centrality class*.

The problem of absolute normalization arises when one wants to obtain the event averaged number of particles (N) emitted in the collision events of certain centrality (impact parameter) range, or probability density distributions of particle emission with respect to kinematical variables.

$$N = \frac{\mathcal{N}}{E}\frac{1}{\mathcal{A}}, \tag{3.16}$$

where the desired average N is calculated from the number $\mathcal{N}$ of detected particle tracks over E collision events of given trigger-selected centrality class, using the apparatus which registers only $\mathcal{A} \leq 1$ fraction of such tracks.

$$E = B \times i \times c, \tag{3.17}$$

where the E collisions are selected from the $B \times i$ inelastic beam-target interactions by means of the trigger. The trigger is represented by quantity c, which will be called trigger centrality. The interaction probability i in eq. (3.17) is not measured precisely. Unknown in the eq. (3.17) is $i \times c$. The beam count B is live-gated and measured by the Cherenkov beam counter (sections 2.5, 2.4.1, [29]). In this section I quote c, assuming that $i = 0.034$ (as discussed in section 2.3).

The E includes collisions with and without tracks in the acceptance. Important here is that even though the E includes collisions with no tracks in the acceptance, the requirement for them to be of the same centrality class as the trigger events (to ensure "cleanliness" of the average (3.16)) forces one to pay attention to all centrality-sensitive components of the trigger. The notion of the **trigger-selected centrality class**, or sample, and its characteristic c becomes therefore the key issue of the normalization analysis.

c is the fraction of inelastic interactions, which includes all of the following and only the following:

(a) interactions that satisfy the trigger requirements

(b) for every interaction of group (a), all interactions of the same *total multiplicity* that happened in reality during the run, but did not cause triggering due to absence of tracks in the spectrometer's acceptance, and only due to this reason.

The class of events just described will be also referred to as the "normalization sample" or "c-sample". This definition of c guarantees that the N in formula (3.16) is indeed the correct average multiplicity in the centrality class selected by the trigger.

One should bear in mind that there is also a group of events which *do not* belong to the same total multiplicity class as the trigger events, have *acceptable* T0 amplitude in the trigger and do not create tracks in the spectrometer. They must be excluded from the definition of the trigger-selected centrality class and be not confused with the events of group (b) ! (Otherwise the result will be an underestimate of the true N !). This subtlety would not exist for a large acceptance experiment, due to absence of the group (b) itself. Among the mechanisms responsible for existence of the events with lower total multiplicity but acceptable T0 amplitude are δ-electrons, noise and fluctuations associated with operation of T0, fluctuations in the distribution of charged tracks in space.

Let us list the centrality-sensitive components of the trigger and briefly discuss them.

3.2.2 Role of T0

The fraction of the full azimuthal angle covered by T0 depends on the (pseudo)rapidity and varies between 0.84 for $\eta = 3.7$ and 0.22 for $\eta = 1.4$, being 0 outside this η-range. Due to geometrical reasons, a "natural" (no trigger bias) sample of collisions is dominated by peripheral ones. To what extent do the peripheral collisions with pronounced reaction plane (and fragmentation ?) effects "emulate" the T0 response typical for the central events, given the mirror-symmetric (rather than azimuthally symmetric) geometry of T0 ? Our analysis of the Si pad array multiplicity allows to say that the combination of T0 discrimination with the "midrapidity" trigger coming from the spectrometer (*MUL1*) selects a fairly homogeneous sample of events without exceptionally low Si multiplicities. In the normalization scheme being

described, the T0 amplitude of the δ-free side[11] (and only it) is used to define samples of different centralities.

3.2.3 Role of *MUL1*

Distribution of the number of tracks that hit the spectrometer's acceptance deviates from the Poissonian one due to the variation of the Poissonian mean event to event, and due to two-particle and multiparticle correlations. Realizing that, it is nevertheless useful to recall that in the Poissonian case with average μ, $(n+1)P(n+1)/P(n) = \mu$. Upon comparison with the ratio of double to single track events we see in the central trigger runs of our experiment, it is clear that even in Pb+Pb, the spectrometer (even in the low angle setting, due to the "jaws") presents a target which is difficult to hit ($\mu \ll 1$). I use

$$P(0) \simeq \exp(-2P(2)/P(1)) \tag{3.18}$$

as a measure of the probability that the spectrometer has zero tracks. (In case of the Poissonian law, the equation (3.18) would be exact. The current discussion however does not pursue more than qualitative understanding.) Table 3.2.3 summarizes the Poissonian estimates of $P(0)$.

momentum	+ 4 GeV		+ 8 GeV		- 4 GeV		- 8 GeV	
p_T setting	low	high	low	high	low	high	low	high
h	0.76	0.91	0.71	0.95	0.77	0.92	0.72	0.96
K/p	0.96	0.97	0.93	0.97	h^-	0.99	0.97	0.99

Table 3.2: The estimated fraction of events that do not create tracks in the spectrometer. It has been obtained according to the Poissonian law, $P(0) \simeq \exp(-2P(2)/P(1)$, based on the DST information.

Had it been easy to satisfy ($\mu \geq 1$), the *MUL1* requirement would not have been considered important component of the centrality trigger. Therefore, *MUL1* needs to be taken into account for determination of the trigger centralities.

[11] that is, the side of the detector, free of δ-electrons due to the deflecting effect of the dipole magnetic field.

3.2.4 General idea of the procedure

Based on the discussion in the previous sections, one can foresee two directions that lead to the correct determination of the c-sample:

1. direct (or indirect) counting of events that satisfy the set of conditions which makes up the c-sample (see the definition in section 3.2.1). In NA44, the criterion of the c-sample has no direct hardware implementation. I invested a lot of effort into attempts to quantify the difference between the c-sample and the samples that do have direct hardware implementation (various trigger modes), by analyzing properties of the latter (e.g., correlations between the amplitudes of left and right T0 scintillators). Dissatisfaction with this path of analysis eventually led me to prefer the following idea:

2. there is a device that does not need the operation of average (as in equation (3.16)) and, therefore, the "normalization sample", to get the multiplicity. The Si pad array measures multiplicity of individual events, event-by-event. For any trigger mode, no matter how complex it is, the Si can give multiplicity of each event taken and thus the average multiplicity. The left-hand side of equation (3.16) becomes known, and so one determines the c of the trigger (given i).

3.2.5 How to use the Si pad array

Given the quality of the Si amplitude resolution in 1995, the traditional method of multiplicity analysis, based on the channel-by-channel comparison of amplitude with the MIP expectation, can not be reliably used for the whole run period, because the amplitude resolution was affected by radiation damage. Multiplicity analysis can be performed under considerably relaxed requirements to the amplitude resolution, if the probability distribution $P(n)$ of number of tracks n, crossing an individual pad of the array, is known. Our eventual goal, sufficient for the task of normalization as it is formulated in the section 3.2.1, is finding a single number, $dN/d\eta$, characterizing the average multiplicity of the whole detector, averaged over all events of a physics run. Therefore it is acceptable to deal with one $P(n)$ for the whole detector, over the whole run (or a set of runs taken with a specific trigger and angular setting). Then, number H of the hit pads (i.e., pads with signal above the threshold, set during the calibration and subtracted during the DST [12]-production) out

[12]DST – the Data Summary Tape.

of M pads in total, is

$$H = M(1 - P(0)) \tag{3.19}$$

As a measure of Si multiplicity, I use the Si occupancy calculated event by event as

$$N = -M \ln(1 - H/M). \tag{3.20}$$

Here N is the number of tracks that cross the array of M channels and create H hits. Equation 3.20 uses the Poisson law for $P(n)$. N is linearly correlated with the total amplitude (the sum of the channel amplitudes), and for low occupancy cases I use the amplitude (properly calibrated in the units of N) instead because in those cases contribution of noise hits (due to drifting pedestals) or absent hits (again due to drifting pedestals) may be significant.

The multiplicity via occupancy expression (Eq. 3.20) has been justified as an integral, or "average", multiplicity over the Si acceptance. Variation of multiplicity from ring to ring is thus neglected. The technical reason for that was the absence of individual ring data in the existing DSTs. If the track density is not uniform over the Si acceptance, the formula results in a systematic error, which increases for steeper $dN/d\eta$. Let's compare the approximate expression for multiplicity with the exact one.

Approximate (Eq. 3.20 detailed):

$$N = -16m \ln(1 - \frac{\sum_{i=1}^{16} H_i}{16m}), \tag{3.21}$$

where m is number of pads in a ring, H_i is number of hits, and N is the number of tracks crossing the detector.

Exact:

$$N = \sum_{i=1}^{16} N_i \tag{3.22}$$

where every

$$N_i = -m \ln(1 - H_i/m) \tag{3.23}$$

– from every ring. Therefore the exact formula is

$$N = -m \ln(\prod_{i=1}^{16}(1 - H_i/m)) \tag{3.24}$$

To summarize, the approximate expression uses the *arithmetic* average in the logarithm, while the exact one replaces it by the *geometrical* average. We also see that the approximate and exact expression become *identical* if

$$H_1 = H_2 = H_3 = ... = H_{16} \tag{3.25}$$

i.e., if the distribution is uniform over the 16 rings of the detector.

Thus we see that knowledge of the distribution can serve to correct for the systematic error. In principle there are two choices:

- purist: use real Si data to extract the shape of the distribution, and use that information to get the correction.

- pragmatic: we know (and use this knowledge elsewhere in the analysis) that RQMD reproduces the shape of the non-identified charged dN/dy (and therefore $dN/d\eta$) fairly well. Compare, e.g., the NA49 data points in Fig 3.2 with the corresponding RQMD histogram plotted as a line. So, we can use

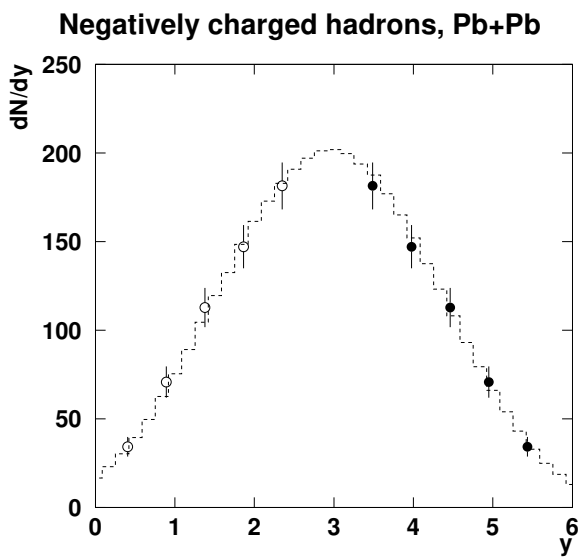

Figure 3.2: dN/dy distributions for negative hadrons: solid and open points – from NA49 measurements [41]; the histogram – from RQMD events of comparable centrality.

RQMD to get the correction.

I followed the second path. [13] The average number of tracks hitting a

[13]In the subsequent event texture analysis, I extracted the $dN/d\eta$ shape from the Si data. It was not different from that of RQMD or HIJING.

pad in a specific ring can be extracted from a properly binned RQMD charged track (+ and −) $dN/d\eta$ distribution:

$$\frac{N}{M} = \frac{\Delta N}{\Delta\eta} \times \frac{\Delta\eta}{M} = \frac{\Delta N}{\Delta\eta} \times \frac{(3.3-1.5)}{16}\frac{1}{32} = 0.0035 \times \frac{\Delta N}{\Delta\eta}$$

because 16 rings (with equal pseudorapidity coverage) of the detector cover pseudorapidity range 1.5 to 3.3, and each ring has 32 pads. Inverting Eq. 3.20, the 16 values of H_i/M_i were obtained – they range between 0.5 and 0.8. Plugging them into the "approximate" and "exact" expressions above yields the correction:

$$\frac{dN/d\eta(exact)}{dN/d\eta(approximate)} = 1.022$$

Conclusion: the multiplier 1.022 needs to be applied to account for deviation of the $dN/d\eta$ distribution from uniformity over the Si acceptance.

3.2.6 Si – spectrometer acceptance matching

After the Si multiplicity is obtained, it needs to be compared with the spectrometer $dN/d\eta$. One needs to take into account that Si acceptance is broader and extends further from midrapidity than spectrometer's; therefore $dN/d\eta$ is measured over different ranges of η. I had to involve RQMD simulation to be able to compare $dN/d\eta$ from the Si and the spectrometer. In principle one can get the same answer from the measurement of non-identified dN/dy distribution for + and − (like NA49's h^- [41]).

Therefore I require that the absolute $dN/d\eta$ in Si and spectrometer match with factors which I derive from RQMD distribution, see Table 3.3. The spectrometer acceptance was cut down to a fiducial range, free of the edge effects (monitored by the acceptance-corrected $dN/d\eta$ histograms with high resolution in η). These factors are the ratios of $dN/d\eta$ from the simulation alone. The simulation needs to know only the gross shape of $dN/d\eta$ for both signs, which RQMD does know. (Its dN/dy distribution for pions has $\sigma = 1.4$ in agreement with NA49 h^- [41].) The words "simulation alone" mean that delta electrons which I do not simulate, as well as imperfections of Si alignment, which I do not know, do not affect the simulated factors. Massive particles have asymmetrical $dN/d\eta$ distribution and our high angle spectrometer settings cover them more efficiently than Si. As a result, the simulated factors are different for + and − because of the asymmetry between protons/antiprotons and K^+/K^-.

$\frac{spectrometer}{Si(+and-)/2}$	Spectrometer sign	
	+	−
high angle	1.208	0.986
low angle	1.025	0.871

Table 3.3: RQMD-generated factors for acceptance matching. The following acceptance intervals were used. For the Si: $\eta_{min} = 1.5$, $\eta_{max} = 3.3$. For the spectrometer: in the low angle setting, $\eta_{min} = 3.6$, $\eta_{max} = 4.4$. In the high angle setting, $\eta_{min} = 2.6$, $\eta_{max} = 3.1$.

3.2.7 $dN/d\eta$ matching: Si vs spectrometer

This subsection explains the core procedure of centrality determination. It consists in finding the number c which gives the closest match between the Si and the spectrometer data, and is illustrated by the chart in Fig. 3.3.

In my method I scan correlation between the normalized (under some tentatively assumed trigger centrality) spectrometer $dN/d\eta$ of non-identified tracks and the Si $dN/d\eta$. Acceptance correction for the non-identified spectrometer tracks is described in subsection 3.1.4. The spectrometer $dN/d\eta$ is corrected for the inefficiencies due to dead channels, presence of the pad chamber in the trigger, tracking confidence level cuts, and includes extrapolation to $p_T = \infty$. The correlation is scanned varying the T0 multiplicity, with 14 fixed T0 thresholds. The centrality that makes spectrometer and Si $dN/d\eta$ match with the factors shown in the Table 3.3 is accepted. An example of such centrality fitting is illustrated by Fig. 3.4 and Fig. 3.5.

Shown in the right part of Fig. 3.4 is the "diagonalized" T0 distribution from two PMT tubes on the δ-free side. (The "diagonalization" means that distributions from two tubes on the δ-free side were gainmatched, the covariance matrix that describes their correlation was diagonalized, and the value plotted is the diagonalized coordinate which is correlated with multiplicity. The zero of the normalized unit is chosen at the mean vealue of the distribution.) The points shown correspond to 14 centrality bins with boundaries 0, .0001, .0002, .0005, .001, .0025, .005, 0.01, 0.02, 0.04, 0.06, 0.08, 0.10, 0.12, 0.14, later referred to as c_i. Of course, the thresholds t_i change with different values assigned as the overall trigger centrality. The vertical lines across the T0 distribution in the right panel of Fig. 3.4 show locations of the thresholds which maximize the correlation in the left panel.

Fig. 3.5 justifies why the correlation on Fig. 3.4 was found to be maximized by the centrality chosen. It shows the χ^2 (per number of degrees of freedom) between each of three possible correlations and the one expected

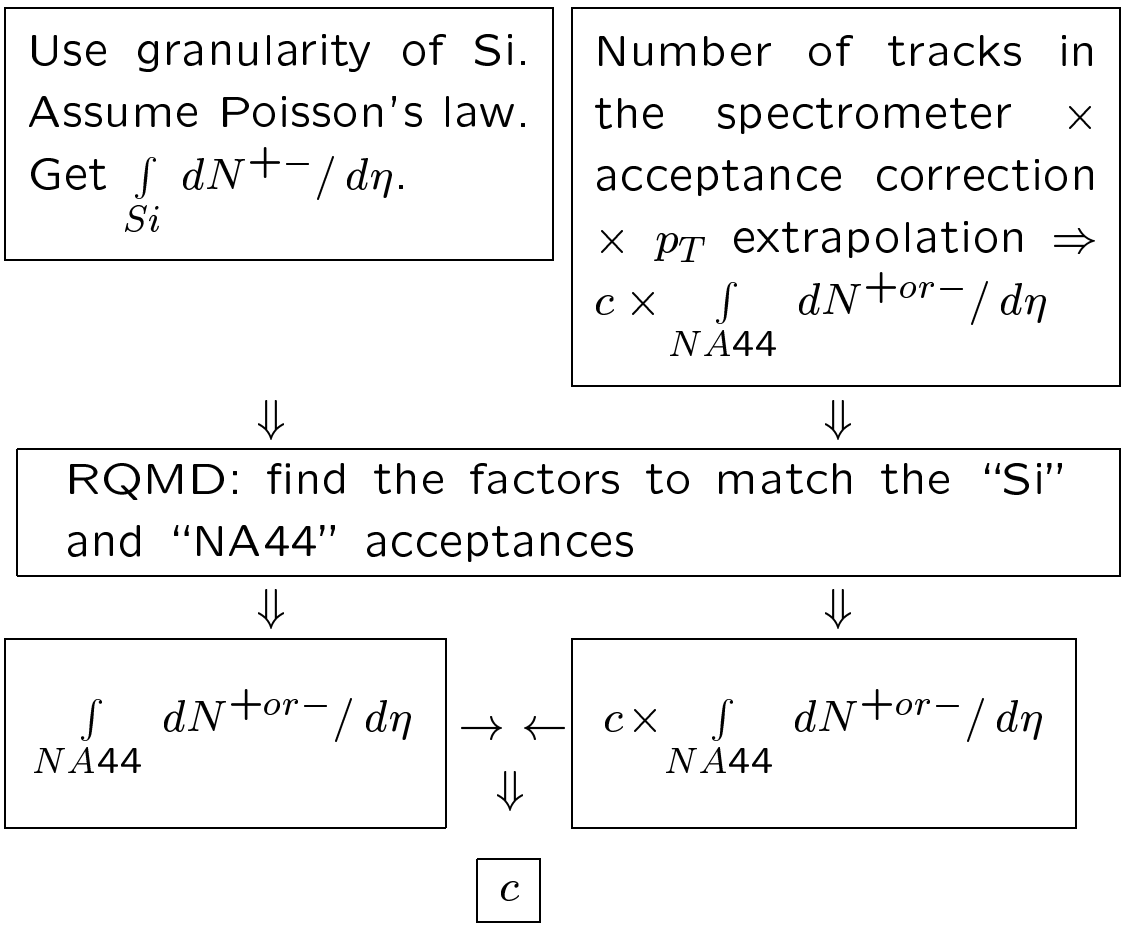

Figure 3.3: Determination of the trigger centrality by matching the Si and spectrometer multiplicity data. The multiplicity comparison is done withing the same multiplicity classes based on T0 amplitude, see text.

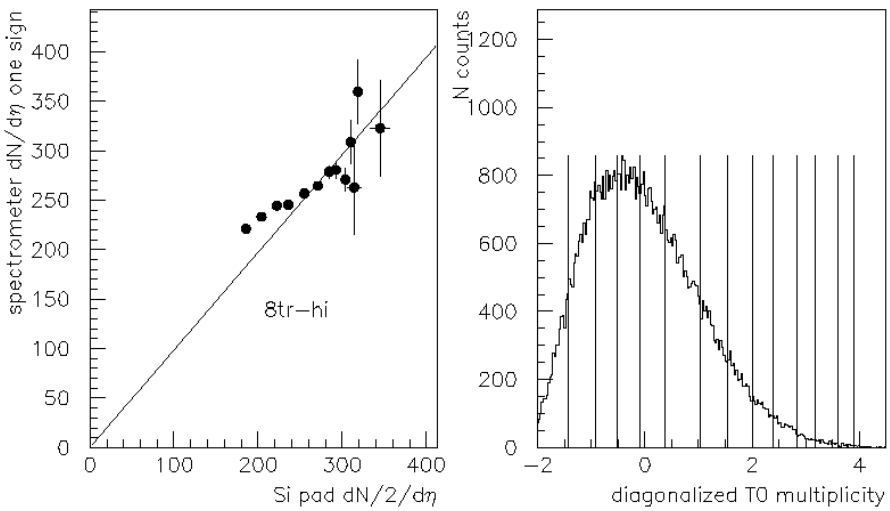

Figure 3.4: Left: correlation between $dN/\,d\eta$ obtained by charged track counting in the spectrometer and fired pad counting in the Si, found to be the best for a particular spectrometer setting. Right: positions of the multiplicity bins of the left plot along the "diagonalized" and normalized T0 amplitude.

on the basis of acceptance simulation (see Table 3.3), vs the number of points involved. Data for three close choices of centrality are shown, the best choice is the one plotted by ○.

The trend present on most figures like Fig. 3.4, left, (analyzed separately for every spectrometer setting) is a flattening of the correlation slope for lower multiplicity bins, as compared to a perfect correlation, especially for those *bins* where central T0 distribution deviates significantly from the valid beam[14] one. The centrality thresholds are chosen based on the interpolation of the integrated T0 amplitude distribution dN/dA,

$$f(t) = \int_t^\infty \frac{dN}{dA}\, dA,$$

where dN/dA is normalized so that $f(-\infty) = c$. Recall that these runs are central triggered. Normalization of every run period is done with dN/dA of that period, i.e. the physics runs are normalized using their own dN/dA. The above mentioned 14 thresholds t_i come from solving numerically the 14 equations

$$f(t_i) = c_i. \tag{3.26}$$

[14]for the definition, see Subsection 2.4.1

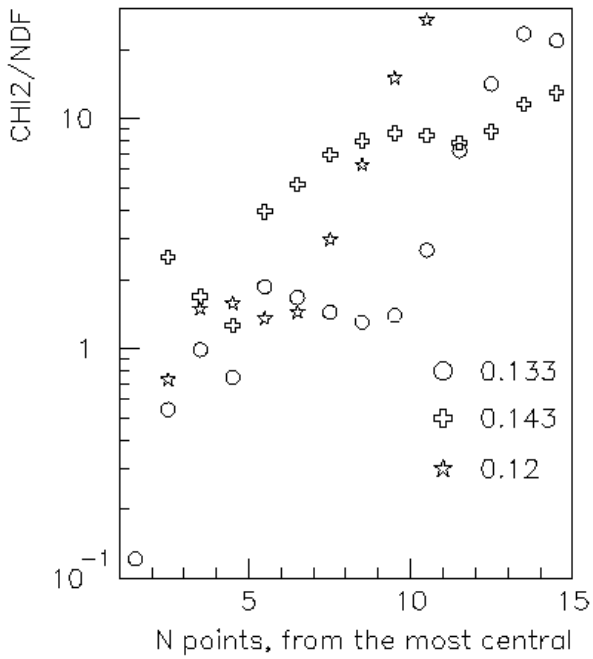

Figure 3.5: χ^2/NDF between actual correlations and the one expected on the basis of acceptance simulation, vs the number of points involved, for three different centralities.

From this it is clear that the bins to the left of the maximum in dN/dA contain a broader composition of true centralities. However, the correlation in $dN/d\eta$ between the Si and the spectrometer holds as long as the tracks in the numerator of equation (3.16) come from events which are unbiased representatives of their centrality class. Recall here that both T0 and spectrometer, but not the Si, enter the trigger. Can we hope that the events in question are unbiased in this sense ? No, the bin contents to the left of the maximum in dN/dA are the ones which deviate from the minimum bias T0 distribution *the most* ! Selection of these events is obviously the most affected by the trigger requirement of a spectrometer track. This explains why the correlation flattens out, i.e. the Si $dN/d\eta$ drops faster than the "same" quantity from the spectrometer.

3.2.8 Runs with Cherenkov veto

Clearly, the philosophy of the matching of non-identified $dN/d\eta$ can be implemented only for the runs with no Cherenkov veto. Statistics for kaons

in pion runs is too low for meaningful analysis of physics as a function of centrality. One has to learn how to determine centrality of runs with the Cherenkov veto in the trigger. The way I do it is the following.

I link the T0 thresholds for the kaon run with chosen T0 thresholds in the nearby pion run by requiring bin-by-bin (in T0 bins) correlation of Si between the two runs. Once centrality of the pion run is known (by varying the centrality to optimize the correlation between spectrometer and Si $dN/d\eta$, as described in the previous section), the link to the pion run is provided by Si. Now I vary centrality of the kaon run c_K, thus vary T0 bin boundaries and optimize the correlation of Si with respect to Si – between the kaon and pion runs. The kaon run centrality that maximizes the correlation is accepted. In other words, the kaon and pion samples are normalized to each other using the Si; samples of *identical* Si multiplicity are

1. selected by proper choice of T0 thresholds
2. normalized using *identical* values of trigger centrality.

3.2.9 Correction for the consequences of radiation damage in Si

Radiation damage in Si detectors is known [42] to result in

- an increase in dark current due to damage to the bulk Si
- a decrease in the collected charge signal due to charge trapping

Both effects make discrimination of particle track signals against the noise and dark current background more difficult. Technically, the problem shows up in the number of hits with signal above the threshold, not associated with particle tracks. These "fake hits" affect the multiplicity measurement. The effect calls for evaluation and correction. The correction algorithm (to be described below) deconvolutes the real distribution from the real+noise by sampling events according to the measured distributions of real+noise and noise, and consists of the following steps:

1. In the valid beam run, a sample of "pure noise" Si events was selected by cuts on all T0 tubes, combined with a 2D cut on the Si amplitude sum vs Si number of hits, using both sides of the Si detector and vetoing Si events with large total amplitude (but not with large number of hits !). Thus the distribution of the number of hit Si pads (delta-free part only) in these "pure noise" events was sampled. It is an asymmetric

distribution with maximum around 10 and a mean between 20 and 40, depending on the quality of the detector's performance. (An example can be found in Fig. 3.6, the middle panel, "Noise Si hits".) The asymmetry points to a "collective" nature of the effect responsible for the fake hits – in accordance with the features of the physics mechanism just discussed.

2. Knowing the "pure noise" distribution, and the "real+noise" distribution of the Si hits in the central trigger run, it is possible to reconstruct the "real" distribution, because the two known pieces of information determine it uniquely. The following "random purification" algorithm has been constructed:

   - make up a random number distributed according to the distribution of the number of fake hits. This random number will be called $NFAKE$. Randomly pick $NFAKE$ Si channels.
   - make up a random number distributed according to the distribution of "real+fake" hits. This random number will be called $NTOTAL$.
   - make up an integer random number uniformly distributed between 0 and the maximum number of working channels. This random number will be called $NPURE$. Randomly pick $NPURE$ channels.
   - Count channel numbers occupied by $NPURE$ OR $NFAKE$.
   - Compare it with $NTOTAL$.
   - If it equals $NTOTAL$, histogram $NPURE$.
   - Repeat the steps until sufficient statistics is obtained in the histogram of $NPURE$. By construction, the histogram so obtained represents the needed "rectified" distribution (with a caveat discussed below).

3. Transform the "real+noise" and "real" distributions into the Poissonian variable μ which characterizes multiplicity of tracks. Derive the correction factor, $\mu(real)/\mu(real + noise)$

4. Apply the correction directly to dN/dy

This ends the description of the correction method. Application of the method is illustrated by Fig. 3.6. [15]

[15] A caveat: the above described correction method is not rigorous because the simulation of effect is reduced to sampling from the distributions of observed $NTOTAL$

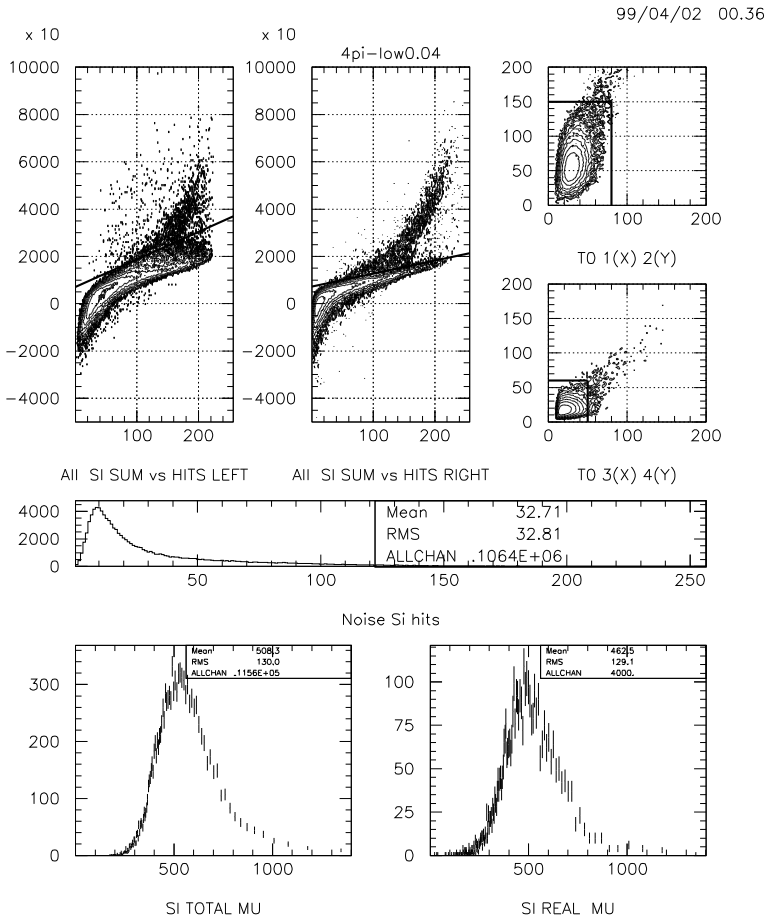

Figure 3.6: Illustration of the Si radiation damage correction algorithm in case of the 4GeV negative low angle setting, 4% centrality sample. From left to right, from top to bottom: SI ADC sum vs number of hits for the left and right parts of the detector in the valid beam run, with the non-interaction cut shown by the solid line; non-interaction cut on T0 signals in the valid beam run ; distribution of the number of Si noise hits in the valid beam run with the non-interaction cut; the "dirty" number of charged tracks in the physics run; the "purified" number of charged tracks. See text of Subsection 3.2.9

---

and $NFAKE$. In the procedure, $NTOTAL$ and $NFAKE$ are being sampled independently of each other. Useful pairs of $NTOTAL$ and $NFAKE$ are only those where $NTOTAL \geq NFAKE$. This means that the distribution of "useful" $NTOTAL$ and $NFAKE$, which will enter the correction procedure, will differ from the observable ones. However, in practice, for a central trigger run, in *most* cases

Table 3.4 gives the summary of corrections for all settings used in the analysis. The error bars on the correction factors were derived from the scatter of correction factors determined in 3 independent "random purification" runs, 1000 successful events each.

Setting	4% centr.	10% centr	Setting	4% centr.	10% centr
4k-low	0.91 ± 0.013	0.902 ± 0.011	4k+low	0.873 ± 0.002	0.864 ± 0.007
4k-high	0.943 ± 0.004	0.951 ± 0.011	4k+high	0.935 ± 0.008	0.931 ± 0.010
$4\pi^-$low	0.92 ± 0.01	0.921 ± 0.007	$4\pi^+$low	0.89 ± 0.02	0.876 ± 0.005
$4\pi^-$high	0.947 ± 0.002	0.934 ± 0.003	$4\pi^+$high	0.937 ± 0.01	0.934 ± 0.003
8k-low	0.955 ± 0.004	0.955 ± 0.002	8k+low	0.879 ± 0.013	0.879 ± 0.010
8k-high	0.930 ± 0.003	0.926 ± 0.006	8k+high	0.938 ± 0.005	0.947 ± 0.007
$8\pi^-$low	0.956 ± 0.008	0.948 ± 0.009	$8\pi^+$low	0.88 ± 0.016	0.872 ± 0.009
$8\pi^-$high	0.939 ± 0.008	0.9333 ± 0.0004	$8\pi^+$high	0.930 ± 0.013	0.931 ± 0.007

Table 3.4: Radiation damage correction. The factors listed here are applied directly to dN/dy.

Conclusions from the table:

1. Si in the the high angle setting performs better. This is natural, given the radiation damage mechanism of the problem, and the fact that the high angle setting was used earlier in the run.

2. As a general trend, the larger multiplicity bin (4%) needs less of a correction. This is because more real multiplicity leaves less room for the fake hits to contaminate the picture.

3.2.10 Results, systematic uncertainties, and conclusions.

The left and right halves of the Si detector had different number of working channels: 225 on the left side, 245 on the right, out of 256 on either side in total. In the analysis, a δ-free side of the detector is used for each sign. This is the "left" (Saleve) side for the positive, and "right" (Jura) side for the negative settings. After the radiation damage correction (Table 3.4) is applied, a comparison of the so corrected multiplicities, measured in the samples of identical centrality by the left and right parts of the detector, is performed to test the quality of the multiplicity measurement. In all cases we look at δ-free side, so it takes a change in the sign of magnetic field to compare the two sides.

$NTOTAL \gg NFAKE$. The result of this is that in case of the central runs, the bias coming from the condition $NTOTAL \geq NFAKE$ is negligible.

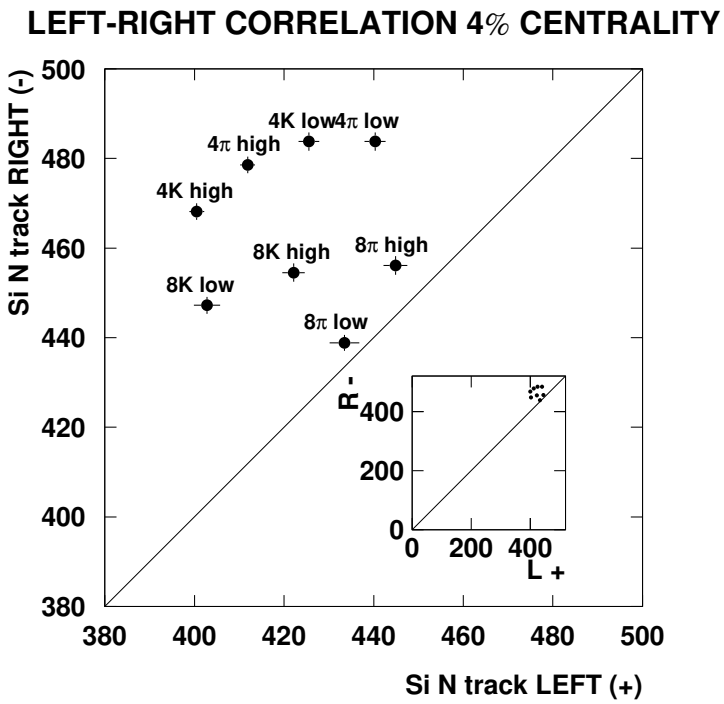

Figure 3.7: Comparison of the average charged track multiplicities measured independently by the left and right sides of the Si detector in the runs with different field sign. See text of Subsection 3.2.10.

Fig. 3.7 shows the comparison where each point represents a particular setting of the Cherenkov trigger, angle and magnetic field strength. The abscissa and the ordinate represent average multiplicity of charged tracks, measured in the 4% centrality sample, in the positive and negative runs respectively, by one half of the detector. Corrections for the dead pads ($=\times 256/(256 - N_{dead})$) are applied. This comparison reveals a systematic trend for the right side of the detector to give somewhat higher multiplicity. Most likely this is due to geometrical misalignment which was not calibrated out in the '95 data set. The center of gravity of the set of points is displaced from the diagonal representing the perfect correlation. In other words, the right side of the Si detector shows systematically larger multiplicity than the left side. The cause of this could be a horizontal displacement of the beam with respect to the Si. The magnitude of the left-right asymmetry in the mean number of tracks in the data samples of the same centrality $(\langle\text{Right}\rangle - \langle\text{Left}\rangle)/(\langle\text{Right}\rangle + \langle\text{Left}\rangle)$ – this number indicates by what fraction one would have to move an individual point, in order to eliminate the asymmetry) is about 3.5%, which is better than

the accuracy of a centrality calibration in an individual spectrometer setting (6-8%, see below). This level of systematics seems acceptable.

The estimate of the systematic uncertainty in the centrality determination is based on the following considerations. Once the set of T0 thresholds at fixed centralities is established for every physics setting, a comparison of the Si multiplicities between different runs can be performed for every centrality bin. The variance of the Si multiplicity $dN/d\eta$ between different run periods (at fixed centrality) characterizes the uncertainty of the absolute normalization. The fractional error bar of c is slightly better for high centrality points in agreement with my intuitive view that selection of high multiplicity samples and measurements of high multiplicity should be more reliable, because statistical fluctuation of a larger number is relatively smaller. For the interesting range of centralities ($c \leq 0.1$) the $\sigma(c)/c = 0.06$. For kaons, because the Si is involved twice, I multiply the above mentioned centrality uncertainty by $\sqrt{2}$. Table 3.5 summarizes the centralities.

momentum	4 GeV		8 GeV	
p_T setting	low	high	low	high
π^+	0.145± 0.008	0.152 ±0.009	0.17 ±0.01	0.116±0.007
K^+	0.145±0.011	0.152± 0.012	0.17 ± 0.014	0.116±0.009
π^-	0.129± 0.007	0.128±0.007	0.143± 0.008	0.127 ±0.007
K^-	0.129±0.010	0.128±0.010	0.145 ± 0.012	0.127 ± 0.010

Table 3.5: Trigger centrality c of the physics settings.

The advantage of this method of normalization is that it utilizes the Si *multiplicity* to solve the problem of normalization which is otherwise difficult to solve without making ungrounded assumptions, idealizing the experiment, e.g. the assumption that the top x% of T0 amplitudes are the top x% of the most central events, or that requirement of a spectrometer track in the trigger (with the "jaws" !) makes no effect on the centrality of the data sample so selected.

I have used RQMD simulation to link the acceptances of Si and spectrometer. I believe that any other normalization technique using T0 would, too, need simulations to fully understand the shape of minimum bias distribution in T0, and the effect of the spectrometer requirement in order to determine the trigger performance to the degree of realism needed for absolute normalization at the 6-8 % systematic error level. My approach reduces the simulation problem to the one which is quite tractable and relies on RQMD features not more sophisticated than the gross shape of $dN/\,d\eta$ distribution.

3.3 Track identification

A number of analysis steps have to be performed regardless of the particle identity one focuses on, and are common to π, K, etc. These are discussed in this section.

3.3.1 Double beam cut

The events of a beam particle crossing the target are distributed randomly in time, and there is a non-zero probability for more than one particle to come (and cause interactions) within a time interval shorter than our most sensitive equipment (i.e. the beam counters BC, see section 2.4.1) can resolve. This will look as a single event with abnormal properties, which we want to avoid. In the amplitude distribution of the PMT signals from the BC, one can clearly distinguish a secondary peak of the double beam events. The separation between the peaks is typically $3 \times FWHM$ of the single beam peak, so that clean discrimination is possible. The beam count B in formula 3.17 is corrected to represent the fraction of events after the double beam cut has been applied. The fraction of rejected events was, depending on the setting, between 2.9% and 5.4%, and known with high precision.

3.3.2 Track confidence level cut

NA44 tracks particles in the volume behind the magnetic channel. In the *MUL1* (see subsection 2.4.3) runs, the predominant majority of events are single track ones, and our tracking situation is the simplest possible in a heavy ion experiment. Which devices are used to track particles, and which information they provide, is described in subsection 2.8.1. The tracks are fitted with straight lines in three dimensions. In the process, one obtains two χ^2 values (vertical and horizontal), which, for given number of degrees of freedom NDF, characterize the quality of the fit. For given χ^2 and NDF, we calculate the probability that a random variable from a true χ^2 distribution with given NDF happens to be larger than the given χ^2 value. Examples of such distributions are shown in Fig. 3.8. We call this probability a *confidence level*, cut on it from below and call that a confidence level cut, or CL-cut. In experimental data (and in a realistic MC), due to a number of instrumental imperfections (detector off-set, fake hits, inefficiencies) and deviations of the real tracks from the idealistic fitting model (decays, conversions, multiple scattering) the percentage of tracks actually rejected by a sufficiently low CL-cut is much higher than what the "nominal" value of the confidence level implies.

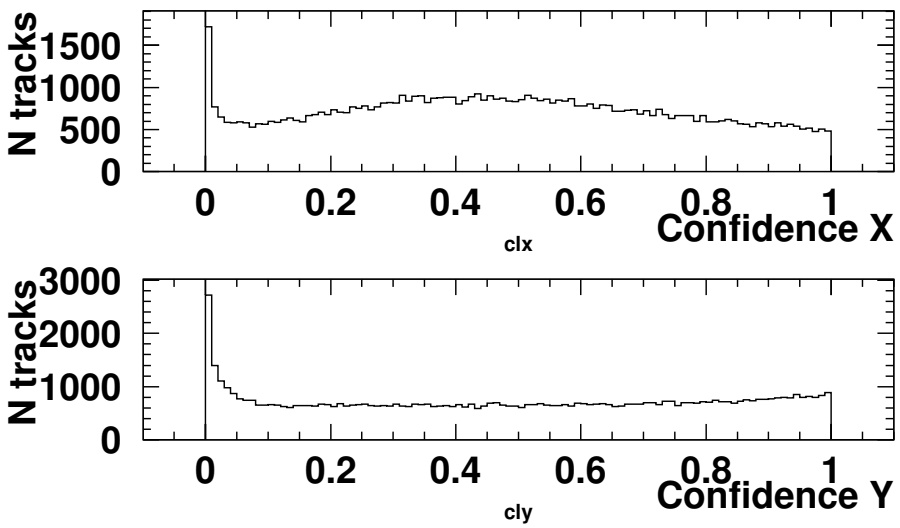

Figure 3.8: Track confidence level distribution in the positive strong field, high angle, pion trigger setting. Top: confidence level distribution in X. Bottom: confidence level distribution in Y.

To get rid of the unreliable tracks in the off-line analysis of the experimental data, I rejected tracks with *either* vertical *or* horizontal $CL < 10\%$. To evaluate the probability for a real track to be lost as a result of that, I ran MC simulation (thus modeling some of the imperfections mentioned above), and found out that the combined 2D CL-cut retains from 83% to 87% of the good tracks, slightly depending on the setting used. The corresponding corrections (known with 4 digit precision) were applied for each setting.

3.3.3 Pad Chamber in the trigger

In the NA44 design upgraded for the *Pb* beam running, the PC is an essential tracking device of limiting acceptance. In 1995, a PC hit [16] was required in the multiplicity trigger. This increases the rate of useful events, but reduces the efficiency due to inherent inefficiency of the chamber and the coincidence inefficiency. The following algorithm was used to find PC-related trigger inefficiency component:

1. Count good tracks in the run with PC in the trigger and normalize to the live beam.

[16] read out by Gasplex

2. Same in the run with no PC in the trigger, the rest of the trigger being the same

3. Take the ratio; apply as a multiplier to the particle yield.

If a couple of data sets with the trigger conditions required for the comparison could not be found, we used the one with the closest settings. Table 3.6

momentum	4 GeV		8 GeV	
p_T setting	low	high	low	high
π^+	1	1	1.13 ± 0.01	1
K^+	$8\pi^+$low	$8\pi^+$high	$8\pi^+$low	$8\pi^-$high
π^-	1.128	1	1.096 ± 0.009	1.219 ± 0.011
K^-	$4\pi^-$low	$8\pi^-$high	$8\pi^-$low	$8\pi^-$high

Table 3.6: Corrections for the PC in the trigger. "1" is used when PC was not part of the trigger. See section 3.3.3.

summarizes the corrections.

3.4 Pion identification

Here I discuss the issues specific to pion identification. Success of the UCAL calibration (whose usefulness had been hitherto limited by effects of radiation damage in the scintillator) enabled a correction for the inefficiency of pion PID due to a Cherenkov (*C2*) veto. This made it possible to obtain normalized yields of π^+ and π^- published in [26] and discussed in Chapter 4. Table 3.7 summarizes the conditions necessary to identify a track as a pion, in addition to those necessary to validate a track and described in Section 3.3.

3.4.1 Time of flight in pion identification

In the weak field setting, time of flight is helpful in separating pions from kaons. The principles of particle identification by the TOF cut and of performance evaluation for such a cut are discussed in subsection 3.5.1 and are not different for pions.

setting	$C2$	H3		$p_y, GeV/c$
		a, ns/slat	b, ns	
$4\pi^-$low	≤ 58	.04	3	$[.002, .008]$
$4\pi^-$high: 3614,15,16	≤ 64	.04	3	
$4\pi^-$high: 3617,18	≤ 64	-.04	-2	
$4\pi^+$low	≤ 74	.03	3	$[0.002, 0.008]$
$4\pi^+$high	≤ 74	.05	2	
$8\pi^-$low	see text	.04	4.	$[0.006, 0.01]$
$8\pi^-$high	see text	.04	4.	
$8\pi^+$low	see text	.04	4.	$[0.006, 0.01]$
$8\pi^+$high	see text	.04	4.	

Table 3.7: Summary of conditions used to identify a track as a π (PID cuts). The "$4\pi^-$high" setting was split in two because of different hodoscope calibrations. The a and b parameters are used to specify a slat-dependent hodoscope cut: $H3TOF < H3SLAT \times a + b$, where $H3TOF$ is time-of-flight, $H3SLAT$ is the slat number. Words "see text" refer to Subsection 3.4.4. The fields are left blank when a device was not used to apply a cut for the π identification.

3.4.2 UCAL calibration

The calibration was performed using the standard technique, documented elsewhere [43] and based on the measurement of Uranium's natural radioactivity via the scintillator stack. As a rule, the dedicated calibration measurements were taken before and after the physics running session. The pedestals were extracted from the out-of-burst information found on physics tapes. The time stability of the calibration constants over the period of Pb beam running was 5-10%, with a clearly seen systematic trend for the later calibration to give larger calibration constants. Stability of the pedestals was better than 0.5%.

DST software innovations were needed to cope with the problem of *radiation damage* in the scintillators. The radiation damage is known [44] to result in significant absorption of light in the scintillators and observable (factor of 2 in our device) dependence of the signal amplitude on the location of primary track. Hitherto, this problem had not been addressed in the NA44 DST production software.

The correction method chosen consisted in constructing a product of the two PMT amplitudes for each tower. The way it affects usage of the calibration constants is a subject of a special discussion and therefore is separated in Appendix A. In brief, to recalibrate, one must multiply tower's energy by a factor which depends on the attenuation length and therefore has to be mea-

sured. The measurement was performed by selecting the tower with maximum amplitude (to be able to ignore the effects of threshold and pedestal subtraction, the random details of propagation of shower tracks to the neighboring towers and sharing of light between the towers), then averaging separately the sum and the product of the tower's two PMT signals, and taking the ratio of sum to the square root of product. Only single track events were considered. Under some model assumptions, one can relate this ratio to the attenuation length in the scintillator. [17]

I estimated the attenuation length to be between 5 and 7 cm for most of the towers in 1996. It was seen to be systematically shorter in the EM section (which had no Cu plates in it [32]). 5 out of the 9 UCAL stacks were U/Cu/scintillator, and 4 were U/scintillator. The pure U stacks showed better performance and therefore seemed to have been restacked with newer scintillator. Comparing the sum/$\sqrt{\text{product}}$ ratios between 1995 and 1996, I noticed a systematic increase of about 5-7% in 1996, which indicated continuing deterioration [18].

A potential danger associated with using the product is that of losing the signal altogether if at least one of the PMTs gives no signal, as may happen due to the attenuation. However, the counterargument is that this never happens for (the nominal spectrometer momentum) electrons in the EM section and hadrons in the hadronic section. Therefore, the possibilities of identifying the electromagnetic events by high EM signal, selecting hadrons by high signal in the hadronic section and vetoing any background by low signal remain unaffected. I studied the issue quantitatively, selecting (by Cherenkovs, *C2* at 14.7 PSI) a sample of electrons and a sample of protons and kaons in a 4 GeV positive setting, and found that for the true electrons the inefficiency due to making a product instead of a sum is $(0.2 \pm 0.1)\%$, which is comparable with the inefficiency due to non-interacting (the non-interacting probability is $\exp(-6.4)$). For p and K, such kind of inefficiency in the hadronic section is less than 1×10^{-4} due to the larger signal from these particles.

Out of a variety of other possible correction methods, the following two were tried:

1. correction based on comparison of the left and right PMT signals

2. correction based on the external tracking

[17] as discussed in detail in Appendix A

[18] An increase in the the sum/$\sqrt{\text{product}}$ means that the attenuation length decreases, see Appendix A.

I concluded that it would be more difficult to achieve a performance comparable to that of the product method using 1) or 2) or their combination.

3.4.3 Correcting for the electron veto inefficiency.

The problem of electrons misidentified as pions is non-negligible in the low field settings only, because the spectrum of electrons falls rapidly with momentum. The electron veto correction factor was determined using supplementary PID provided by the UCAL electromagnetic/hadronic ratio. The question of how tight a cut one needs to apply in order to get the supplementary PID is of little importance, since the electron veto inefficiency determination operates entirely *within* the sample which satisfies this tough PID criterion. This is true as long as devices used for the veto and for the supplementary PID are uncorrelated. The requirement of $UCHAD/UCEM > 10$ identifies track as a reliable hadron and constitutes the tough, clean supplementary PID. Fig. 3.9 shows how the ratio of tracks that exceed the pion $C2$ veto cut to those that do not (let me denote this as $N(\bar{C}2)/N(C2)$) changes with $UCHAD/UCEM$. Such figures were obtained for all low field settings and different centralities. They all have the same characteristic pattern: the ratio falls with $UCHAD/UCEM$, and then becomes flat after $UCHAD/UCEM$ exceeds a certain threshold[19]. From this we conclude that

- a high signal in $C2$, just as a low ratio $UCHAD/UCEM$, both characterize the same group of tracks – obviously, the $e^+(e^-)$ ones
- contribution of the $e^+(e^-)$ goes down to zero when $N(\bar{C}2)/N(C2)$ gets flat, and thus one chooses the safe $UCHAD/UCEM$ cut
- for true hadrons, the reasons that cause $C2$ to fire are unrelated to UCAL since $N(\bar{C}2)/N(C2)$ is flat above 10.

Thus we have justified the electron veto correction obtained via UCAL. It is the factor

$$1 + N(\bar{C}2)/N(C2) \tag{3.27}$$

with the counting errors in both N counts propagating into the systematic error of the pion yields.

[19]This was not seen until I calibrated out the position dependence of the UCAL signal, significant due to the radiation damage in the scintillator (see Subsection 3.4.2).

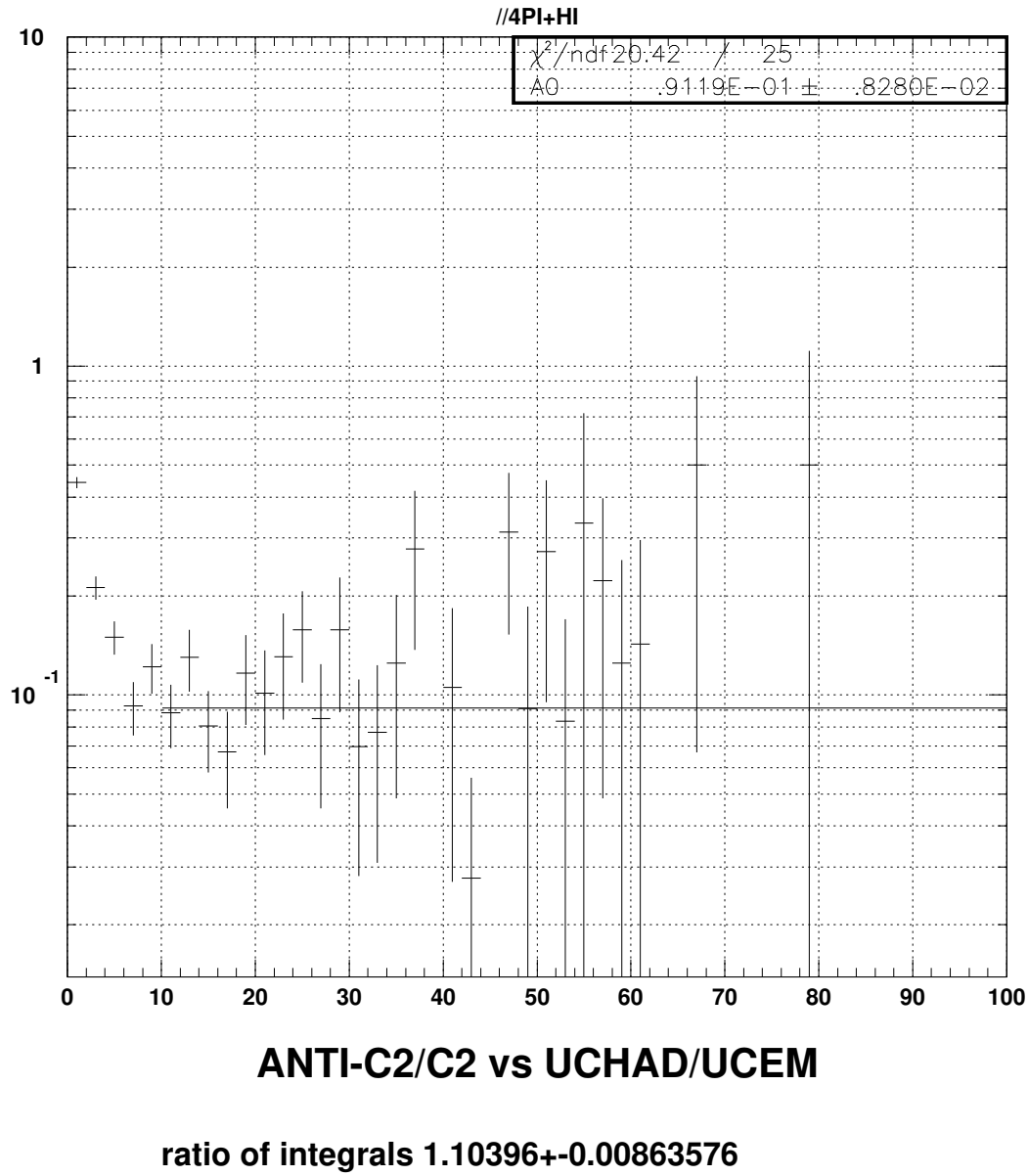

Figure 3.9: $N(\bar{C}2)/N(C2)$ (see text of subsection 3.4.3) as a function of $UCHAD/UCEM$ for the weak field, high angle, positive polarity setting.

3.4.4 Counting pions in the strong field setting.

In the strong field setting, to identify pions directly one needs to require a $C2$ firing (see Fig. 2.5 and discussion of the Cherenkovs in Subsec-

setting	Cherenkov veto correction		H3 TOF
	10%	4%	
$4\pi^-$low	1.93 ± 0.07	1.94 ± 0.07	1
$4\pi^-$high	1.239± 0.014	1.23 ± 0.02	1
$4\pi^+$low	1.57 ± 0.05	1.59 ± 0.08	0.996
$4\pi^+$high	1.096± 0.006	1.11 ± 0.01	1.021
$8\pi^-$low	N/A	N/A	1
$8\pi^-$high	N/A	N/A	1
$8\pi^+$low	N/A	N/A	0.9936
$8\pi^+$high	N/A	N/A	0.9957

Table 3.8: Multiplicative corrections to the π yields related to the process of particle identification for the samples of top 10% and top 4% centrality.

tion 2.4.4). However, it is desirable to avoid the uncertainty associated with the Cherenkov's efficiency, which would have entered the game had $C2$ been required to fire. Notice that sorting out p ($\bar{p}$) off-line by vetoing $C1$ and $C2$ and using TOF can be done cleanly and reliably even in the strong field settings. Having done that, we are left with a sample of K and π[20]. For this sample, we can obtain distributions with respect to the kinematic variables of a π by applying a pionic acceptance correction [21]. Then, we obtain inefficiency-corrected, clean K distributions with respect to the pionic y and k_T, where a pionic acceptance correction is used. Finally, we subtract the kaon component in the distributions:

$$\frac{dN(\pi)}{dy_\pi} = \frac{dN(\pi + K)}{dy_\pi} - \frac{dN(K)}{dy_\pi} \tag{3.28}$$

Clearly, the y above can be replaced by any kinematic variable.

3.5 Kaon identification

Here I discuss the issues specific to kaon identification. Table 3.9 summarizes the conditions necessary to identify a track as a pion, in addition to those necessary to validate a track, described in section 3.3.

[20]We neglect $e^+(e^-)$ for the reasons outlined in Subsection 3.4.3.

[21]Particles of different mass and life time have different acceptance corrections, and they are calculated separately. By "pionic" one I mean the one calculated for pions.

setting	$C1$	$C2$	H3		H2		$p_y, GeV/c$
			a	b	a	b	
$4K^-$low	$\leq$70	$\leq$60	.1	10	0.	10	$[0.002, 0.009]$
$4K^-$high	$\leq$77	$\leq$74	.1	10	.083	7	
$4K^+$low	$\leq$75	$\leq$65	.1	10			$[0.002, 0.009]$
$4K^+$high	$\leq$77	$\leq$74	.1	10			
$8K^-$low		$\leq$59	.067	1.5			$[0.006, 0.01]$
$8K^-$high		$\leq$63	.05	2.			
$8K^+$low		$\leq$59	.067	1.5			$[0.006, 0.012]$
$8K^+$high : K calibr		$\leq$66	.06	1.			
$8K^+$high : p calibr		$\leq$66	-.06	-1.5			

Table 3.9: Summary of conditions used to identify a track as a K (PID cuts). The "$8K^+$high" setting was split in two because of different hodoscope calibrations. The a and b parameters are used to specify a slat-dependent hodoscope cut: $H3TOF < H3SLAT \times a + b$, where $H3TOF$ is time-of-flight, $H3SLAT$ is the slat number. The fields are left blank when a device was not used to apply a cut for the π identification.

3.5.1 Time of flight in kaon identification.

The time of flight cut is used to separate K^+, K^- from $p, \bar{p}$ respectively in the strong and weak field setting of the spectrometer at both arm angles. Since only particles with momenta within a narrow range are accepted by the spectrometer, [22] velocity

$$v = \frac{p}{\sqrt{m^2 + p^2}} \tag{3.29}$$

becomes a measure of particle's mass m. v itself is measured by time interval between the interaction (provided by beam counter [23]) and the scintillation hodoscope *H3*. [24] K/p separation is therefore achieved by a TOF cut. A good cut is slat dependent as velocity and slat number are correlated by virtue of the spectrometer's analyzing power. The problem of this cut's cleanliness/efficiency becomes noticeable only in the strong momentum setting. By *performance evaluation* I mean a procedure which allows me to answer two questions:

[22] data on momentum acceptance is found in Table 2.2

[23] see section 2.4.1 for description

[24] see section 2.4.1 for description

setting	Cherenkov veto correction		H3 TOF
	10%	4%	
$4K^-$low	2.2 ± 0.7	3.1 ± 0.8	N/A
$4K^-$high	1.46± 0.05	1.56± 0.09	N/A
$4K^+$low	2.61± 0.21	2.91± 0.34	N/A
$4K^+$high	1.22± 0.04	1.20± 0.05	N/A
$8K^-$low	2.08± 0.16	2.4 ± 0.6	1.056
$8K^-$high	1.10± 0.04	1.09± 0.04	1.016
$8K^+$low	2.15± 0.12	2.4 ± 0.4	1.086
$8K^+$high	1.12± 0.01	1.15± 0.05	1.0028

Table 3.10: Corrections to the K yields related to the process of particle identification for the samples of top 10% and top 4% centrality.

- how many real particles get lost due to the cut?
- how many unwanted ones get misidentified ?

The TOF distribution is Gaussian and therefore easy to analyze. The algorithm consists of the following steps:

1. Select a sample of tracks of desired PID, using *all* cuts except for the hodoscope cut.
2. For this sample, fill separate TOF histograms for every slat.
3. Fit each slice with a sum of two Gaussians; assume that TOF distribution is independent of PID and take the sigmas to be the same.
4. For the two Gaussians with known separation, find the contamination and the loss due to the cut.

The corrections can be found in Table 3.10.

3.5.2 Correcting for pion/electron veto inefficiency

At this point we turn again to the figures (Fig. 2.4 and Fig. 2.5) that illustrate the difference in the approaches to kaon identification in different spectrometer settings. As was already discussed in Section 2.4, a Cherenkov veto ($\bar{C}$) was used to obtain kaon-enhanced data samples. The price of the high cleanliness of a PID with $\bar{C}$ is its high inefficiency: any event resulting in a firing of the vetoing Chereknov's counter (a passage of any charged particle of sufficient velocity through the counter's aperture) may result in a loss of a

kaon. In particular, such can be the outcome of a coincidence of the kaon with a pion or an electron in the counter's acceptance. To evaluate this inefficiency, we take the following steps:

1. On-line: obtain a sample without the $\bar{C}$ veto and a sufficient statistics of kaons.

2. Off-line: in the sample without veto, find a way of *counting* [25] the kaons with and (non-trivial !) without the veto.

The counting of the rejected kaons can be possible in presense of a device sensitive to the difference between kaons and lighter particles. Presense of a device capable of *identifying* kaons independently of the Cherenkovs is ideal. Such an ideal case is realized in the weak magnetic field setting, (see Fig. 2.4) where the m^2 measurement (due to the good time-of-flight resolution) allows one to tell kaons from lighter particles even in the absence of the veto. The inefficiency correction factor is therefore easily calculable:

$$1 + \frac{N(K)_{lost}}{N(K)_{detected}} \tag{3.30}$$

The case of a strong field setting (see Fig. 2.5) is complicated by the fact that a particle lost due to the veto is not necessarily a kaon, but a kaon or a lighter particle. The lighter particle is most likely a pion and will be called so in the following discussion. It is possible to *count* the lost kaons without identifying them, taking advantage of the fact that the kaon and pion peaks in the m^2 spectrum of vetoed tracks (see Fig. 3.10) are separated, even though they overlap. In order to subtract the pions from all vetoed tracks, we select a clean sample of undoubtedly light tracks (π+e) from a sample of good events with a single hit in hodoscopes $H2$ and $H3$ and only one reconstructed track, by requiring a large (characteristic of a pion) signal in $C1$. Since this requirement is highly selective, we use the shape of the distribution $dN_{clean,light}/\,dm^2$ so obtained, but not the magnitude of the probability it represents. Therefore, we seek a multiplier Υ that allows us to subtract the light particle distribution without remainder to obtain the number of the vetoed K and p only. We do it by dividing the "+" histogram on Fig. 3.10 by the clean light track distribution (not shown). Flatness of the ratio so obtained (shown as $\diamond$) is to be expected in the range of m^2 where the light particle line shape selected is representative

[25] To emphasize: we do not have to *identify*, but merely have to *count* the rejected kaons for this task.

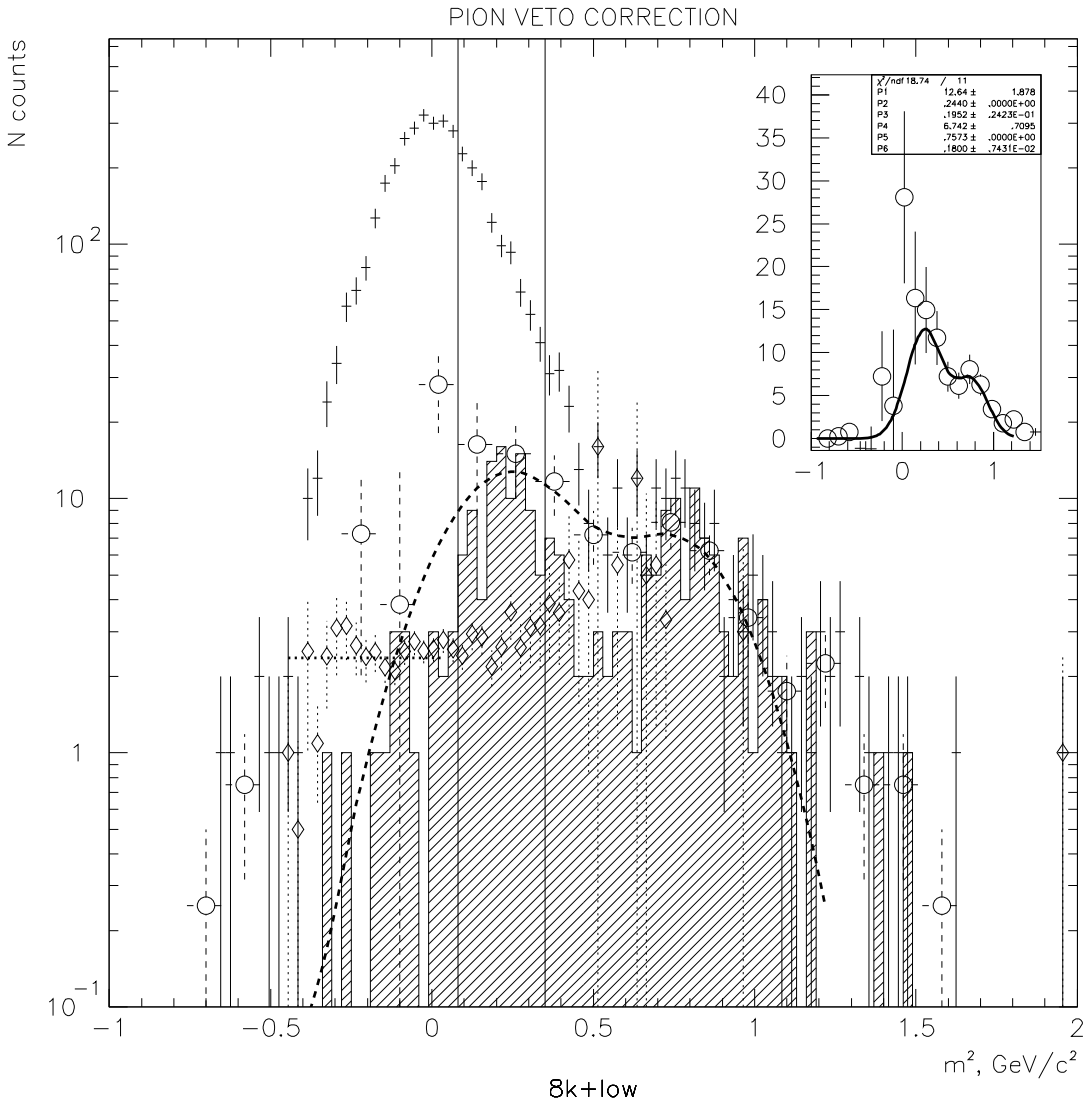

Figure 3.10: Correcting for the Cherenkov veto inefficiency in the strong field case, 4% most central events. The number of rejected kaons is evaluated by subtracting the clean pion m^2 line shape scaled by a proper multiplier Υ. $+$ = all vetoed tracks $dN_{lost}/\,dm^2$; $\diamond$ = ratio of the pure pion line $dN_{clean,light}/\,dm^2$ to the "all vetoed tracks" distribution, $\circ$(also in the insert) $= dN(K+p)_{lost}/\,dm^2$ obtained as "all vetoed tracks" minus Υ - scaled pion line (see Eq. 3.31). The shaded histogram shows the m^2 distribution of K/p tracks which were not vetoed.

case	centrality	PID	p_T extrapolation	total
representative	0.081	0.042	0.0067	0.098
maximum in any setting	0.081	0.25	0.063	0.26
minimum in any setting	0.058	0.014	0.0042	0.058

Table 3.11: Summary of fractional systematic errors to the normalized yields. Positive kaons in the weak field high angle spectrometer setting are chosen as "representative". Maximum and minimum uncertainties indicate the range; the overall systematic uncertainty was evaluated for each setting separately.

of the sample we want to subtract. We fit the ratio in the flat region to obtain the required multiplier Υ, and subtract the light particle line shape:

$$\frac{dN(K+p)_{lost}}{dm^2} = \frac{dN_{lost}}{dm^2} - \Upsilon \frac{dN_{clean,light}}{dm^2} \tag{3.31}$$

The histogram plotted on Fig. 3.10 by $\circ$ represents the m^2 distribution of vetoed K and p only, $dN(K+p)_{lost}/\,dm^2$. To get $N(K)_{lost}$, we pick an m^2 window (vertical lines on Fig. 3.10). By solving the standard problem of interpreting a sum of two Gaussian peaks as "signal" + "background", K being the signal and p the background, one finds that the "lost" kaons in the window are 98-99% clean of protons.

3.6 Summary of the systematic uncertainties

Here I briefly summarize the systematic errors to the normalized yields and distributions of charged pions and kaons. For more detailed discussion see the appropriate section of this chapter. The systematic uncertainty in the calculation of the Cherenkov veto inefficiency is dominated by the *statistical* uncertainty of the "lost" particle counting (see Eq. 3.30).

Table 3.6 shows the sources of systematic uncertainty on dN/dy. The error in the extrapolation due to uncertainty in the slope parameter(s) is small because over 95% of particles around mid-rapidity have p_T in the range covered by one of the two angle settings. Consequently, the systematic error in dN/dy is dominated not by the extrapolation, but by uncertainties in determination of centrality and particle ID efficiency. The systematic uncertainty due to centrality was determined from the setting-by-setting variation of acceptance corrected yields of charged tracks, without requiring particle ID. The uncertainty due to PID efficiency corrections arises from statistical uncertainties in the particle counts in untriggered runs used to determine the veto correction.

Chapter 4

Inclusive single particle results for π and K. Their meaning.

We start this chapter with a brief introduction into strangeness enhancement as a QGP signature, after which the results of our kaon and pion measurements [26] will be summarized. Discussion of the meaning of those results in the overall context of the AGS and SPS strangeness studies (both experimental and theoretical) will complete this Chapter. The technique of the NA44 measurements has been already explained in Chapters 2 and 3.

4.1 Strangeness as a deconfinement signature

In the deconfined phase, partonic reactions change the number of strange quarks:

$$g + g \leftrightarrow s + \bar{s}, \tag{4.1}$$

$$q + \bar{q} \leftrightarrow s + \bar{s}, \tag{4.2}$$

where q and $\bar{q}$ denote quarks and antiquarks, and g – gluons. In the hadronic gas, the relevant processes are

$$\pi + \pi \leftrightarrow K + \bar{K} \tag{4.3}$$

$$\pi + N \leftrightarrow Y + K \tag{4.4}$$

$$N + N \leftrightarrow N + Y + \bar{K} \tag{4.5}$$

$$N + N \leftrightarrow N + N + \bar{K} + K \tag{4.6}$$

Here Y stands for a Λ or Σ hyperon, and kaons are $K = \bar{q}s$ (K^-, $\bar{K^0}$) and $\bar{K} = q\bar{s}$ (K^+, K^0). Reaction 4.4 may proceed through intermediate stages involving

heavy resonance formation, their interaction with the medium, excitation and decay through the $Y + K$ channel. In that case, the right-hand side may be not the only product.

The first proposal of a strangeness-based QGP signature was made by Rafelski and Hagedorn [20] in 1981. It did not involve a detailed analysis of hadrochemical kinetics, but was based on a statistical model approach advocated by Hagedorn [45]. Assuming equilibration of strangeness in QGP, they estimated that for the ratio of baryochemical potential [1] to temperature $\mu/T \sim 6-7$[2], one could expect ratio $\bar{s}/\bar{q} \sim 5$. The enhancement was expected to be stronger for higher baryochemical potential since that would exclusively suppress $q\bar{q}$ (and not $s\bar{s}$) production.

In a subsequent work, Rafelski and Müller [21] used lowest order perturbative QCD calculations to obtain the production rate of $s\bar{s}$ pairs in reactions with quarks and gluons in the initial state. They found that the predominant fraction of strangeness is produced in gluon-gluon reactions, and that consequently the strangeness per baryon number in QGP *saturates* over the time of the order of 10 fm/c.

Besides that, it was pointed out [20] that "some of the numerous $\bar{s}$ may, instead of being bound in a $q\bar{s}$ kaon, enter into a $\bar{q}\bar{q}\bar{s}$ antibaryon and, in particular, a $\bar{\Lambda}$ or $\bar{\Sigma}^0$." In hadronic gas, such particles can be created only in direct pair production reactions, which is kinematically suppressed by a high threshold. This makes strange antibaryons the most *characteristic* strangeness-related QGP signature. However, it was also emphasized [46] that K^+ abundance deserves attention because "about half of the $\bar{s}$ quarks from the plasma will be used in making K^+ mesons, the other half contributing to $K^0 \pm \bar{K}^0$ states, and a smaller, and for this consideration, insignificant number of $\bar{s}$ quarks being contained in the antistrange baryons; $\bar{s}\bar{s}\bar{s}$, $\bar{s}\bar{s}\bar{q}$, $\bar{s}\bar{q}\bar{q}$, or $s\bar{s}$ mesons, as it is self-evident that such states have a much smaller chance of emerging from a baryon-rich plasma than does a $\bar{s}q$ meson." On the contrary, kaons with an s quark ($K^- = s\bar{u}$, $\bar{K}^0 = s\bar{d}$), due to their large strangeness exchange cross-section in hadronic gas, represent mainly the post-hadronization stage in the evolution of the system. Because K^0 and $\bar{K}^0$ are mixed in the decay eigenstates K_S and K_L (so that no distinction can be made between the s and $\bar{s}$ meson), neutral kaons are less interesting than K^+ from the QGP signal point of view [46].

---

[1] parameter of statistical models needed to account for the fact that the total baryon number in the system is fixed (conserved).

[2] too high for the SPS freeze-out conditions, but the authors of that early work [20] considered lab energies up to $E/A \approx 4GeV$

4.2 Hadrochemistry

Here we summarize the present understanding of how inelastic hadronic rescattering in a thermal hadron gas can change flavour composition and influence relative abundances of particle species.

Koch, Rafelski and Muller [24, 22] pointed out that in the thermally equilibrated fireball, the usual reaction

$$N + N \leftrightarrow N + Y + \bar{K}, \tag{4.7}$$

where $Y = \Lambda$ or Σ, plays almost no role because, first, the majority of collisions are πN and $\pi\pi$, not NN, and second, the following πN and $\pi\pi$ reactions have lower threshold :

$$\pi + N \leftrightarrow \bar{K} + Y \tag{4.8}$$
$$\pi + Y \leftrightarrow \bar{K} + \Xi \tag{4.9}$$
$$\pi + \Xi \leftrightarrow \bar{K} + \Omega \tag{4.10}$$
$$\pi + \bar{N} \leftrightarrow K + \bar{Y} \tag{4.11}$$
$$\pi + \bar{Y} \leftrightarrow K + \bar{\Xi} \tag{4.12}$$
$$\pi + \bar{\Xi} \leftrightarrow K + \bar{\Omega} \tag{4.13}$$
$$\pi + \pi \leftrightarrow K + \bar{K} \tag{4.14}$$

For charged kaons, $\bar{K}$ is K^+ $(u\bar{s})$ and K is K^- $(s\bar{u})$. In $Pb + Pb$ collisions at SPS, the $\bar{p}/p$ ratio was reported to be around 0.07 [47, 48], and p/π around 0.16 (as seen by collecting the data from [47, 48] and the present work [26]). Therefore it is clear that the reactions above enhance K^+ whereas K^- is little affected. The effect of the pion rescattering 4.9,4.10 on the Λ, Σ and Ξ will be depletion, since the left hand side of these reactions is a more common state.

There is another side to the question of how rescattering affects strange particle yields. The *strangeness exchange* reactions

$$K + N \leftrightarrow Y + \pi \tag{4.15}$$
$$K + Y \leftrightarrow \Xi + \pi \tag{4.16}$$
$$K + \Xi \leftrightarrow \Omega + \pi \tag{4.17}$$
$$\bar{K} + \bar{N} \leftrightarrow \bar{Y} + \pi \tag{4.18}$$
$$\bar{K} + \bar{Y} \leftrightarrow \bar{\Xi} + \pi \tag{4.19}$$
$$\bar{K} + \bar{\Xi} \leftrightarrow \bar{\Omega} + \pi \tag{4.20}$$
$$\tag{4.21}$$

are exothermic when they proceed from the left to the right. When the system cools down, kaons and hyperons are already present and cooling down will shift the balance to favour the right hand side.

4.3 Subtleties and controversies related to the strangeness signature

As was pointed out originally by Redlich *et al.*[49] and later by Kapusta and Mekjian [52], McLerran [50], and Baym [51], strangeness per unit of entropy is *larger* in the hadron gas in flavour equilibrium than it is in the plasma, due to the fact that a significant fraction of entropy in the plasma is carried by gluons. During the return to the confined state, the entropy is conserved while the disappearing free gluons give birth to mesons. The K/π ratio immediately after the phase transition approximates the strangeness to entropy ratio in QGP well. The problem however is that the K/π ratio we measure reflects the rescattering in the hadron gas phase before the system freezes out. In particular, reaction 4.8 works to convert some pions into kaons.

Thus, an observation of strangeness enhancement should be regarded as an indirect and conditional QGP signature. At most it can testify to the state of flavour equilibrium reached by the hadron gas, and it remains to be proven that such a state was reached via a descent from a deconfined state. Kinetic theory calculations of the number of strange quarks in the hadronic gas resulting from the deconfined phase have been carried out in [22]. It was concluded that on the time scale of the collision (10 fm/c), the hadron gas can not equilibrate its flavour composition unless a transient QGP phase boosts the process. In the baryonic medium, kaons ($\bar{s}q$) equilibrate faster than strange antibaryons.

The topic of flavour equilibrium is approached by fitting particle ratios with statistical models. Statistical models are based on the following postulates[75]:

- In a certain volume, a system of N secondary particles is formed as a result of strong interaction of the primary particles
- N is large enough to justify statistical description
- By the time when the statistical equilibrium is established (relaxation time), the states of individual particles are statistically independent. In other words, the only remaining correlations are due to energy-momentum

conservation. (To avoid misunderstanding: the effect of HBT interference of like particles, used to characterize system size, is a final state effect and it remains in this case[53]!)

It has been noticed that the rarer a particular baryon is, the less reliable its description via statistical model becomes[73]. From a logical point of view, even a perfect fit of data with a statistical model is merely a consistency check, rather than a proof of equilibration, since the statistical assumption inherent in such a model cuts off alternative explanations of the same behaviour by construction.

There is, moreover, another important component in resolving the dilemma between the QGP/non-QGP strangeness production scenarios, which makes the issue more complicated than just a choice between the purely hadronic and the QGP flavour equilibration mechanism. Very early in the collision, some strangeness production takes place in the energetic primary collisions. Its physics is neither that of the thermalized hadron gas, nor that of the thermalized QGP. Mattiello *et al.* (the RQMD group) showed [54] that kaon production in the primary hard collisions explains the enhanced production of K^+ in the $Si + Au$ collisions at AGS. Via color rope mechanism[57], RQMD can also explain Λ and $\bar{\Lambda}$ production at the SPS[69].

4.4 What the data say

As far as the motivation for studying kaon production is concerned, the following points can summarize the discussion :

- Because kaons are the lightest (and therefore the most abundant) strange particles, the strangeness content of the final state can not be understood without measuring kaons.
- On the other hand, the kaon abundance alone does not permit to draw conclusions about presence or absence of the deconfined phase in the evolution of the system.

For the former reason, and in the light of the latter caveat, we have carried out a study of kaon production in $Pb + Pb$ collisions at SPS [26].

Tables 4.1 and 4.2 give the m_T slope parameters and values of dN/dy for kaons and pions. The measured distributions for charged kaons of both signs in transverse kinetic energy and rapidity, are shown on Fig. 4.1

The $1/m_T$ scaled spectra appear exponential in accordance with the behaviour typical for thermalized ensembles of interacting particles, or for particles in whose production the phase-space constraints played the dominant role

PID	y interval	T (MeV)	$\sigma(T)$ stat., syst. (MeV)
K^+	2.3-2.6	230	$\pm$ 8 $\pm$ 14
K^+	2.4-2.9	254	$\pm$ 4 $\pm$ 7
K^-	2.3-2.6	259	$\pm$ 8 $\pm$ 12
K^-	2.4-2.9	245	$\pm$ 7 $\pm$ 6

Table 4.1: Inverse slope parameters T.

PID	y interval	dN/dy	$\sigma(dN/dy)$	PID	y interval	dN/dy	$\sigma(dN/dy)$
K^-	2.7-2.9	21.5	$\pm$ 7.5	K^+	2.7-2.9	37.1	$\pm$ 5.4
	2.3-2.5	18.7	$\pm$ 1.9		2.3-2.6	27.2	$\pm$ 2.5
	3.1-3.4	15.4	$\pm$ 4.1		3.1-3.4	29.7	$\pm$ 5.6
	2.6-2.8	14.8	$\pm$ 1.4		2.6-2.8	33.6	$\pm$ 3.1
π^-	3.3-3.7	176	$\pm$ 14	π^+	3.3-3.7	160	$\pm$ 15
	2.6-2.9	193	$\pm$ 12		2.6-2.9	153	$\pm$ 10
	3.5-4.0	173	$\pm$ 12		3.5-4.0	145	$\pm$ 10
	2.6-2.9	173	$\pm$ 15		2.6-2.9	164	$\pm$ 13

Table 4.2: Particle distributions in rapidity for top 4% centrality. Every spectrometer setting provides an independent measurement. Settings overlapping in y are listed separately. Statistical and systematic errorbars are added in quadrature to form $\sigma(dN/dy)$ listed.

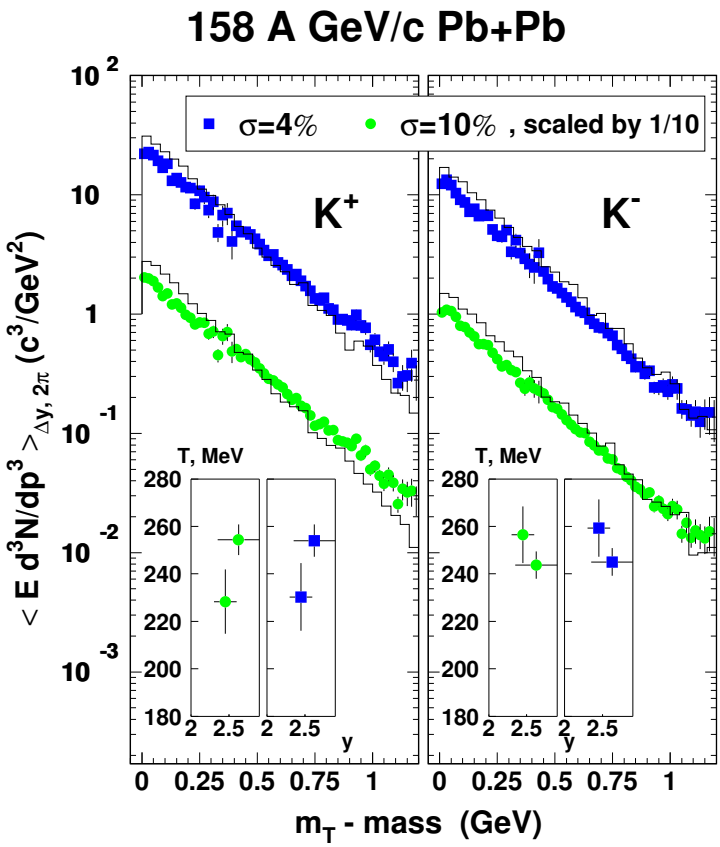

Figure 4.1: Measured transverse kinetic energy distributions of positive and negative kaons for the 4% and 10% most central of Pb+Pb collisions. Two spectrometer angle settings meet at $m_T - m = 0.35$ GeV. The fits follow the form $1/m_T\, dN/\, dm_T \propto exp(-m_T/T)$, where $m_T = (m^2 + p_T^2)^{1/2}$. y ranges of the fits are given in Table 2 and are indicated by the horizontal errorbars in the inserts. RQMD predictions for $|y - y_{CM}| < 0.6$ (i.e., within NA44 acceptance) are shown as histograms.

[55]. The spectra were fit with an exponential in $(m_T - m)$, and the resulting slopes are shown in the inserts in Fig. 4.1. The inverse slopes of the K^+ and K^- spectra are the same, within errors. Our event selection is sufficiently central that the slopes show no dependence on multiplicity.

In Fig. 4.2, it is clear that many fewer kaons are produced than pions, as was observed in $p+p$ collisions. There are approximately twice as many positive as negative kaons produced. This is typical for baryon rich systems, and was also observed in $p+p$ collisions. Preliminary[3] NA49 measurements of K^+ and K^- dN/dy in $Pb+Pb$ [56] are consistent with those reported here. Both Fig. 4.1 and 4.2 compare the data with predictions of the transport theoretical approach RQMD [57]. While RQMD tends to overpredict both the K^+ and K^- yields, for K^- the discrepancy appears to be larger. Running RQMD in the mode which does not allow the hadrons to rescatter (shown by the dashed line on the figure) decreases the number of kaons produced. This result illustrates the importance of the secondary scattering to the total kaon yields. Measurements of proton production at midrapidity[48] and of the $p-\bar{p}$ rapidity distribution[58] indicate that RQMD somewhat overpredicts the degree of baryon stopping. Because πN inelastic collisions can produce kaons, an increase in stopping translates naturally into kaon enhancement at midrapidity. The data show that the hadron chemistry via secondary scattering, as implemented in RQMD, successfully reproduces the general trends in the hadron distribution. However, the hadron chemistry in the model is not quantitatively correct.

Strangeness enhancement compared to the interpolated [59] pp collision data, shown as the line, is seen in Fig. 4.3. The solid point, corresponding to ISR data at midrapidity, indicates the extent of the enhancement due to the midrapidity cut on the particles. The figure shows that K^+/π^+ is enhanced in high multiplicity heavy ion collisions, but K^-/π^- is consistent with $p+p$ values. Higher multiplicity, or more central collisions, yields larger enhancement, independent of $\sqrt{s}$.

Secondary hadronic interactions of the type $\pi + N \leftrightarrow Y + \overline{K}$ are important for the strangeness production [57, 61], and their rate is proportional to the product of the participant's effective concentrations.

Fig. 4.4 shows the dependence of the K^+/π^+ ratio on the product of rapidity densities of the two ingredients of the associated strangeness production, N (represented by p) and π^+ in the AGS [62] and SPS [63] data, and RQMD calculations. This "$p \times \pi$" product serves as an observable measure

[3]To the best of my knowledge as of July 2001, these NA49 data have not yet been published in the refereed press

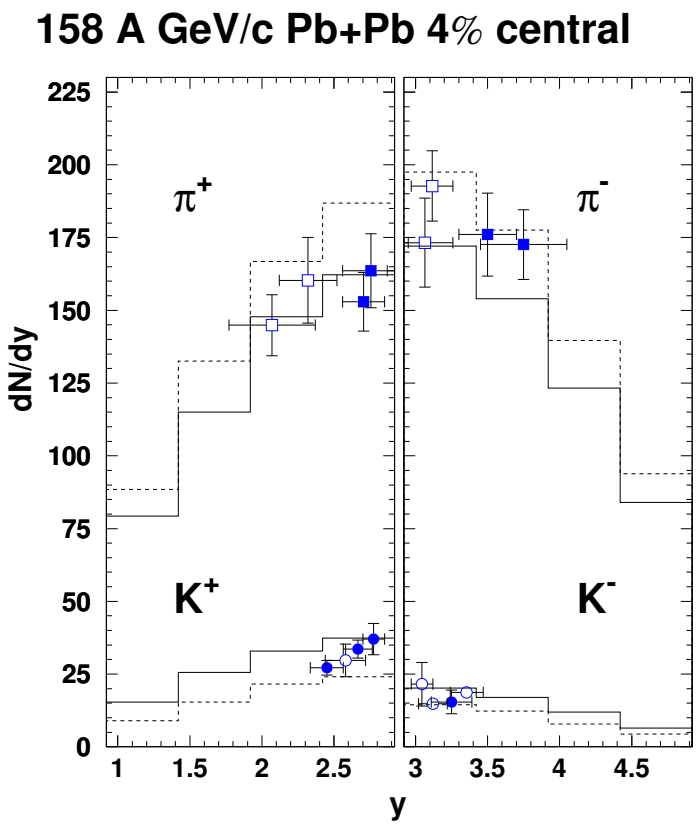

Figure 4.2: Comparison of measured charged kaon and pion yields with RQMD predictions. The vertical error bars indicate statistical and systematic errors, added in quadrature; the horizontal ones – y boundaries of the acceptance used for p_T integration in each spectrometer setting. Open symbols represent spectrometer settings whose y position is shown mirror-reflected around midrapidity (2.92); their solid analogs – the actual settings. RQMD: solid line – standard mode, dashed line – no rescattering.

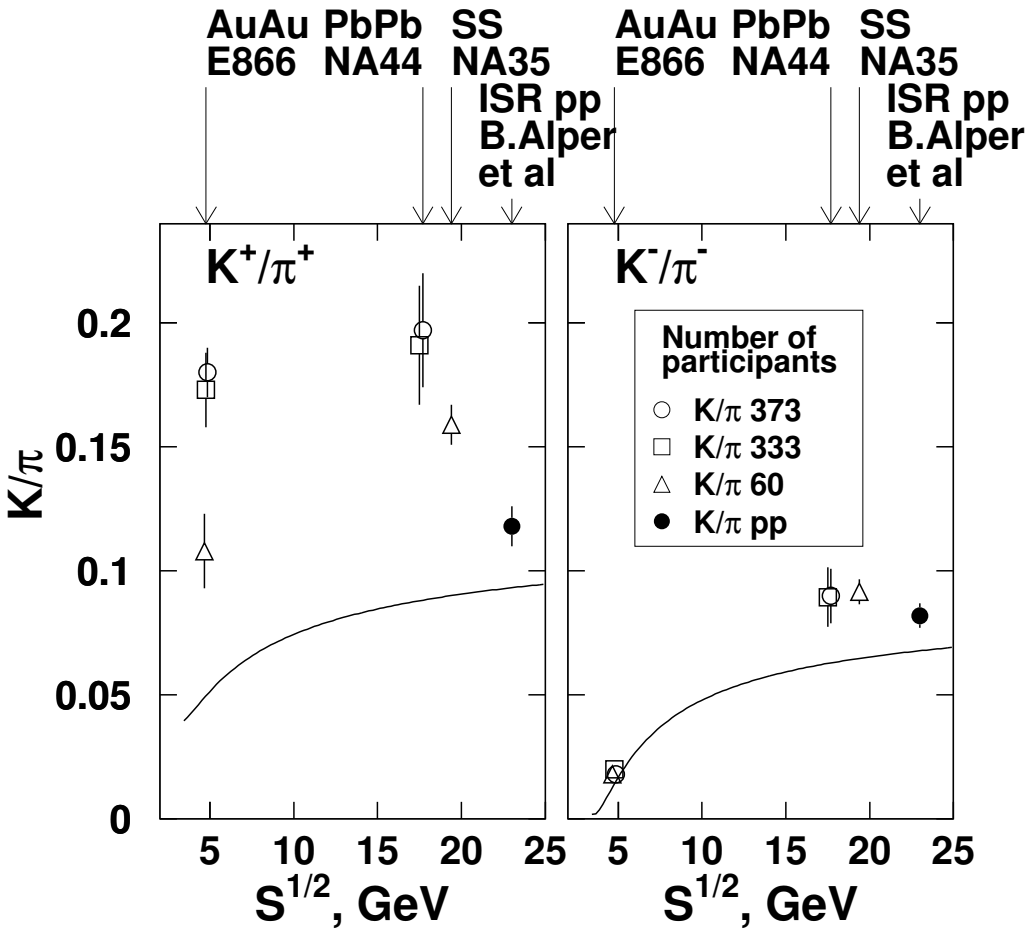

Figure 4.3: K/π ratios in symmetric systems at midrapidity $|y - y_{CM}| \leq |y_{proj} - y_{targ}|/8$. The solid line shows full solid angle K/π in $p+p$ collisions from the interpolation [59]. The data points from other experiments result from an interpolation in y to the midrapidity interval. The E866 data points [60] are also interpolated in the number of participants, for comparison with the SPS data.

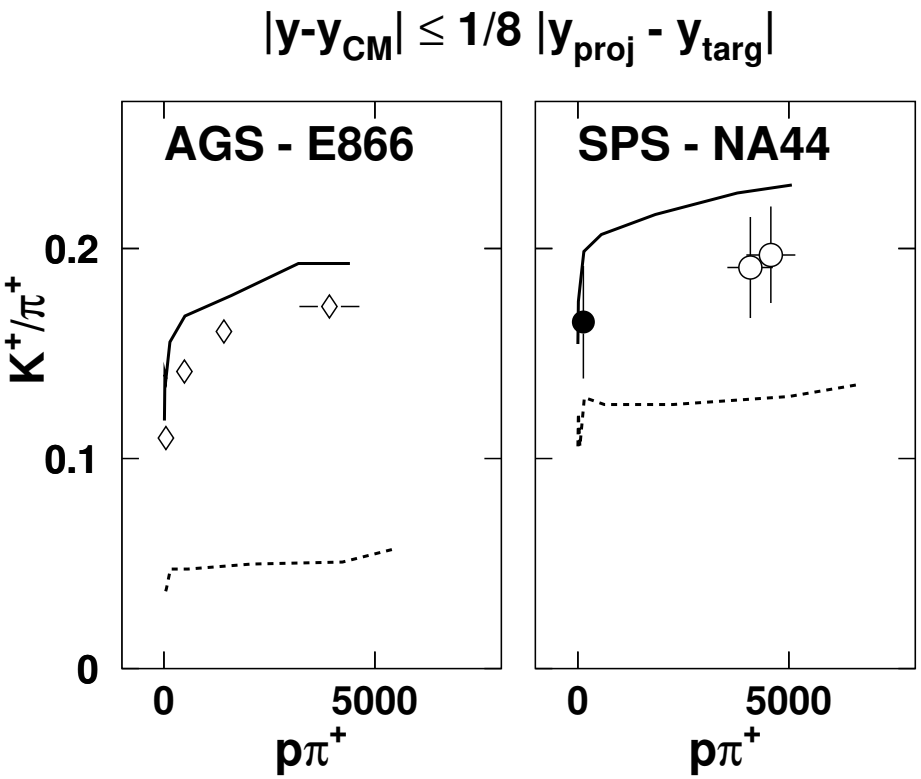

Figure 4.4: Comparison of measurements with RQMD predictions: K^+/π^+ ratio in the specified rapidity interval around mid-rapidity, as a function of the product of pion and proton dN/dy, obtained in the same rapidity interval, in symmetric collisions. ◇ – E866 AuAu, ● – NA44 SS, ○ – NA44 PbPb. RQMD: solid line – standard mode, dashed line – no rescattering.

of the strangeness-enhancing rescattering. The rate of change in the K^+/π^+ ratio with this rescattering observable is initially very high. However, K^+/π^+ nearly saturates after this initial rise. The figure shows why the enhancement is large as soon as the multiplicity becomes appreciable. The values of "$p \times \pi$" reached at the SPS and AGS are comparable, explaining the similarity of the kaon enhancement despite the different energies. RQMD reproduces the trend of the data very well, and the dotted lines (illustrating no rescattering) along with the shape of the rise with "$p \times \pi$" underscore the role of hadronic rescattering in kaon yields. The quantitative agreement of RQMD with the data is not as good, but the final results are undoubtedly quite sensitive to the magnitude of the cross sections used in the model.

When comparing AA data to pp, even if only particle ratios are considered, it is important to bear in mind that there are effects which distinguish AA from pp and which do not qualify as QGP signals. The time interval between two NN interaction in the target rest frame is of the order of fm/c, but due to the Lorentz time dilation, the intermediate object created in an NN interaction has no time to hadronize and is involved in the next collision and all further ones. RQMD[57] and VENUS[64] take this into account. Comparison to pA, rather than pp, is more credible, but if the intermediate partonic objects can involve constituents from more than one projectile nucleon, a similar argument still holds. And according to the Lorentz invariance, the intermediate partonic objects can involve more than one *projectile* nucleon since, as we have seen, they can involve more than one *target* nucleon, whereas such kind of discussion should not depend on the choice of reference frame. We therefore conclude that, qualitatively speaking, a comparison with a lighter system can not be done in a completely model-independent way, even though, quantitatively speaking, there are different degrees of credibility among the existing methods. In making the claim about the enhancement of (multi)strange (anti)baryons, WA85 compared SW with pW[65], NA49 – $PbPb$ with pp[66], WA97 – $PbPb$ with pPb system[67], but notably, the latter experiment devoted a special paper to the RQMD and VENUS comparisons[69].

Some strangeness production in RQMD goes through the excitation of the nucleon resonances – these are not considered secondaries, they are propagated and can be re-excited and de-excited[68]. Some of their decay channels contain strange mesons and baryons. For this reason, there is a difference between K^+/π^+ ratio in pp and K^+/π^+ ratio in RQMD without rescattering (as seen from comparison between Fig.4.3 and Fig.4.4). This difference looks larger for SPS than for AGS.

There are two processes in the RQMD mode *without rescattering* that affect the K/π ratio differently [68]:

1. slowing down of the original nucleon as it passes through the medium. This works to reduce K/π ratio, compared with pp collisions at the original $\sqrt{s}$.

2. excitation of resonance nucleon states some of which decay into $\Lambda + K$ – this enhances K/π.

Because at the AGS energy the slowing down is significant, these two processes tend to balance each other. At SPS, slowing down is not so significant, and the resonances win.

WA97 Collaboration measured yields of K^0_S, Λ, Ξ, and Ω (both particles and antiparticles) at midrapidity for $p + Pb$ and $Pb + Pb$ collisions [67]. It was found that the enhancement factor with respect to $p+Pb$ is larger for $\bar{s}\bar{s}\bar{q}$ and ssq than for $\bar{s}\bar{q}\bar{q}$ and sqq baryons. However, the measured enhancement for *anti*baryons is *smaller* than for baryons.

RQMD predictions for strange and antistrange baryon yields in $Pb + Pb$ are available [57] to compare with. The microscopic cascade method of RQMD does not involve the notion of the deconfined quark-gluon soup, even though the partonic degrees of freedom are involved via color strings and ropes. Elastic and inelastic rescattering is simulated. The publication [57], based on RQMD 2.1, contains predictions for all the hyperons measured in [67], except for Ω and $\bar{\Omega}$, as dN/dy histograms and total number yield per central event. With reasonable accuracy, one can draw meaningful conclusions from comparing WA97's $\Delta N/\Delta y$ within $\Delta y = 1$ around midrapidity [4] in the most central sample with RQMD's dN/dy. It turns out that RQMD [57] overpredicts K^0_S, overpredicts Λ, does a good job on $\bar{\Lambda}$, and considerably overpredicts Ξ^- and $\bar{\Xi}^+$ yields reported for $Pb + Pb$ by the WA97 [67]. The same work includes predictions for RQMD runs with ropes, but without rescattering, and with no ropes and no rescattering. Whereas ropes are the main effect responsible for the birth of strange (anti)hyperons, rescattering depletes their abundance by redistributing (anti)strange quarks into mesons. The latter is a generic hadrochemistry feature not unique to RQMD, as has been discussed earlier.

The WA97 Collaboration made a dedicated comparison of their data with VENUS and RQMD 2.3[69], and concluded that VENUS[64] (based on Gribov-Regge theory with rescattering simulation via pre-hadron clusters) *overpredicts* yields of $\bar{\Lambda}$, Ξ^-, $\bar{\Xi}^+$, Ω^- and $\bar{\Omega}^+$ in pPb and $PbPb$, whereas RQMD 2.3 does a good job for K^0_S, Λ,$\bar{\Lambda}$, Ξ^- and $\bar{\Xi}^+$, but underpredicts Ω^- and $\bar{\Omega}^+$.

[4] from -0.5 to 0.5 in the CMS

4.5 Conclusion from NA44 strangeness measurements

Production of charged K and π mesons in central Pb+Pb collisions at 158 GeV/nucleon has been measured. Within the centrality range studied, no strong multiplicity dependence of the kaon m_T slopes or K/π ratios has been observed. We see no significant slope difference between K^+ and K^-. K^+/π^+ is enhanced by a factor of about two over $p+p$ collisions, whereas K^-/π^- is little enhanced. Our measurement of K^+/K^- in this saturated region may be used for chemical calculations of the hadron gas.

Comparison with the RQMD model shows that the model qualitatively reproduces the hadron chemistry, through the rescattering of the produced particles. Quantitative comparisons, however, show that the model overpredicts the K^-, while the magnitude of K^+ enhancement is within the range explainable by the RQMD mechanisms. Deconfinement scenarios of the K^+/π^+ enhancement can not, however, be ruled out or proven by the NA44 data alone. Non-NA44 measurements of strange particles less common than kaons do not clarify the picture and the overall impression is that

- an overprediction of a (multi)strange (anti)baryon yield is the most frequent outcome for both VENUS and RQMD
- the rarer the particle, the less reliable the theoretical predictions, based on dynamical modes, become.

Chapter 5

Technique for event-by-event multiparticle texture analysis using the NA44 Si pad array

This chapter describes analysis procedures performed to obtain physically meaningful results from the Si pad array (hereafter referred to as *the detector*) measurements. Motivations for such measurements are outlined in the Introduction. A description of the detector's design and principle of operation, as well as of the experimental setting, is given in Chapter 2. The analysis required solutions to the following problems:

- channel-by-channel amplitude calibration (Section 5.3),
- determination of the detector's geometrical position with respect to the beam's center of gravity (Section 5.4),
- study of cross-talk between the channels (Section 5.5),
- construction of an observable sensitive to the possible manifestations of the physics we are interested in (Section 5.6),
- analysis of background effects and a technique of their subtraction (Section 5.7),
- a Monte-Carlo simulation of the detector's response to model-generated events based on the detailed understanding of the above-mentioned detector effects (Section 5.8),
- analysis of the observable's response/sensitivity to the interesting effects, based on the MC simulation (Sections 6.2 and 6.3).

Run number	sign	target	trigger	events on tape	events after cuts
3155	−	Pb	VB	42650	42408
3191	−	Pb	VB	39312	38905
3192	−	Pb	$VB.T0$	39924	36334
3156	−	empty	VB	35280	35020
3190	−	empty	$VB.MUL1$	7979	4831
3200	−	empty	$VB.MUL1.\bar{C}1.\bar{C}2$	2027	1412
3157	+	empty	VB	40275	40078
3187	+	empty	$VB.\bar{C}1.\bar{C}2$	6454	4141
3188	+	empty	VB	38208	37901

Table 5.1: Data used in the Si analysis.

5.1 Data sample and data reduction

The physics data set consists of runs 3155, 3191, 3192. Runs 3155 and 3191 are valid beam triggered runs; 3192 is a central trigger run. Runs 3156, 3190 and 3200 are empty target runs of the same field polarity as the physics runs; runs 3157, 3187 and 3188 are empty target runs of the opposite field polarity. The magnetic spectrometer setting for all runs is 4 GeV/c. A cut on CX veto counter (Section 2.4.1) was used to safeguard against non-target interactions and beam halo. Contamination of the detector by δ-electrons is a major problem discussed in subsection 5.2. Due to the presence of the dipole magnetic field, only one half of the detector is δ-contaminated. The problem therefore is solved by ignoring that half in the analysis altogether. In the negative runs, the left (looking along the beam) side of the detector is δ-free. Only that side was used for the analysis. Out of its 256 channels, 252 were operating normally and 4 were dead. Whenever an *amplitude sum* is quoted, it is from those 252 channels only. The range of calibrated amplitude sum between -25 MeV and 95 MeV was split into 12 bins of equal (10MeV) width; events outside this range were not used. The power spectra of local fluctuations were analyzed in each bin. Event mixing was done separately in each bin. More detailed information about the data sample is given in Table 5.1.

5.2 δ-electrons and the Si detector

One of the first problems encountered is that of the δ-electron contamination of the detector. The δ-electrons are copiously produced by the Pb beam nuclei passing through the Pb target. The thickness of the target is $1.15\ g/cm^2$, or 18% of the radiation length. Due to the z^2 dependence of the ionization energy loss on the charge of the projectile, a passage of a beam nucleus without nuclear interaction (statistically, the predominant event) produces, typically, more δ-electrons than originate from (even a central) interaction. Kinematically, the problem is that of an elastic scattering of a relativistic heavy incident nucleus on an (effectively resting) atomic electron – a particular case of a relativistic elastic two-body scattering (analyzed in [75] and other textbooks). For an electron initially at rest in the lab, the dependence of its final state energy on the emittance angle θ is unique, and there is no kinemitical restriction on the angle. The differential cross-section

$$\frac{d\sigma}{d\theta} \propto \frac{\sin\theta}{\sqrt{1-\sin^2\theta}} \tag{5.1}$$

grows with the polar angle for the angles of interest ($\theta < \pi/2$). This results in a peculiar pattern of detector occupancy, with maximum occupancy at the outer rings of the detector – opposite to the trend seen in the nuclear interactions. In valid beam triggered runs (I looked at both field polarities, to disentangle effects of δ-electrons from those of the geometrical misalignment) it was noticed that in the outer rings, the extra multiplicity on the outer rings, ascribed to the δ-electrons, is comparable with the contribution of the nuclear interaction vertex. In the T0-amplitude triggered [1] runs without magnetic field, δ-electrons dominate the picture. In this situation, we decided to

- use runs with field on
- ignore the contaminated half of the detector in the physics analysis

In the 4 GeV/c setting, the magnetic field strength in the first dipole (which includes the target area) is $\approx 0.8Tl$. The kinetic energy spectrum of δ- electrons falls off like

$$\frac{dN}{d(T/m_e)} \propto \left(T/m_e\right)^{-2} \tag{5.2}$$

[1] we normally call it "central trigger", but in the field-off situation this name is hardly justifiable, as seen from the context

Simple estimates, based on the kinetic energy spectrum (as well as GEANT simulations) lead to the conclusion that for all practical purposes the residual contribution of δ-electrons to the multiplicity on the δ-clean side is negligible for the field and geometry in question.

5.3 Amplitude calibration of the Si channels

Amplitude calibration was carried out channel by channel for all 512 channels. The following elements are essential to understand the procedure.

1. Using a given run (4×10^4 events), we accumulate a histogram of amplitudes for a given channel. A typical distribution is shown on Fig. 5.1

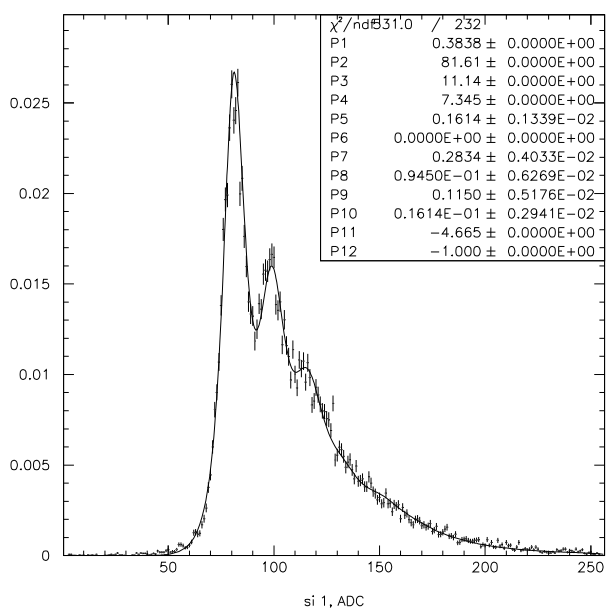

Figure 5.1: A typical calibration fit. Channel 1.

2. Normalize the amplitude distribution to unit total integral. The same normalization is imposed on the fitting model in the calculations. This removes one fit parameter, but requires extra work in figuring out and imposing the normalization of the fitting function.

3. Empty pad peak. The fitting function was developed by using data from a valid beam trigger run (low multiplicity).

Its distribution represents noise inherent in all signal measurements. Therefore, in the fitting model, this noise distribution is folded with physical fluctuation of the ionization energy loss. The shape of the peak is non-Gaussian; it has somewhat more events on the tails. Therefore, I describe this peak by a product of a Lorentzian (a function with pronounced tails), and a Gaussian which prevents those tails from going too far. The noticeable asymmetry of the peak is taken into account in two ways: by introducing an addition of an odd-power Hermite polynomial (with p_{11}) and by displacing the symmetry axis of the Lorentzian with respect to that of the Gaussian (through p_{12}).

$$\mathcal{N}(x) = \frac{1}{n}\frac{\exp(-\frac{1}{2}(\frac{x}{p_3})^2)(1+\frac{1}{6}(\frac{p_{11}}{p_3})^3(8(\frac{x}{p_3})^3 - 12\frac{x}{p_3})}{(x-p_{12})^2 + p_4^2}. \tag{5.3}$$

The normalization constant n has to be calculated numerically. $x_0 = x - p_2$, where x is the ADC channel number and p_2 is the position of the empty pad peak.

4. Ionisation energy loss is a random process and large fluctuations can occur in the energy dE deposited by a particle in a layer of material. The thinner the layer, the more pronounced is the tail of the statistical distribution of dE. This is characterized by the parameter

$$\kappa = \frac{\xi}{E_{max}}, \tag{5.4}$$

where ξ is the mean energy loss of a particle with charge 1, moving with velocity β, and undergoing Rutherford scattering on an atom with atomic mass A, and Z electrons, in a medium of such atoms of thickness $t(g/cm^2)$:

$$\xi = \frac{153.4Zt}{A\beta^2} keV. \tag{5.5}$$

E_{max} is the kinematical upper limit on the energy transfer in a single collision:

$$E_{max} = \frac{2m_e\beta^2\gamma^2}{1 + 2\gamma m_e/M + (m_e/M)^2}, \tag{5.6}$$

where M is the mass of the incident particle.

In high energy physics, it is customary [78] to use Landau distribution [76] (which ignores the existence of E_{max}) for

$$\kappa < 0.01, \tag{5.7}$$

and use Vavilov distribution for $0.01 < \kappa < 10$. For our detector, ξ depends the location of the pad and velocity of the incident particle, but typically is in the range 110-120 keV. Given that the typical ionizing particle is a charged pion ($m_e/M \approx 3.7 \times 10^{-3}$) with the lab energy of the order of 2-4 GeV (at midrapidity), it is easy to see that the condition 5.7 is satisfied. Therefore we use the Landau distribution in calibration.

CERNLIB function DENLAN gives it as a function of a universal dimensionless variable λ. This variable is related to the actual energy loss, Δ, through the expression:

$$\lambda = \frac{\Delta}{\xi} - 1 + \Gamma - \ln(\frac{\xi}{\epsilon'}) \tag{5.8}$$

Here Γ is Euler's constant 0.577215... , and ξ is explained by Eq. 5.5.

and ϵ' is defined, according to Landau's work [76], as

$$\epsilon' = \exp(\beta^2)(1-\beta^2)\frac{I^2}{2m_e\beta^2}, \tag{5.9}$$

where I is ionization potential (of Si), taken to be 172.2 eV on the basis of [77].

I set up the calibration code so that the Si thickness is calculated taking into account the track's angle of incidence for given geometrical location of a pad. β is calculated for a "representative" particle with p_T=0.4 GeV/c and $y = 2.4$.

The energy loss in the formula is related to the ADC channel X through the conversion coefficient p_5, and the "0" position p_2.

$$\Delta = \frac{x - p_2}{p_5} \tag{5.10}$$

$dN/\,d\Delta = DENLAN(\lambda)/\xi$ is the probability density of having certain Δ, its integral = 1. According to the expression above, $d\Delta/\,dx = 1/p_5$, therefore the single particle ADC distribution

$$dN_1/\,dx = DENLAN(\lambda)/(\xi p_5),$$

and its integral still = 1. (Here, x is the ADC amplitude).

5. Now consider the Landau distribution for m hits. For given fixed number of hits m, I apply "linear superposition", that is, replace the problem of m incident particles with that of a single particle traversing a layer of material m times thicker. Therefore, ξ becomes ξm, and the rest remains unchanged:

$$\frac{dN_m}{dx} = \frac{dN_1(m\xi)}{dx} \tag{5.11}$$

6. Statistics of hits. In the overall fit function, weights must be assigned to the cases of various m. In general, a Poisson distribution does not result in good fits.[2] Therefore, I independently vary the weights of 1, 2, 3, and 4 hits. The rest of weights w_5, w_6, w_7 (I consider up to 7 hits, as the weights for larger numbers are vanishingly small) follow a Poissonian, with mean value inferred from ratios of weights formed among w_1, w_2, w_3, w_4.

   Here is how the weights are related to the fit parameters

$$w_1 = p_7 \tag{5.12}$$

$$w_2 = w_1 - p_8 = p_7 - p_8 \tag{5.13}$$

$$w_3 = w_2 - p_9 = p_7 - p_8 - p_9 \tag{5.14}$$

$$w_4 = w_3 - p_{10} = p_7 - p_8 - p_9 - p_{10} \tag{5.15}$$

$$w_0 = 1 - w_1 - w_2 - w_3 - ... - w_7 \tag{5.16}$$

[2]This is not surprising for at least two reasons: 1) a sample of events in a run is *not* a sample of a constant total multiplicity – the multiplicity varies event by event. Thus varies the mean multiplicity μ. A sum of multiple Poissonians of different μ and arbitrary weights is not expected to be a Poissonian. 2) When the total multiplicity is fixed, the dominant reason for the deviation will be correlations between particles (e.g. the Bose-Einstein ones). In our case, however, the dominant reason is (1).

7. Putting the pieces together. The probability distribution to see ADC amplitude x, for given hit multiplicity distribution w_m is

$$\frac{dN}{dx} = \sum_{m=1}^{7} w_m \frac{dN_m}{dx} \tag{5.17}$$

This distribution is then folded with noise $\mathcal{N}(x)$:

$$\int_{-\infty}^{+\infty} \frac{dN}{dx} \mathcal{N}(x - x')\, dx' \tag{5.18}$$

Then I add the result (smeared compared to the "clean" Landau) to the "0" peak $w_0 \mathcal{N}(x)$.

8. This description of the fitting model ends with a summary of fit parameters.

   - p_1 – the overall normalization, normally fixed at 1.
   - p_2 – position of the empty pad peak
   - p_3 – Gaussian sigma of the empty pad peak
   - p_4 – Lorentzian gamma of the empty pad peak
   - p_5 – ADC/keV conversion factor
   - p_6 – makes parameters p_3 and p_4 grow linearly with ADC, normally set to 0.
   - p_7 – w_1
   - p_8,p_9,p_{10} – used to define other weights
   - p_{11} – Hermite polynomial asymmetry parameter
   - p_{12} – Lorentzian asymmetry parameter

Calibrations from runs 3155 and 3192 were used for the rest of runs listed in Table 5.1.

5.4 Geometrical alignment of the detector

5.4.1 Formulation of the problem

An offset of the event vertex with respect to the detector's symmetry axis results in a non-trivial functional dependence between the actual η and

ζ [3], and the η', ζ' presumed based on the "ideal" geometry: $\eta = \eta(\eta', \zeta')$, $\zeta = \zeta(\eta', \zeta')$. This makes the observable multiplicity distribution $d^2N/\,d\eta'\,d\zeta'$ (in the presumed coordinates) differ from a simple function of η':

$$\frac{d^2N}{d\eta'\,d\zeta'} \neq \frac{1}{2\pi}\frac{dN}{d\eta'} \tag{5.19}$$

In the true coordinates η and ζ, the inequality 5.19 becomes an equality. However, the detector's acceptance area in the true coordinates becomes distorted. Figures 5.2 and 5.3 show the pad multiplicity (gray level) in the misaligned and aligned coordinates, respectively.

In the following we will refer to this as a "Jacobian effect". The Jacobian effect, obviously, contributes to the event textures, especially on the large scale, and needs to be evaluated and corrected for.

5.4.2 Solution

From Eq.5.19, the criterion of the true coordinate basis (η, ζ) emerges naturally: it is the basis which makes the observable $d^2N/\,d\eta\,d\zeta$ independent of ζ. Such a criterion can be formulated quantitatively; then, the problem becomes that of a formal minimization, treatable numerically. This is done in the following way. Let i and j index pads. We approximate acceptance of a pad i by a quadrangle and calculate its area on the η, ζ plane S_i. Then $d^2N/\,d\eta\,d\zeta$ at the pad i is approximated as N_i/S_i, where N_i is the pad's mean occupancy. We denote its statistical errorbar (based on the propagation of the fitting error estimates obtained in the fitting procedure described in 5.3) as $\sigma(N_i/S_i)$. We seek an offset such that N_i/S_i and N_j/S_j with i and j at different ζ, but similar η, be minimally different. In practice, comparison of the N/S quantities must be limited to pads with a finite η difference, which is small enough so that the only reason for the difference of the N/S may be the geometrical offset. Then, the quantity to minimize is

$$\frac{\sum_{i,j} \text{ with small } \Delta_{i,j} \; \frac{(N_i/S_i - N_j/S_j)^2}{\sigma(N_i/S_i)^2 + \sigma(N_j/S_j)^2}}{\sum_{i,j} \text{ with small } \Delta_{i,j} \; 1} \tag{5.20}$$

where

$$\Delta_{i,j} = \eta_i - \eta_j \tag{5.21}$$

[3] In this Chapter, I denote azimuthal angle by ζ to reserve ϕ and ψ for the wavelet functions

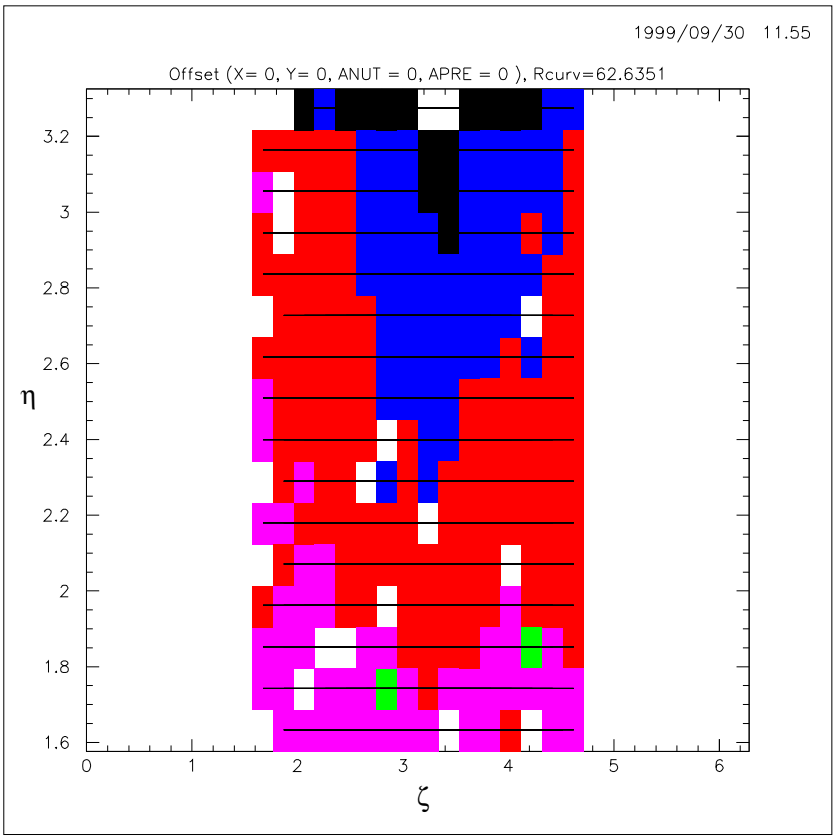

Figure 5.2: Example of a monitoring plot used in the course of the analysis to understand the alignment procedure and the alignment quality. The color (or gray level) corresponds to the pad multiplicity. No misalignment correction is applied. The horizontal lines connect centers of the pads with $\Delta_{i,j}$ sufficiently small for the pairs to be used in formula 5.20 (compare with Fig. 5.3). Run 3192. The δ-contaminated part of the detector is not shown.

is the maximal separation in η allowed. Too small a value of $\Delta_{i,j}$ will result in too few channel pairs to compare. To calculate the function, a geometry transformation is required to find displaced coordinates (η', ζ') for every $(\Delta x, \Delta y)$ displacement of the detector in the vertical plane. Displacement along the z axis and rotations were not considered because the problem does not seem sensitive to them. GEANT simulation package [78] was used to calculate the geometrical transformations, and MINUIT minimization package [79] – to search for the minimum of the function given by formula 5.20. At first, I

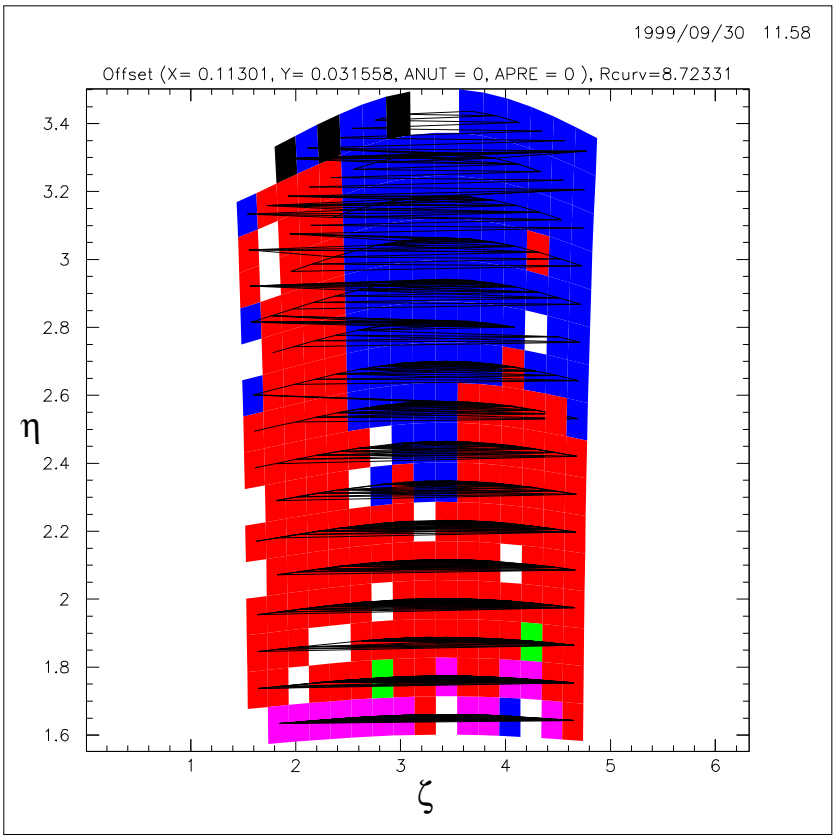

Figure 5.3: Another example of a monitoring plot used in the course of the analysis to understand the alignment procedure and the alignment quality. The color (or gray level) corresponds to the pad occupancy. A misalignment correction is applied. One can see how both the acceptances of the pads and their (double differential !) multiplicities are modified. The horizontal lines connect centers of the pads with $\Delta_{i,j}$ sufficiently small for the pairs to be used in formula 5.20 (compare with Fig. 5.2). Run 3192. The δ-contaminated part of the detector is not shown.

was using $\Delta_{i,j} = 0.0225$, [4] with a non-gradient (SIMPLEX [79]) minimization. Then I realized that the function 5.20, not everywhere differentiable, could be made suitable for gradient minimization by smoothing it. The smoothing was done by replacing the sharp cutoff at $\Delta_{i,j}$ by a smoothly decaying weight

[4]This value is $((\eta_{max} - \eta_{min})/16/5$, i.e. 1/5 of the pad's rapidity span.

function:

$$w(i,j) = \frac{1}{1+\exp(2\frac{\Delta_{i,j}-\Delta_{cut}}{\Delta_{cut}})}, \tag{5.22}$$

where Δ_{cut} was set at 0.01125. [5] That is, the binary "yes/no" decision making on the inclusion of a term was replaced by a weight, varying smoothly between 0 and 1.

```
START MNCONTOUR CALCULATION OF  12 POINTS ON CONTOUR.
Y-AXIS: PARAMETER   2  Y shift
 0.4200000E-01 ..............................................
                .                 .          X            .
 0.4000000E-01 ...                .   X              X     .
                .                 .                        .
 0.3800000E-01 ...            X   .                        .
                .                 .                        .
 0.3600000E-01 ...                .                        .
                .    X            .                      X.
 0.3400000E-01 ...                .                        .
                .                 .                        .
 0.3200000E-01 ...  X             .                        .
                ................. ........................
 0.3000000E-01 ...                .                        .
                .                 .                  X     .
 0.2800000E-01 ...X               .                        .
                .                 .                        .
 0.2600000E-01 ...                .           X            .
                .                 .                        .
 0.2400000E-01 ...       X        .                        .
                .              X .                        .
 0.2200000E-01 ..............................................
                /        /        /        /        /
          0.9200E-010.1020    0.1120    0.1220    0.1320
                      ONE COLUMN=0.1000000E-02
                      X-AXIS: PARAMETER   1  X shift
```

Figure 5.4: Alignment results for run 3192. The axes show detector's offsets in X and Y in cm. MIGRAD (see [79]) minimization converged at point $(X,Y) = (0.110 \pm 0.019, 0.031 \pm 0.009)$ cm. The dotted lines cross at the estimated minimum. The contour and the errorbar estimates quoted correspond to the unit deviation of the function from the minimum.

A typical result of the minimization is shown on Figure 5.4. The offsets we find are within the tolerance of the detector/beam positions. The (η, ζ) transformation so found was used in the Monte Carlo detector response simulation to compare the measured data with the event generators.

[5] This value is 1/10 of the pad's rapidity span.

5.5 Cross-talk analysis

Cross-talk between the electronics channels is a detector-related correlation phenomenon and introduces a "texture" effect of its own. Therefore it received a lot of attention during the analysis. An event mixing technique (subsection 5.6.2) which respects cross-talk was eventually preferred.

5.5.1 Sources of cross-talk

Two sources of cross-talk are expected:

1. global cross-talk[6] in the AMPLEX chips is known [30] to be negative [7] and proportional to the total charge received by the chip.

2. negative cross-talk due to capacitive coupling between pads through the detector board.

The AMPLEX group performed test measurements [30] where detector board cross-talk was eliminated by disconnecting two pairs of channels adjacent to the stimulated one on each side of it, but in the actual experimental application this source of cross-talk should be expected. Its magnitude was not a priori clear. In the AMPLEX test measurements [30], -1.5% global cross-talk in the chip was observed. The experts admit [30]: "The origin of this effect is not yet understood". They found the adjacent cross-talk to be negligible. Our channel-to-channel correlation analysis of the NA44 central *PbPb* data, discussed in detail in this section, reveals 9% adjacent cross-talk. The global cross-talk was seen with event displays, although rarely, and did not manifest itself in the channel-to-channel correlation analysis.

5.5.2 Channel wiring and numbering

General description of the Si detector is given in subsection 2.6. For the cross-talk discussion, it is important to remember the channel numbering scheme of the detector: channel "1" is in the outer ring, then the numbering proceeds sector by sector, so that you can trace it with a continuous curve, going azimuthally counter-clockwise, looking along the beam direction. Every sector (16 channels) is read out by the same AMPLEX chip, one sector per chip.

---

[6] that is, the cross-talk between the given stimulated channel and *all other* channels of the chip

[7] that is, the induction has the opposite sign with respect to the stimulating signal

5.5.3 The covariance matrix approach

In our detector with 512 channels, there are $512\times(512-1)/2 = 130816$ two channel pairs (unordered), all of which were subjected to covariance analysis off-line. A cross-talk, present between channels i and j, and absent in some other pairs, makes the (i, j) pair special in some respect. The quantitative way to look at the problem, *at first glance*, appears to be the following. On a sufficiently large set of events (statistics of a single run, $\approx 4 \times 10^4$ events is sufficient) calculate the covariance matrix of all channels:

$$\mathrm{cov}(A_i, A_j) = \mathfrak{M}[(A_i - \mathfrak{M}[A_i])(A_j - \mathfrak{M}[A_j])] = \mathfrak{M}[A_i A_j] - \mathfrak{M}[A_i]\mathfrak{M}[A_j], \tag{5.23}$$

where the $\mathfrak{M}[\ ]$ is a mathematical expectation operator. Its estimate is an average taken on a set of events. When this is done, the pattern turns out to be dominated by the trivial ring-wise correlation (with the covariance matrix having characteristic chess-board structure, if the i and j indices are assigned according to the channel numbering described in subsection 5.5.2 above. In other words, one sees that a correlation between channels i and j is the tighter, the closer their ring indices. This turns out to be a manifestation of a recurrent theme [8] in the study of correlations – a problem of the varying mean density which feigns a correlation, when one looks at a two-point correlator like the one of Eq. 5.23. What happens is a departure of $\mathrm{cov}(A_i, A_j)$ from 0 simply because an event of a larger/smaller multiplicity tends to increase/decrease A_i as well as A_j in a correlated way. This correlation is genuine but trivial. To go beyond it, one needs to identify/estimate and subtract the varying part of A in some way. The way we do it is by taking, for a given event, a half-ring average amplitude and subtracting it from A:

$$a_i = A_i - \frac{\sum_{\text{half-ring of } i} A_k}{\sum_{\text{half-ring of } i} 1} = A_i - \frac{1}{16} \sum_{\text{half-ring of } i} A_k \tag{5.24}$$

then substituting the a_i, rather than A_i, into Eq. 5.23. We take the half-ring where the channel belongs, either right or left, depending on the field polarity, rather than a full ring, because the calibrated amplitudes of the two halves of the detector are quite different due to the additional ionization from δ-electrons on one side. One peculiar side effect, introduced by the subtraction, is an auto-anticorrelation in the covariance matrix. Namely, the channels of

[8] In the Discrete Wavelet Transformation approach, a very similar problem – that of the varying mean density $\bar{\rho}$ – is solved by virtue of the orthogonality of the basis, as will be explained in section 5.6.

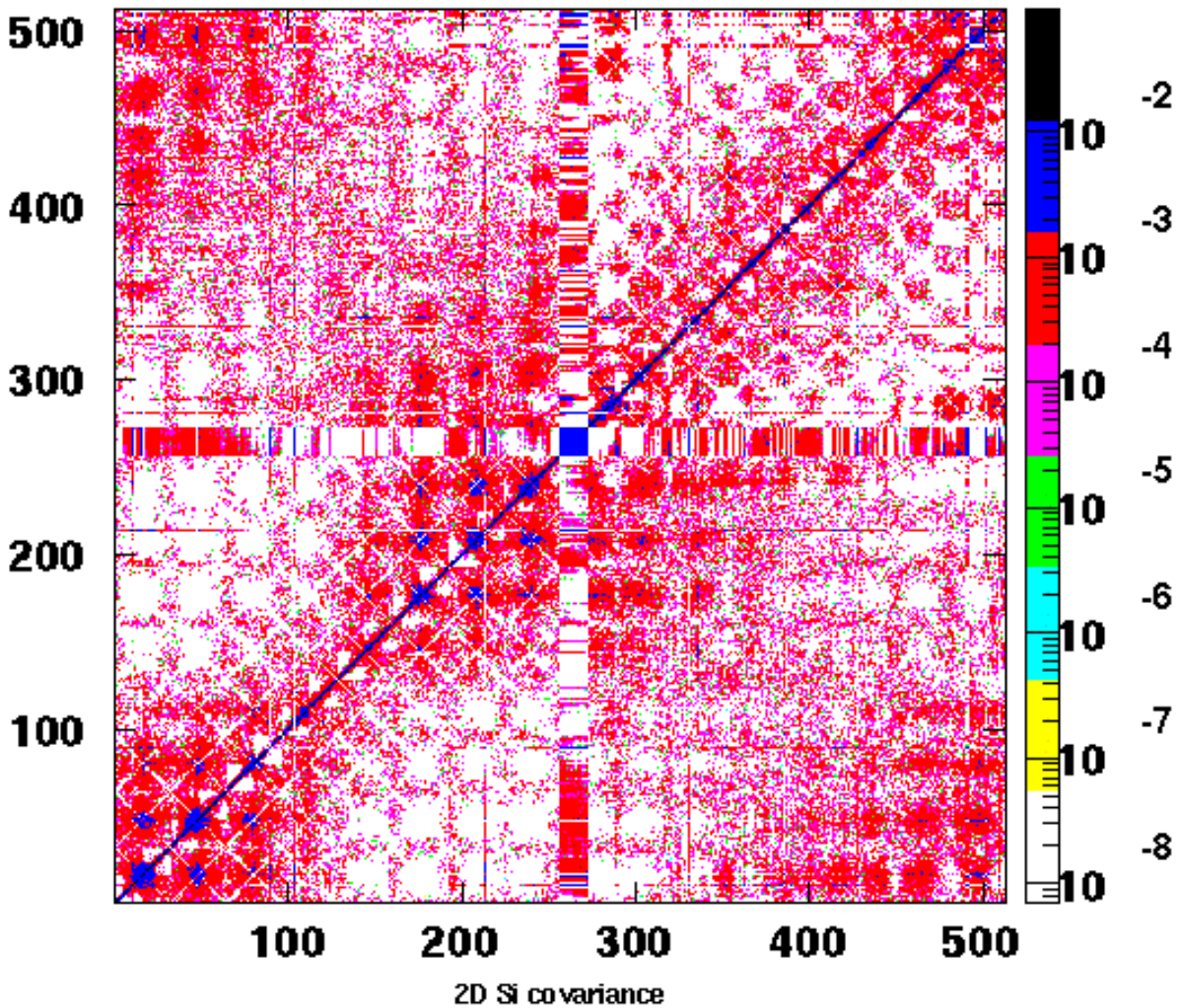

Figure 5.5: Covariance matrix cov(a_i,a_j) of the Si pad array in run 3192. The color scale is logarithmic, units are MeV^2. The matrix is symmetric. Increased elements next to the main diagonal indicate the adjacent neighbour cross-talk. Non-uniform overall landscape is due to the beam offset and the beam's geometrical profile. The white diagonals represent the autocorrelation discussed in subsection 5.5.3. The "cross" in the middle corresponds to dead channels.

the same half-ring (e.g., 1 and 32, 2 and 31, see subsection 5.5.2 for the channel numbering) appear anticorrelated. This is seen on Fig. 5.5 as white diagonal lines. The mechanism is simply the fact that when i and j belong to the same half-ring,

$$a_i = A_i - \frac{1}{16}(A_i + A_j + S_{14}), \tag{5.25}$$

where S_{14} is an amplitude sum over 14 other channels of the same half-ring, and

$$a_j = A_j - \frac{1}{16}(A_j + A_i + S_{14}), \tag{5.26}$$

then a_i and a_j are anti-correlated no matter what the physical origins of A_i and A_j are. Elimination of this anticorrelation requires subtracting a different term (with A_i and A_j excluded) for every same half-ring pair (i, j), which would complicate the computations enormously. How large is the anticorrelation so induced ? Based on the Eq. 5.25 and 5.26, and using identities C.4 and C.5:

$$\begin{aligned}\mathrm{cov}(a_i, a_j) = \frac{15^2+1}{16^2}\mathrm{cov}(A_i, A_j) - \frac{15}{16^2}(\mathfrak{D}[A_i] + \mathfrak{D}[A_j]) \\ -\frac{14}{16^2}(\mathrm{cov}(A_i, S_{14}) + \mathrm{cov}(A_j, S_{14})) + \frac{1}{16^2}\mathfrak{D}[S_{14}],\end{aligned} \tag{5.27}$$

where $\mathfrak{D}$ denotes variance. If the leading cause of non-zero $\mathrm{cov}(A_i, A_j)$ is the common event multiplicity (which assumption practically amounts to neglecting the identity of the indices i and j as long as $i \neq j$ [9]), then a crude estimation can be done using

$$\mathrm{cov}(A_i, S_{14}) \approx \mathrm{cov}(A_j, S_{14}) \approx 14\mathrm{cov}(A_i, A_j), \tag{5.28}$$

$$\mathfrak{D}[S_{14}] \approx 14\mathfrak{D}[A_i] + 14 \times 13\mathrm{cov}(A_i, A_j), \tag{5.29}$$

and Eq. 5.27 can be rewritten entirely in terms of a single channel variance $\mathfrak{D}[A]$ and a two channel covariance $\mathrm{cov}(A_i, A_j)$:

$$\mathrm{cov}(a_i, a_j) = \frac{1}{16}(\mathrm{cov}(A_i, A_j) - \mathfrak{D}[A]) \approx -\frac{1}{16}\mathfrak{D}[A], \tag{5.30}$$

where the last approximation is based on the practical (and expected) observation that $|\mathrm{cov}(A_i, A_j)| \ll \mathfrak{D}[A]$. The $\mathfrak{D}[A]$ can be estimated based on an RMS^2 of a histogram like the one shown on Fig. 5.1 (but including all channels) and is approximately $(2.4 \times 10\mathrm{keV})^2 = 0.057 MeV^2$. In other words, we expect to see a number of negative covariance elements around $-0.0036\mathrm{MeV}^2$ as one of the features of the matrix.

[9] remember that i and j belong to the same half-ring and are therefore close in η

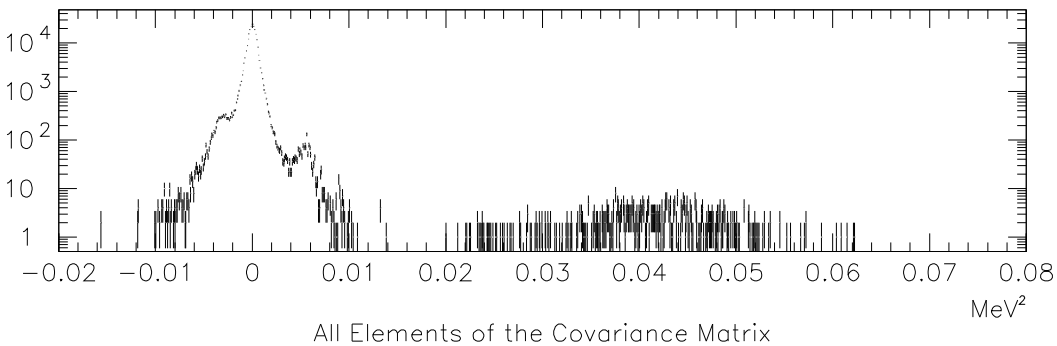

Figure 5.6: A distribution of the covariance matrix elements. Run 3192. Information on the cross-talk magnitude is in the distance between the third and fourth peaks (counting from left).

5.5.4 Cross-talk evaluation: results and discussion

Now it's time to introduce the measured cross-talk results and discuss their meaning. Figure 5.6 presents the distribution of the covariance matrix elements in magnitude.

Four peaks are clearly seen:

- The largest peak is centered at 0. No cross-talk is therefore the most likely outcome for an arbitrary pair of channels.
- A broad peak is centered between 0.04 and 0.05 MeV^2. It contains the diagonal elements of the covariance matrix and does not represent a channel-to-channel influence, but rather a single channel variance, or RMS^2 of a distribution like that of Fig. 5.1.
- The peak on the left shoulder of the 0 peak is the one just discussed at length in subsection 5.5.3. It is indeed found where we expect it to be.
- Finally, the peak on the right shoulder of the 0 peak has to be identified with cross-talk. Fig. 5.7 shows this peak separately – it turns out to be the subset of the covariance matrix (i.e. the subset of histogram 5.6) which represents correlations between adjacent channels – namely, the elements next to the main diagonal. As we see, the cross-talk appears as a positive correlation between channels.

What is the magnitude of the cross-talk ? In a typical cross-talk measurement, i.e. by stimulating one channel and registering inductions on the others, at what percentage of the stimulating signal would the induction be ?

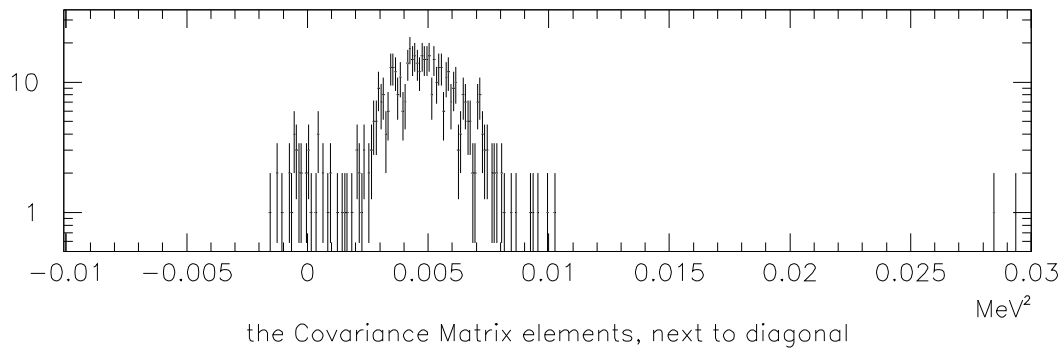

Figure 5.7: A distribution of the covariance matrix elements, that represent correlations between adjacent channels. Run 3192. Same binning as on Fig. 5.6; on that figure, this is seen as the third peak.

To answer this, let's modify equations 5.25 and 5.26 to model the coupling of the two channels with strength c:

$$\begin{aligned} A_i &\to A_i + cA_j, \\ A_j &\to A_j + cA_i \end{aligned} \tag{5.31}$$

and plug in the A_i and A_j so modified in $cov(a_i, a_j)$. What we get (using C.5) is

$$\begin{aligned} \mathrm{cov}(a_i, a_j) = &\frac{15^2 + (15c-1)^2}{16^2} - \frac{15(1-15c)}{16^2}(\mathfrak{D}[A_i] + \mathfrak{D}[A_j]) \\ &-\frac{14+15c}{16^2}(\mathrm{cov}(A_i, S_{14}) + \mathrm{cov}(A_j, S_{14})) + \frac{1}{16^2}\mathfrak{D}[S_{14}], \end{aligned} \tag{5.32}$$

and we repeat the arguments that followed Eq. 5.27. Now we are able to relate c with the observables, because the present analog of Eq. 5.30 reads:

$$\mathrm{cov}(a_i, a_j) \approx \frac{14 + 30(15c-1)}{16^2}\mathfrak{D}[A]. \tag{5.33}$$

We consider a typical pair of adjacent channels i and j, look at Fig. 5.7 and conclude that $\mathrm{cov}(a_i, a_j) \approx 0.005 MeV^2$ would be a reasonable estimate; then we recall that $\mathfrak{D}[A] \approx 0.057 MeV^2$ (it already figured in the end of subsection 5.5.3). With this input, Eq. 5.33 yields 9% for the effective cross-talk fraction c. There are pairs of channels with the coupling parameter c both lower and higher than this.

Why does the cross-talk appear as a positive correlation ? Do not both sources of cross-talk (see subsection 5.5.1) produce an anticorrelation ?

The covariance matrix is an "integral" way of looking at the problem. Information so obtained is not sufficient to realistically simulate the effect in the MC detector response program. An event display study indicates that unusual events happen where large positive amplitudes [10] in a couple of neighboring channels are accompanied by noticeable negative amplitudes in the other channels of the same chip (sector), which appear correlated among themselves and anticorrelated with respect to the large amplitude ones. Such an example is shown on Fig. 5.8. Sector 11 is affected by cross-talk. There are $16 \times (16-1)/2 = 120$ pairs to be formed among 16 elements (counting only pairs of different elements); in this particular example (2 correlated "positive" neighbours + 7 correlated "negatives"), there are 7+7=14 anticorrelated pairs and $7 \times (7-1)/2 = 21$ correlated ones. Therefore, what is, on a large scale, actually an anticorrelation phenomenon, looks from the point of view of a two-point correlation analysis like a correlated one – and sure enough the net contribution of this particular pattern into the covariance matrix will be positive. [11]

5.5.5 Cross-talk correction for the multiplicity

It is clear that the cross-talk between neighbouring channels not only influences the correlation/fluctuation content of the observed events, but, being effectively positive, makes the measured multiplicity systematically larger. In this section I convert the knowledge of the 9% cross-talk effect (subsection 5.5.4) into a down-scaling correction factor for the total multiplicity. The simplest way of doing it is to say that a fitted multiplicity, based on weights w_0, w_1, w_2 ... (see formula 2.2), can be approximated by taking the total energy deposited in a pad over the run and dividing it by mean energy $\langle dE_{MIP} \rangle$. This is equivalent to saying that multiplicity is, effectively, proportional to the amplitude. Then, the extra multiplicity induced by the cross-talk from a typical adjacent channel is, on the average, a 9% addition, and this number needs to be multiplied by 2 for a typical channel which has two neighbours. More accurately, 14 out of 16 channels have two neighbours and 2 have 1 neighbour, therefore on the average the factor is $(14 \times 2 + 2 \times 1)/16 = 15/8$ rather than 2. The best is to take the subsample of the channel pairs from Fig. 5.7 such

[10] I am talking about calibrated amplitudes, where 0 corresponds to the pedestal – hence "positive" and "negative".

[11] Incidentally, this is a good insight into the "general theory" of correlation measures – a two point correlation approach does not tell the whole story; one really needs a scale-differentiated texture study !

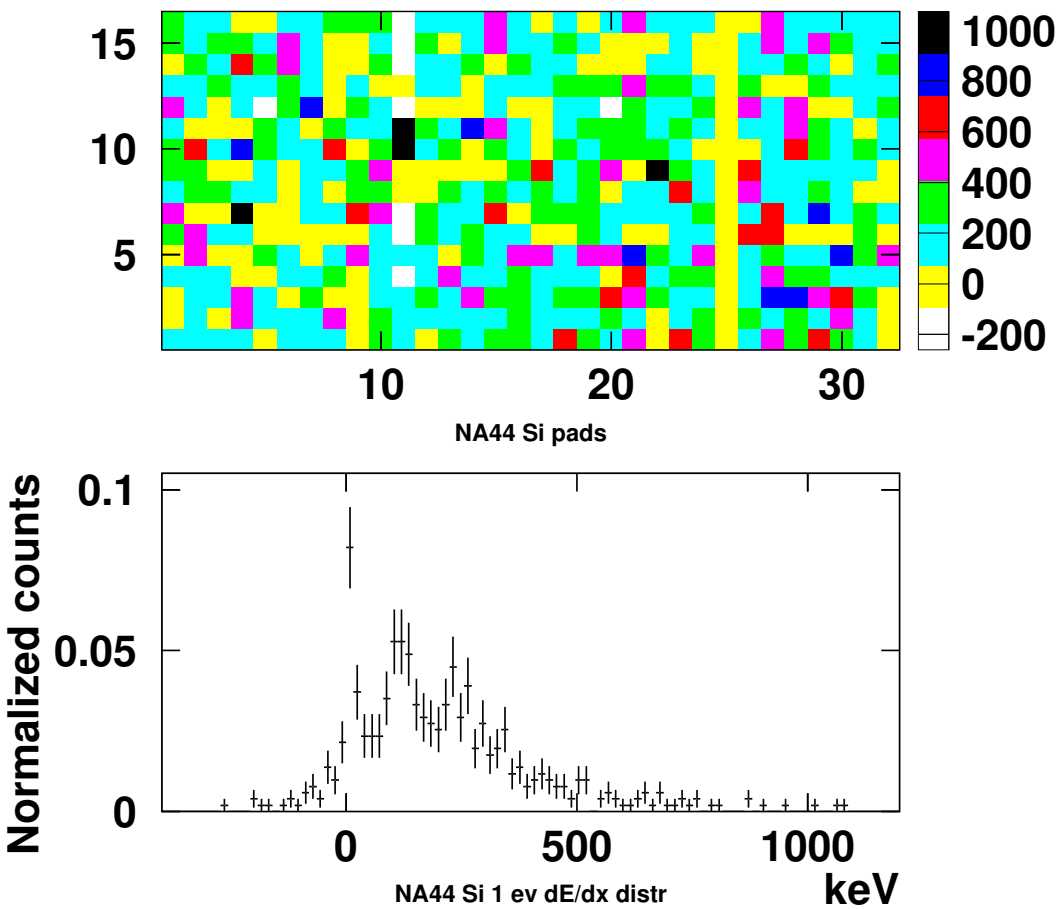

Figure 5.8: An example of a pathological event in the Si pad array. Top panel: the amplitude array. Sector number – horizontal axis, ring number – vertical axis. The δ-free acceptance, used in the analysis, is limited to sectors from 9 through 24. Sector 11 is affected by cross-talk. Sector 25 is dead. Bottom panel: amplitude distribution from this event only. It looks quite normal. The pedestal peak is fine, single and double hit peaks are clearly seen.

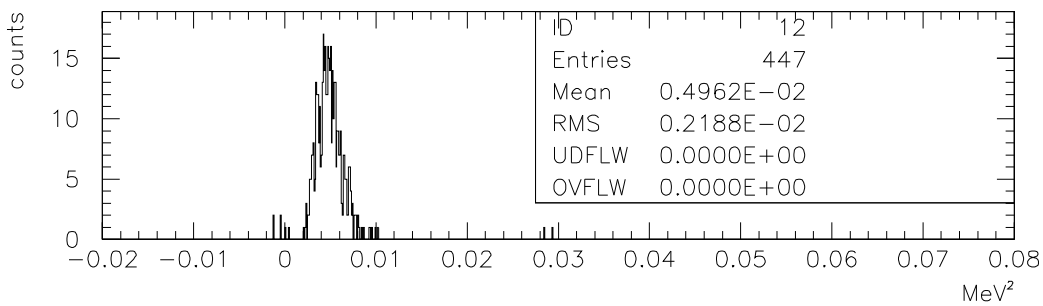

Figure 5.9: A distribution of the covariance matrix elements, that represent correlations between adjacent *inner* channels of sectors. Matrix elements involving dead channels are not shown. Run 3192.

that both channels are inner channels, and use Eq. 5.33 to get the effective coupling c. Then the multiplicity correction factor becomes $1/(1+15c/8)$. The distribution of the covariance matrix elements for such pairs is shown in Fig. 5.9. With its input, the correction factor becomes 0.86. A necessary caveat is that the 9% cross-talk is merely an "effective", approximate and integral way of looking at the problem. The level of approximateness implied by using the single correction for all channels is therefore not a reduction of accuracy, as compared to what has been done in Subsection 5.5.4.

5.5.6 The double differential multiplicity distribution

The double differential multiplicity data (Fig. 5.10) illustrate the quality of the detector operation, calibrations (Section 5.3), geometrical alignment and Jacobian correction (Section 5.4). The data set is composed of two pieces, obtained by switching the magnetic field polarity: run 3192 is used for sectors 9 to 24 (range of $\pi/2 < \zeta < 3\pi/2$); run 3151 is used for sectors 1 to 8 and 25 to 32 (range of $0 < \zeta < \pi/2$ and $3\pi/2 < \zeta < 2\pi$). The reason to disregard one side of the detector is additional occupancy due to δ-electrons, as was explained in section 5.2. Figure 5.10 demonstrates the quality of alignment as well, since the η and ζ along the horizontal axes are the aligned coordinates. Any geometrical offset of the detector makes acceptances of different pads non-equal and dependent on the pad position. The acceptance of each pad has been calculated in the aligned coordinates, and the $d^2N/\,d\zeta\,d\eta$ uses the actual acceptances $d\zeta$. The shape of the ζ dependence of $d^2N/\,d\eta\,d\zeta$ (left panel of Fig. 5.10) is flat as it should be for an event ensemble with no reaction plane selection. The η dependence (right panel of Fig. 5.10) shows

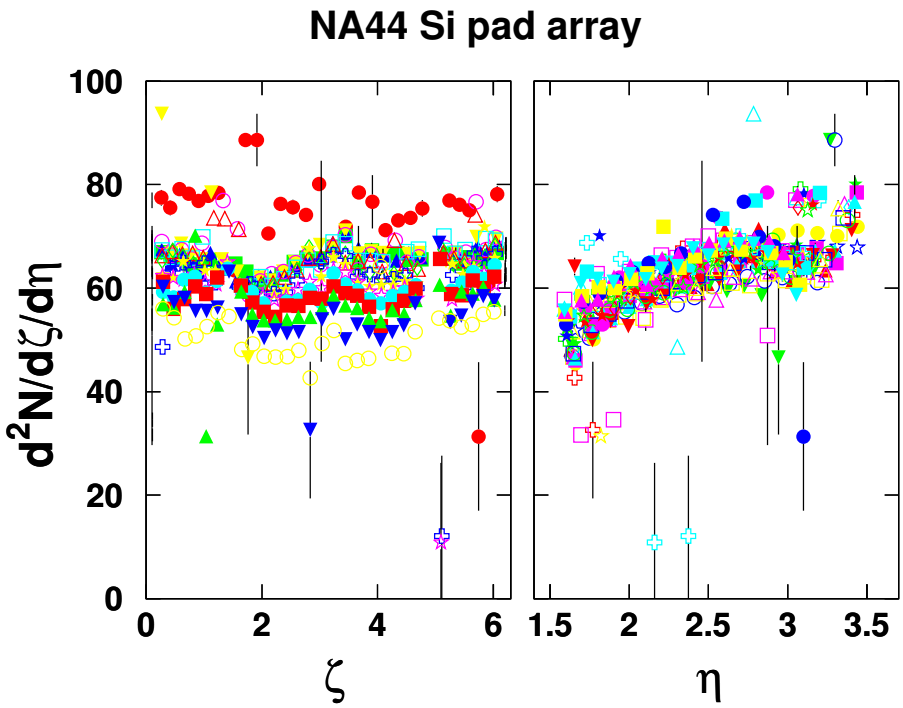

Figure 5.10: Double differential multiplicity distributions of charged particles plotted as a function of azimuthal angle ζ (with different symbols representing different rings) and of pseudorapidity η (with different symbols representing different sectors). The ζ and η are in the *aligned* coordinates.

increasing multiplicity towards midrapidity, [12] as is expected. The absolute value of $d^2N/\,d\zeta/\,d\eta$ includes a correction for the channel cross-talk, discussed in Subsection 5.5.5.

[12]or, more accurately, towards pion midrapidity – η can approximate y well for $m/p \ll 1$

5.6 Discrete Wavelet Transform power spectrum analysis of local fluctuations

5.6.1 The power spectrum – a way to accumulate texture information

In our work, a power spectrum analysis of event texture in pseudorapidity, η and azimuthal angle ζ based on a Discrete Wavelet Transformation (DWT)[17], is performed on a number of large event ensembles sampled according to their multiplicity, thereby studying the impact parameter dependence of the observables. DWT quantifies contributions of different ζ and η scales into the overall event's texture, thus testing for possible large scale enhancement.

DWT formalizes the images of the *PbPb* collision events in pseudorapidity η and azimuthal angle ζ by expanding them into a set of functions orthogonal with respect to scale and position in the (η, ζ) space, and allows one to accumulate the texture information by averaging the power spectra of many events. While the DWT analyzes the object (an image, a sequence of data points, a data array) by transforming it, the *full* information content inherent in the object is preserved in the transformation. Mathematically, this is expressed by stating that the discrete wavelet family of functions constitutes a *complete basis* in the space of all *measurable functions* defined on the continuum of real numbers $L^2(\mathbb{R})$. [13] This statement is known as the *multiresolution theorem* and constitutes the theoretical ground for the *multiresolution analysis*.

The simplest DWT basis is the Haar wavelet, built upon the scaling function [14] $\phi(x) = 1$ for $0 \leq x < 1$ and 0 otherwise. If the interaction vertex lies on the detector's symmetry axis, every pad's acceptance is a rectangle in the (ζ, η) space. Then, the Haar basis is the natural choice, as its scaling function in two dimensions (2D) $\Phi(\zeta, \eta) = \phi(\zeta)\phi(\eta)$ is just a pad's acceptance (modulo units). We therefore set up a 2D wavelet basis:

$$\Psi^{\lambda}_{m,i,j}(\zeta, \eta) = 2^m \Psi^{\lambda}(2^m\zeta - i, 2^m\eta - j). \tag{5.34}$$

$\Phi_{m,i,j}(\zeta, \eta)$ is constructed from $\Phi(\zeta, \eta)$ similarly. Here, m is an integer scale fineness index; i and j index the discrete positions of pad centers in ζ and η ($1 \leq m \leq 4$ and $1 \leq i, j \leq 16$ because we use $16 = 2^4$ rings and 16 sectors

[13] $L^2(\mathbb{R})$ is the space of functions whose second power is integrable: $\int_{-\infty}^{+\infty} |f(x)|^2 \, dx < \infty$.

[14] Some authors call it "mother function".

). Different values of λ (denoted as ζ, η, and $\zeta\eta$) distinguish, respectively, functions with azimuthal, pseudorapidity, and diagonal texture sensitivity:

$$\Psi^{\zeta} = \psi(\zeta)\phi(\eta), \quad \Psi^{\eta} = \phi(\zeta)\psi(\eta), \quad \Psi^{\zeta\eta} = \psi(\zeta)\psi(\eta) \tag{5.35}$$

In the Haar basis, for any variable x

$$\psi(x) = \begin{cases} +1 & : \quad 0 \leq x < \frac{1}{2} \\ -1 & : \quad \frac{1}{2} \leq x < 1 \\ 0 & : \quad otherwise \end{cases} \tag{5.36}$$

is the wavelet function. [15] Then, $\Psi^{\lambda}_{m,i,j}$ with integer m, i, and j are known [17] to form an orthonormal basis in $L^2(\mathbb{R}^2)$.

We adopt the existing [19] 1D DWT power spectrum analysis technique and expand it to 2D. The track density in an individual event is $\rho(\zeta, \eta)$ and its *local* fluctuation in a given event is $\sigma^2 \equiv \langle \rho - \bar{\rho}, \rho - \bar{\rho} \rangle$, where $\bar{\rho}$ is the average ρ (over the acceptance) in the given event. [16]

Using completeness of the basis, we expand

$$\rho - \bar{\rho} = \langle \rho, \Psi^{\lambda}_{m,i,j} \rangle \Psi^{\lambda}_{m,i,j} - \langle \bar{\rho}, \Psi^{\lambda}_{m,i,j} \rangle \Psi^{\lambda}_{m,i,j} \tag{5.37}$$

Notice that $\bar{\rho}$, being constant within detector's rectangular acceptance, is orthogonal to any $\Psi^{\lambda}_{m,i,j}$ with $m \geq 1$. Due to the orthonormality condition $\langle \Psi^{\lambda}_{m,i,j}, \Psi^{\lambda'}_{m',i',j'} \rangle = \delta_{\lambda,\lambda'}\delta_{m,m'}\delta_{i,i'}\delta_{j,j'}$, the $\rho - \bar{\rho}$ components for different scales do not form cross-terms in the σ^2 sum, and the sum contains no cross-terms between ρ and $\bar{\rho}$ for the four observable scales. Instead of a $\langle \rho, \Phi_{m=5,i,j} \rangle$ set, the Si detector energy amplitude array – its closest experimentally achievable approximation – is used as the DWT input. We used WAILI [81] software library to obtain the wavelet decompositions.

The Fourier power spectrum of a random white noise field is known to be independent of frequency [80]. We are looking for dynamical textures in the data, and therefore would like to treat the random white noise case as a "trivial" one to compare with. Therefore it is interesting to reformulate this property for wavelets, where scale plays the same role as frequency in Fourier analysis. To do that, we link scales with frequencies, or in other words, we must understand the frequency spectra of the wavelets. The Fourier images

[15] Some authors call it "father function".

[16] In our notation, a scalar product of f and g in the $L^2(\mathbb{R}^2)$ space is denoted as $\langle f, g \rangle$: $\langle f, g \rangle = \int\int f(x,y)g(x,y)\,dx\,dy$. Repeated indices are being summed over, even if the summation symbol is not written explicitly.

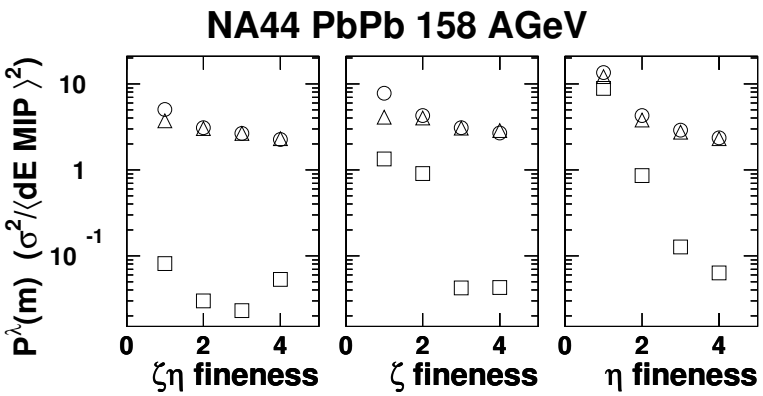

Figure 5.11: Power spectra of 7×10^3 events in the multiplicity bin $326 < dN/d\eta < 398$. ◯ – true events, △ – mixed events, □ – the average event.

of 1D wavelet functions occupy a set of wave numbers whose characteristic broadness grows with scale fineness m as 2^m; 2^{2m} should be used in the 2D case. Discrete wavelets of higher orders have better frequency localization than the Haar wavelets. Despite this advantage, we use Haar because only Haar allows one to say that the act of data taking with the (binned !) detector constitutes the first stage of the wavelet transformation.

In 2D, we find it most informative to present the three modes of a power spectrum with different directions of sensitivity $P^{\zeta\eta}(m)$, $P^{\zeta}(m)$, $P^{\eta}(m)$ separately. We define the *power spectrum* as

$$P^{\lambda}(m) = \frac{1}{2^{2m}} \sum_{i,j} \langle \rho, \Psi^{\lambda}_{m,i,j} \rangle^2, \tag{5.38}$$

where the denominator gives the meaning of spectral *density* to the observable. So defined, the $P^{\lambda}(m)$ of a random white noise field is independent of m. In the first approximation, the white noise example provides a base-line case for comparisons in search for non-trivial effects.

5.6.2 Static and dynamic texture. Event mixing as a way to subtract the static contribution.

Figure 5.11 shows such power spectra for one multiplicity range. The unit on the vertical scale $(\sigma^2/\langle dE_{MIP}\rangle^2)$ is chosen so that the power of the fluctuation whose variance σ^2 equals the squared mean energy loss by a minimum ionising particle traversing the detector, is the unit. The first striking

feature is that the power spectra of physical events are indeed enhanced on the coarse scale. The task of the analysis is to quantify and, as much as possible, eliminate "trivial" and experiment-specific reasons for this enhancement.

The average event, formed by summing amplitude images of the measured events in a given multiplicity bin, and dividing by the number of events, has a much reduced texture as statistical fluctuations cancel (shown as □ in Fig.5.11). Average events retain the texture associated with the shape of $d^2N/\,d\eta\,d\zeta$, with the dead channels and the finite beam geometrical cross-section (though this is only partially visible in the average event, due to the fact that event averaging is done without attempting to select events according to the vertex position). $P^\lambda(m)$ is proportional to the variance, or squared fluctuation σ^2. Therefore, for Poissonian statistics of hits in a pad, the event averaging over M events should decrease $P^\lambda(m)$ by a factor of M. The average event whose power spectrum is shown on Fig. 5.11 is formed by adding 7×10^3 events, however its $P^\lambda(m)$ is down less than 7×10^3 compared to that of the single events. This demonstrates that the average event's texture is not due to statistical fluctuations, but rather, *predominantly* due to the systematic uncertainties listed. Consequently, we can use the average event's $P^\lambda(m)$ to estimate the magnitude of the static texture-related systematics. As seen from Fig. 5.11, the systematics are orders of magnitude below the $P^\lambda(m)$ of single events (true or mixed), with the exception of pseudorapidity, where non-constancy of $dN/\,d\eta$ over the detector's acceptance is visible.

The way to get rid of the "trivial" or static texture is to use mixed events, taking different channels from different events. The mixed events preserve the texture associated with the detector position offset, the inherent $dN/\,d\eta$ shape and the dead channels. This is *static* texture as it produces the same pattern event after event while we are searching for evidence of dynamic texture. We reduce sources of the static texture in the power spectra by empty target subtraction and by subtraction of mixed events power spectra, thus obtaining the *dynamic texture* $P^\lambda(m)_{true} - P^\lambda(m)_{mix}$. In order to reproduce the electronics cross-talk effects in the mixed event sample, the mixing is done sector-wise, i.e. the sectors constitute the subevents subjected to the event number scrambling. Its multiplicity dependence is plotted on Figure 6.1.

For comparison with models, a MC simulation (done with RQMD [57]) includes the known static texture effects and undergoes the same elimination procedure. This allows the effects irreducible by the subtraction methods to be taken into account in the comparison. One such example is the finite beam size, which has been shown by the MC studies to cause the RQMD points to rise with $dN/\,d\eta$.

5.7 Analysis of background effects

5.7.1 Sources of background

In this section the words "backgrounds", "background effects" should be understood in the technical and literal sense, as the causes responsible for the electrical signals produced by the experimental apparatus and recorded, but unrelated to the physics of the $PbPb$ collisions. In the course of data taking for this analysis, the following effects gave rise to the detector occupancy even in the absence of the $PbPb$ interactions:

1. nucleus-nucleus interactions between the incident Pb and the material of the 1 cm thick styrofoam target holder (the "empty target")

2. imperfections of the detector: due to the non-zero pedestal width (seen on Fig. 5.1), the probability of detecting a "hit" even in the absence of a particle track is finite for any reasonable hit threshold. What is worse (and that has been seen in our detector) is the fact that the fake hits tend to arrange themselves in regular patterns. After an event-display study on a statistics of the order of 10^4, it was concluded that the pathological patterns can be roughly categorized in two groups:

   (a) Sometimes, several fake hits appear simultaneously in channels served by the same AMPLEX chip. Their amplitude can reach values typical of and exceeding those of the typical tracks. This problem is addressed by the *sector-wise* event mixing, as discussed in Subsection 5.6.2.

   (b) A pattern of "reversed $dN/d\eta$ shape" was seen: a systematic increase of channel amplitude towards the outer rings (where physics multiplicity is lowest – hence the word "reversed"). Subevent mixing is of little help here because these are large scale patterns. However, inspection of empty target runs showed that the same events exist there. This, on the one hand, rules out "physics" and pile-up explanations; on the other – enables a correction based on the empty target subtraction.

   The pathologies from group 2a affect power spectra components (PSC) of the azimuthal and pseudorapidity modes; those from group 2b – PSCs of the pseudorapidity mode.

3. δ-electrons not deflected by the field and hitting the "clean" side of the detector.

4. random tracks whose origin is unrelated to our experiment

Items 1 and 4 are correctable by an empty target subtraction procedure unconditionally; items 2 and 4 can be corrected by event mixing, and by empty target subtraction if one assumes that it reproduces itself in the empty target events of the same total multiplicity as the given one. Item 3 has been shown by MC (described in Section 5.8) to be negligible.

5.7.2 Background subtraction

Our final goal is correcting the average power spectrum components (PSC) for the background contribution. Let me first introduce the basic notions and notation. I will denote the total amplitude from the analyzed part of the detector as x, and distinguish three kinds of probability density distribution:

- $F(x)$ – non-interactions. $F(x)$ is found in the empty target run.
- $G(x)$ – minimum bias sample of $PbPb$ interactions. This distribution can be only obtained by on-line or off-line discrimination. The NA44 design emphasized triggering on central events with high rates, with no attention paid to obtaining unbiased $G(x)$ in a broad range of x. This has been discussed at length in Section 3.2.
- $P(x)$ – "valid beam" (VB) sample. It consists of two fractions:
  1. minimum bias sample of interactions. Their fraction in the sample equals the interaction probability $\alpha \ll 1$ (Section 2.3).
  2. non-interactions – the predominant majority, fraction $1 - \alpha$.

For definiteness, let's talk about one certain direction mode and one certain scale of PSC, and use notation $\mathcal{P}_F$, $\mathcal{P}_G$, $\mathcal{P}_P$ for the PSCs in the respective trigger modes. It turns out, that under reasonable assumptions, for all multiplicity bins except the one which contains 0, the following formula can be *justified*:

$$\mathcal{P}_{G,x} = \mathcal{P}_{P,x} - \mathcal{P}_{F,0} \tag{5.39}$$

The justification of this intuitive formula is given in Appendix B.

As is clear from the Appendix, this approach is not perfect because it ignores large amplitude events in the empty target sample. Such events, although rare, do occur there. Moreover, those events are often dominated by the correlated noise (already discussed in Subsection 5.7.1) with pronounced

large scale texture features. In terms of multiplicity, these effects are localized not in the zero bin (between and -5 MeV and +5 MeV), but rather, spread over the range of total ionizations 10-40 MeV (counting only the δ-free side of the detector). The method of correction is empty target background subtraction according to formula 5.39. The zero bin had to be extended to include the affected multiplicity range, as shown in Fig.6.1. The same zero bin was used in the physics and empty target runs.

Events with negative total amplitude get into bins with "negative" values of $dN/d\eta$. Such events happen in non-central trigger runs due to the fact that the low-amplitude behaviour of the detector is dominated by the noise which has inherent correlations of purely instrumental nature.

5.8 GEANT-based Monte Carlo simulation of the detector response

I have written a Monte Carlo detector response simulation program to study the experiment's sensitivity to the potential signals and to the expected backgrounds. The program uses the GEANT 3 [78] Detector Description and Simulation Tool. The following aspects of the actual experiment are (more or less realistically) reflected in the MC:

- Geometry, sizes, materials and mutual distances of the Pb target, the Si pad array, and of the T0 counters. The geometry is shown on Fig. 2.2.
- Magnetic field: it is taken to be uniform; the maximal magnitude of field in the first dipole is taken to be true "everywhere", thus somewhat exaggerating the bending ability of the field. This exaggeration, though, seems important only for the δ-electron simulation.
- Interaction of emitted particles (hadrons, leptons and gammas) with the materials of the target, air and the T0 counters on their way from the vertex to the detector. Included are: pair production, bremsstrahlung, decays, Compton scattering and photoelectric effect, δ-ray production and multiple scattering, hadronic processes. Multiple scattering inside the Si was switched off because the simulated setup has nothing behind the Si.
- Fluctuations of ionization energy loss in the detector (via Landau's theory [76]); the observed resolution of the channels, custom fitted to every channel's calibrated characteristics with the level of detail used in the calibration fits, as described in section 5.3.

An interface was created to feed RQMD events (or other events written out in the RQMD-like format) into the detector response simulation.

5.9 Systematic errors

Here I give a brief summary of the systematic errors in the measurements of the DWT texture correlation observable $P_{true} - P_{mix}$. Static texture and dynamic background texture present the largest problem in the search for the phase transition-related dynamic texture via power spectra of local fluctuations. The method of solving the problem is comparison with the reference sample created by event mixing. Thus the $P_{true} - P_{mix}$ observable was created.

By static texture we mean texture which reproduces its pattern event after event. This can be either because it is coupled with detector channels (dead pads, geometry distortion, channel cross-talk, etc) or because of static physics features such as $dN/d\eta$ shape. We eliminate the static texture from the texture correlation observable by empty target subtraction (Subsection 5.7.2) and by subtraction of mixed events power spectra (Subsection 5.6.2). For comparison with models, a Monte Carlo simulation of the Si detector is used (Section 5.8). It includes the known static texture effects and undergoes the same procedure to remove the effects. The "irreducible remainder" is the residual effect which may

1. survive the elimination procedure
2. emerge *as a difference* between the data, subjected to the elimination procedure, and the MC analyzed in the same manner.

Table 5.2 lists the sources of static texture and summarizes the methods of their treatment. We group the *background texture* sources according to similarity of manifestation and treatment, into

- statistical fluctuations
- static texture
- background dynamic texture

The statistical fluctuation is the most trivial item in this list. Both event mixing (provided that mixing is done within the proper multiplicity class) and MC comparison solve this problem. The statistical fluctuations do not result in irreducible systematic errors.

The static texture group includes:

Source	Correction				Irreducible remainder estimate
	subtract empty target	event mixing: subtract mixed events	event mixing: preserve sectors	do MC	
stat. fluctuations	N/A	yes	N/A	yes	0.
$dN/d\eta$ shape, offset, dead pads	N/A	yes	OK	yes	0.
finite beam Xsection 1×2 mm	N/A	N/A	N/A	yes	0.14
background hits	yes	yes	yes	can't	> 0.070, < 0.37
channel Xtalk 8.5% for neighbours	N/A	yes	yes	can't	

Table 5.2: Sources of background texture (dynamic and static) and their treatment. The irreducible remainder estimate is quoted for diagonal texture correlation in the $326 < dN/d\eta < 398$ bin, and is expressed in the units of $\sigma^2/\langle dE_{MIP}\rangle^2$; see text for information on how it was obtained.

- geometrical offset of the detector with respect to the beam's "center of gravity" in the vertical plane (determined in Section 5.4)
- dead pads (Section 5.1)
- $dN/d\eta$ shape – a genuine large scale multiparticle correlation sensitive to the physics of the early stage of the collision

Cleanliness of the static texture elimination via event mixing has been checked by simulating the contributing effects separately. First, by running the detector response simulation on MC-generated events *without* the beam/detector offset and with a beam of 0 thickness it was ascertained that the remaining dynamic texture is very small compared with the systematic errors due to the background Si hits and the beam geometrical cross-section, for all scales and all directional modes λ. Due to the finite size of the multiplicity bin, the mixed events consist of subevents coming from events of different total multiplicity. With the sector-wise mixing, this causes an additional sector-to-sector variation of amplitude in the mixed events, thus resulting in an enhancement of P^{ζ}_{mix} primarily on the finest scale, with respect to P^{ζ}_{true}. (If the mixing is done ring-wise, rather than sector-wise, the same effect is seen in P^{η}_{mix}, rather than P^{ζ}_{mix}.) On Fig. 6.1, this effect can be seen as the $P^{\zeta}_{true} - P^{\zeta}_{mix}$ values progressively grow negative with multiplicity in the finest scale plot. However, as can be seen on the same figure, the effect is small compared with the total

systematic errorbars shown as boxes.

The background dynamic texture group includes:

- elliptic and directed flow
- finiteness of the beam cross-section
- background hits in the Si (Subsection 5.7.1)
- channel-to-channel cross-talk (Section 5.5)

Elliptic and directed flow, observed at SPS [10], are large scale dynamic texture phenomena of primarily azimuthal (elliptic) and diagonal (directed flow) modes. Because both reaction plane and direction angle vary event by event, the respective dynamic textures can not be subtracted by event mixing, unless the events are classified according to their reaction plane orientation and the direction angle, with mixing and $P_{true} - P_{mix}$ subtraction done within those classes. Neither reaction plane nor direction angle was reconstructed in the present analysis, and the $P_{true} - P_{mix}$ (especially that of the azimuthal and diagonal modes on the coarse scale) retain the elliptic/directed flow contribution. The effects of flow on dynamic texture observables are smaller than other texture effects, so they can not be singled out and quantified in this analysis.

The finite beam cross-section effect belongs to this group, despite the fact that a very similar effect of geometrical detecor/beam offset has been classified as static texture. An effect must survive mixing with its strength unaltered in order to be fully subtracted via event mixing. Preserving the effect of the random variations in the $Pb + Pb$ vertex on the power spectra in the mixed events requires classification of events according to the vertex position and mixing only within such classes. This requires knowledge of the vertex for each event, which is not available in this experiment. Therefore, MC simulation of the beam profile remains the only way to quantify false texture arising from vertex variations. MC studies with event generators show that the beam spatial extent and the resulting vertex variation is the source of the growth of the coarse scale *azimuthal* texture correlation with multiplicity (see Fig. 6.1). Uncertainty in our knowledge of the beam's geometrical cross-section must be propagated into a systematic error on $P_{true} - P_{mix}$. Here is how it was done:

1. run MC for beam thickness 1×2 mm, with the calibrated detector offset
2. run MC for beam thickness 1.5×3 mm, with the calibrated detector offset

3. take 50% of the difference between steps 1 and 2 as the estimate of the error

The other two effects in this group are difficult to separate and simulate and the error estimate reflects the combined effect. The systematic errors were evaluated by removing the Pb target and switching magnetic field polarity to expose the given side of the detector to δ-electrons (from the air and T0), while minimizing nuclear interactions. This gives an "analog" generator of uncorrelated noise. The runs used for this purpose are the positive field polarity runs listed in Table 5.1. All correlations (i.e. deviations of $P^{\lambda}(m)_{true}$ from $P^{\lambda}(m)_{mix}$) in this noise generator are treated as systematic uncertainties. Thus this component of the systematic error gets a sign, and the systematic errors are asymmetric. The effect of increasing texture correlation (for diagonal and azimuthal modes) with multiplicity on the coarse scale, attributed to the geometrical offset of the detector with respect to the beam (the leading one in the static group), is present in the switched polarity empty target runs as well. For this reason, it was impossible to disentangle the background dynamic contribution on the coarsest scale. In Table 5.2, the "irreducible remainder estimate" for the diagonal, coarse scale is bracketed with two numbers, which form the lower and upper estimates. The lower estimate is obtained by taking the scale one unit finer and quoting its number. This, indeed, sets the lower limit because the deviations of $P^{\lambda}(m)_{true}$ from $P^{\lambda}(m)_{mix}$ generally grow with scale coarseness. The upper limit is set by ascribing the *entire* texture correlation, observed in the δ-electron data, to the background hits and channel cross-talk, and ignoring the fact that significant portion of it must be due to the vertex fluctuation (finite beam profile). This upper limit is likely to be a gross overestimation, and in Fig. 6.1 we show systematic errors, obtained by adding in quadrature the finite beam error with the background hit error.

Chapter 6

Results of the event-by-event multiparticle texture analysis and their meaning

In this Chapter I present results of the multiparticle texture analysis described in Chapter 5. In order to appreciate the meaning of the results, one has to quantify the sensitivity of the method, and this study is documented in Section 6.3.

6.1 The DWT texture correlation

Fig. 6.1 presents a comparison of the DWT dynamic texture in the measured and RQMD-simulated $Pb + Pb$ collision events. The three directional sensitivity modes (diagonal $\zeta\eta$, azimuthal ζ, and pseudorapidity η) have four scales each, so that there are 12 sets of points in the DWT dynamic texture as a function of the charged multiplicity $dN_{ch}/\,d\eta$ bin. [1] The systematic errors on the points (shown by vertical bars) have been evaluated following the procedure described in detail in Section 5.9.

Fig.5.11 demonstrated that the major fraction of the observed texture exists also in mixed events. A detailed account of the causes was discussed in the preceding section (Section 5.9) , including known physics as well as instrumental effects. It is therefore clear that the observable most directly related to the dynamical correlations/fluctuations is not $P^{\lambda}(m)$ (introduced in 5.6) , but $P^{\lambda}(m)_{true} - P^{\lambda}(m)_{mix}$. We find that if one uses the concepts of fluctuation and scale simultaneously, so that scale-local description of fluctuations is possible, then the term "correlation" becomes redundant for describing

[1] The binning was done in the total ionization amplitude; then charged multiplicity was assigned to those bins by dividing total ionization by mean ionization of a pion with $p_T = 0.4$ GeV/c.

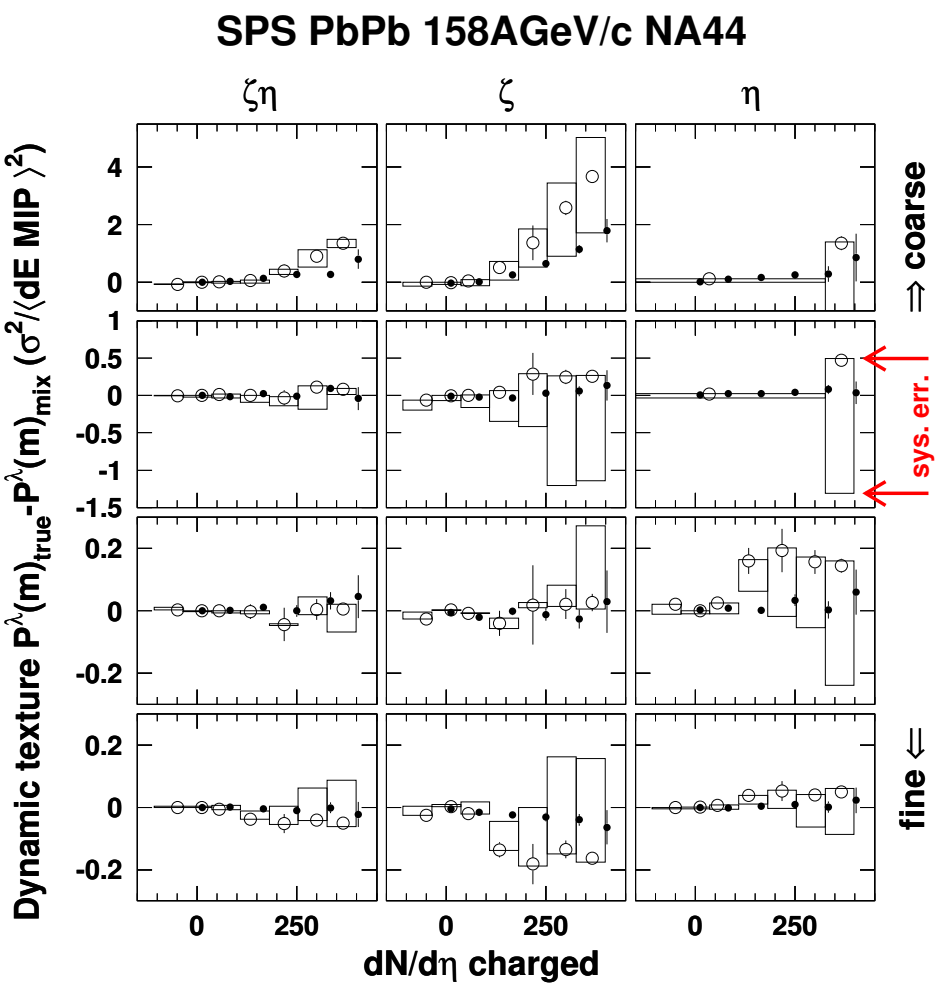

Figure 6.1: Multiplicity dependence of the texture correlation. ◯ – the NA44 data, • – RQMD. The boxes show the systematic errors vertically and the boundaries of the multiplicity bins horizontally; the statistical errors are indicated by the vertical bars on the points. The rows correspond to the scale fineness m, the columns – to the directional mode λ (which can be diagonal $\zeta\eta$, azimuthal ζ, and pseudorapidity η).

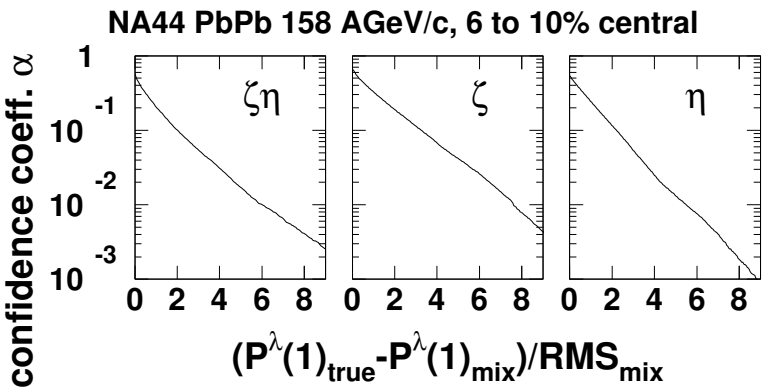

Figure 6.2: Confidence coefficient as a function of the fluctuation strength. RMS_{mix} denotes $\sqrt{\langle P^\lambda(1)^2_{mix} - \langle P^\lambda(1)_{mix}\rangle^2\rangle}$. This is the coarsest scale.

texture, because a "correlation" on some scale can always be thought of as a "fluctuation" on a larger scale. For example, density of paint on the surface of a chess board looks like a "correlation without fluctuation" on the scale of each of its 64 fields, and at the same time, as a "fluctuation without correlation" on the scale of the entire chess board. Alternatively, if one uses the term "correlation" and specifies scale, then the term "fluctuation" becomes redundant. This quantity, normalized to the RMS fluctuation of $P^\lambda(m)_{mix}$, can be used to characterize the relative strength of local fluctuations in an event. The distribution for different λ (or directions) on the coarsest scale is plotted on Figure 6.2 in an integral way, i.e. as an $\alpha(x)$ graph where for every x, α is the fraction of the distribution above x.

$$\alpha(x) = \int_x^\infty \frac{dN}{d\xi}\, d\xi \Big/ \int_{-\infty}^{+\infty} \frac{dN}{d\xi}\, d\xi, \tag{6.1}$$

where ξ denotes the fluctuation strength

$$\xi = \frac{P^\lambda(1)_{true} - P^\lambda(1)_{mix}}{RMS(P^\lambda(1)_{mix})}, \tag{6.2}$$

and $dN/\,d\xi$ is the statistical distribution of ξ, obtained from the experimentally known distributions of $P^\lambda(1)_{true}$ and $P^\lambda(1)_{mix}$. Expression 6.2 is constructed to be sensitive to the difference between $P^\lambda(1)_{true}$ and $P^\lambda(1)_{mix}$, while minimizing detector specifics to enable comparison between different experiments in future. The latter is accomplished by normalizing to RMS_{mix}. This normalization also eliminates the trivial multiplicity dependence of the observable.

The fluctuation strength observable provides a limit on the frequency and strength of the fluctuations and expresses the result in a model-independent way. The *confidence level* with which local fluctuations of a given strength (expressed through the EbyE observables via Eq. 6.2) can be excluded is then $1-\alpha$. Fluctuations greater than $3\times RMS_{mix}$ are excluded in the azimuthal and pseudorapidity modes with 90% and 95% confidence, respectively. The monotonic fall of the curve is consistent with the absence of abnormal subsamples in the data.

RQMD events were fed into the GEANT detector response simulation (Section 5.8) and analyzed using the same off-line procedure as used for the experimental data. The detector offset with respect to the beam center of gravity and the beam profile were included in the simulation. In a separate simulation run, the beam profile was identified as the cause of the rise of the azimuthal dynamic texture with the multiplicity on the coarse scale. In our experiment, this purely instrumental effect dominates the azimuthal component of the DWT dynamic texture.

The most apparent conclusion from Fig. 6.1 is that a large fraction of the texture (seen on Fig. 5.11) is not dynamic i.e. not different between true and mixed events. Being monotonic (or absent), the change of the data points with multiplicity does not reveal any evidence of a region of impact parameters/baryochemical potentials with qualitatively different properties, such as those of a critical point neighbourhood. The RQMD comparison confirms that particle production via hadronic multiple scattering, following string decays (without critical phenomena or phase transition) can explain the observed results when detector imperfections are taken into account. More detailed discussion of the implications of these data on various phase transition models will be given in Sections 6.4 and 6.5.

6.2 The multifireball event generator.

Interesting physics can be manifested in the ensemble probability density distributions as well as in the event-by-event (EbyE for short) observables. To illustrate the power of the EbyE observable we used, we should construct final states of charged particles indistinguishable from the point of view of "traditional", or ensemble-wise observables, such as

1. dN/dy distribution
2. dN/dp_T, $1/mT\, dN/dm_T$ distribution etc.
3. multiplicity distribution

and compare the sensitivity of the above-mentioned observables with that of the EbyE one. In practice, we can accomplish the situation where the difference in texture, or EbyE features, is dominant and the difference in the ensemble-wise distributions shows up like a next order effect. This can be accomplished by tuning parameters of the model. In this situation, we test our experiment's (detector + software) sensitivity to the non-trivial features, using detector response simulation and the actual analysis software.

The sensitivity study was performed using a multifireball event generator created specially for this purpose. Writing a simple texture generator was undertaken to provide a model-independent calibration of the texture sensitivity of this analysis. The generator is used to produce textures of known magnitude; we do not suggest that the physics of $Pb + Pb$ collisions is properly described by a superposition of fireballs of a fixed size.

6.2.1 Physics

This picture of hadronization is inspired by Van Hove's scenario [87] of a first order phase transition via droplet fragmentation of a QGP fluid. QGP droplets are dynamic *spatial* texture phenomena. However, we measure texture in the two dimensional space of directions, spanned by polar and azimuthal angles. The mechanism that makes us sensitive to the spatial texture is longitudinal flow; the concept of boost-invariant longitudinal expansion was introduced by Bjorken [82]. Two droplets, separated along the longitudinal coordinate, will be separated in y and η. As long as there is longitudinal expansion, a spatial texture will be manifested as (pseudo)rapidity texture. In the multifireball event generator, we generate the pseudorapidity texture explicitly, omitting the spatial formulation of the problem. The total p_T of each fireball is 0; its total p_Z is chosen to reproduce the observed dN/dy of charged particles by Lorentz-boosting the fireballs along the Z direction, keeping the total $\vec{p}$ of an event at 0 in the rest frame of the colliding primaries. The fireballs hadronize independently into charged and neutral pions and kaons mixed in a realistic proportion. By varying number of particles N_p per fireball, one varies "grain coarseness" of the event texture in η.

To illustrate the discussion, Fig.6.3 presents examples of dN/dy distributions in four events with different number of fireballs. The dynamic textures seen on the figures are peculiar to these particular events and are gone after dN/dy of many events are added.

- Particle production:

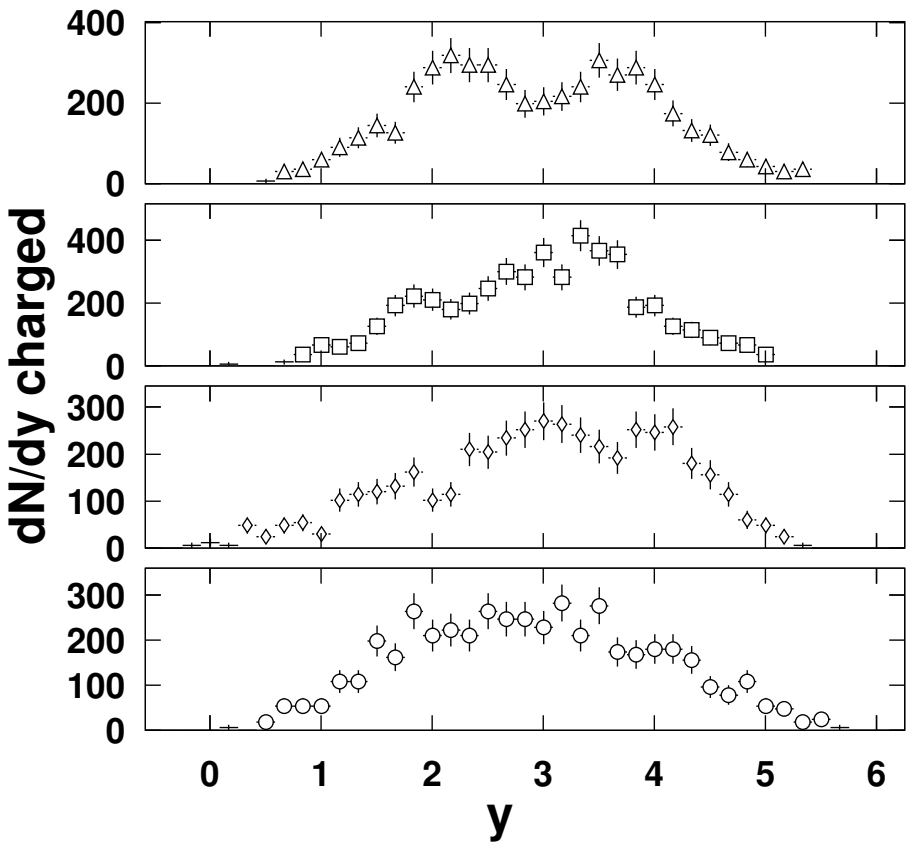

Figure 6.3: dN/dy distribution of charged particles in the multifireball event generator in four *individual events* with different number of fireballs: $\triangle$ – 2 fireballs, $\square$ – 4 fireballs, $\diamond$ – 8 fireballs, $\bigcirc$ – 16 fireballs. One can see how the texture becomes smoother as the number of fireballs increases. We remind the reader that the detector's active area covers 2π azimuthally and pseudorapidity 1.5 to 3.3. In general, acceptance limitations make it more difficult to detect dynamic textures.

- creates only kaons (charged and neutral) and pions (charged and neutral) in a proportion realistic for the SPS PbPb data. [2]
- Glauber model of the dependence of the number of participants on the impact parameter (done as a Monte Carlo generator of a random number of participants N_{part} for a given impact parameter)
- The total multiplicity of mesons in an event scales as N_{part}, with a fixed coefficient.

- Kinematics:
  - a Gaussian [3] distribution of p_X, p_Y, p_Z with adjustable sigma, same for the three directions (isotropy) is simulated for an individual fireball. The data on dN/dy exclude pT/pZ isotropy – an isotropic fireball with $< p_T >$ about 0.35 GeV/c has dN/dy with RMS 0.7 – much narrower than seen in the data; therefore, the longitudinal flow needs to be simulated.
  - The longitudinal flow is simulated by randomly (but conserving total p_Z) boosting individual fireballs along the Z direction.

$$\frac{dN}{dp_Z} = \frac{dN}{dy}\frac{dy}{dp_Z} = \frac{dN}{dy}\frac{1}{E}, \tag{6.3}$$

In this formula, N, y, p_Z, E refer to fireballs, rather than particles; the fireballs do not move transversely. In this formula, I take Gaussian dN/dy with an adjustable parameter σ_{long}. [4] σ_{long} of a fireball is adjusted by comparing the final dN/dy (fireballs + the longitudinal flow) with the data. Fig. 6.4 illustrates the result of the adjustment: despite the different event-by-event dynamics, the ensemble observable dN/dy for negative hadrons looks very similar! (These results were obtained with σ_{long} =1.6)

---

[2]Specifically, the following are probabilities for a simulated particle to assume a particular identity: π^+ - 0.260; π^- - 0.279; π^0 - 0.270; K^+ - 0.0635; K^- - 0.0317; K^0 - 0.0952.

[3]Not the most realistic one, it is chosen because it enables fast and simple momentum-conserving generation of random momenta.

[4]In this approach, one obtains particles with a Gaussian dN/dy from a superposition of multiple isotropic fireballs in a single event. A single isotropic fireball can not produce a realistic combination of y and pT distributions.

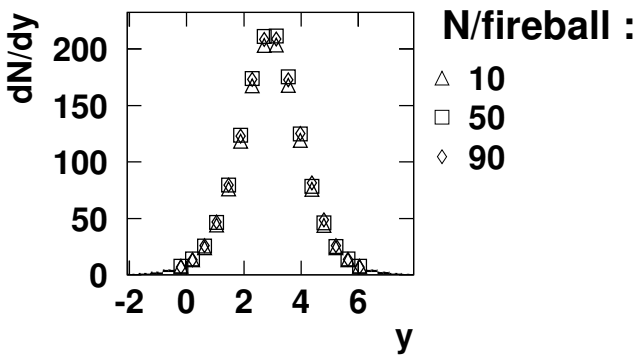

Figure 6.4: dN/dy from negative hadrons obtained in 5% most central events of the multifireball event generator with different clustering parameter N_{ch}/fireball.

- Fireball multiplicity:

  This is a variable parameter. The fireball multiplicity is Gaussian with variable mean and sigma [5], subject to the constraint of fixing the total event multiplicity in a given event (Subsection 6.2.2 describes the mathematical technique).

6.2.2 Mathematics.

I can generate N random numbers, so that an individual number's distribution (same for all of them) approaches the specified distribution, while enforcing strictly the constraint of the specified sum of these N numbers. This ability is essential to conserve momentum $\sum p_X = 0, \sum p_Y = 0, \sum p_Z = 0$, and conserve the total multiplicity while simulating individual fireballs, thus reproducing the given multiplicity distribution regardless of the number and size of the individual fireballs. In principle, the constraint of the sum distorts the specified single-number distribution. The degree of the distortion depends on the sum and the parameters of the single-number distribution. The problem of generating a multi-variate distribution is discussed in [83], it is recommended to do a succession of conditional single-variate distributions. The use of the Central Limit Theorem to (approximately) integrate the successive single-variate distributions is as in [84]. Appendix D gives the details. In course of the simulation of an event, we apply the same technique for two problems:

[5] Section 6.3 describes what they are

- particle number conservation is enforced when random number of particles is split between clusters. The cluster multiplicity has a Gaussian distribution with RMS much less than the mean. The mean is the "clustering parameter" of the model. The number of clusters in a particular event and the *random* cluster multiplicities are made up based on the "clustering parameter" of the run and the total multiplicity of the event.

- momentum conservation for the entire event. The longitudinal expansion prescribes random p_Z momenta of the clusters (see Eq.6.3); p_X and p_Y momenta of each cluster are 0.

- momentum conservation within a fireball. The total momentum is being split between the particles of the fireball.

6.3 Sensitivity of the method

The sensitivity study was performed using the multifireball event generator created specially for this purpose and described in Section 6.2. Writing an event generator with a very simple physics behind it was preferred to searching for an existing one with potentially deep, relevant and interesting physics, for the following reasons:

- an argument, based on a result obtained from an event generator with a simple-minded simulation of the interesting physics effects, is more general than the one made on the basis of a detailed, physically deep calculation of one *particular* theoretical scenario, with one particular set of assumptions

- a *calibration* of the sensitivity of the method, that is, the job of establishing the quantitative connection between a *standard* effect and the response of the experiment is best done with an *immutable* standard

The longitudinal flow of fireballs manifests itself primarily in the rapidity mode. We simulated average fireball multiplicities of 10, 50, 90 (with RMS fluctuation of 3) and larger. The average fireball multiplicity is referred to as a "clustering parameter", and characterizes the "grain coarseness" of the pseudorapidity texture. More detailed description of the model is given in Section 6.2. Fig. 6.5 shows comparison of our data with the simulated pseudorapidity texture. For clustering parameters 50 and 90, on a statistics of $\sim 10^4$ events the detector+software sees a difference between the hadronizations with different mean fireball multiplicities. The signal grows with the multiplicity and with

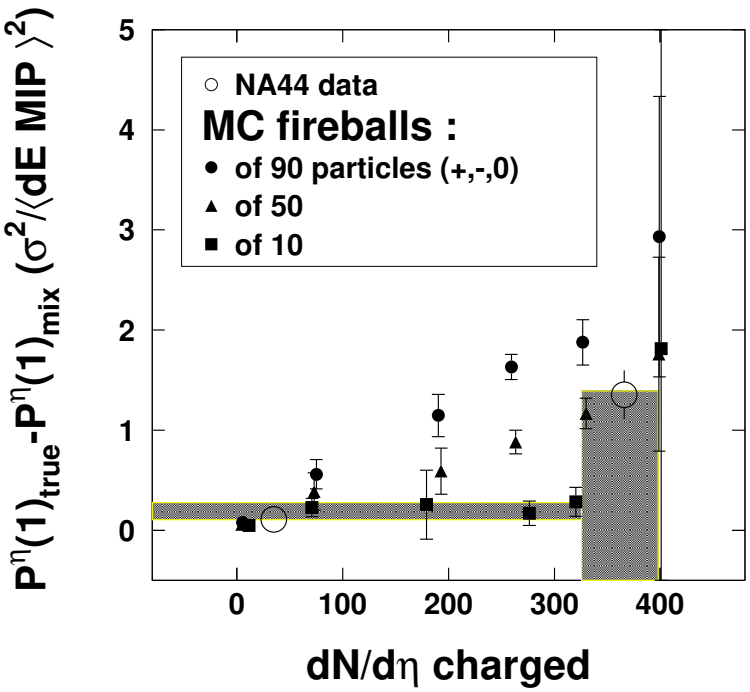

Figure 6.5: Coarse scale η texture correlation in the NA44 data, shown by ◯ (from the top right plot of Figure 6.1), is compared with that from the multifireball event generator for three different fireball sizes. Detector response is simulated. The boxes represent systematic errorbars (see caption to Fig. 6.1).

the clustering parameter. Fig. 6.5 provides *quantitative* information on the sensitivity of the texture measurements by relating the expected strength of response to the strength of texture via Monte Carlo simulation. The sensitivity is limited by systematic errors of the measurement, discussed in Section 5.9. We continue with a *qualitative* discussion of the sensitivity. It is instructive to compare sensitivity of this method with other methods; in particular with two point correlators.

The sensitivity of the method is remarkable indeed if one takes into account that statistics in the fifth multiplicity bin for each of the three event generator points is below 3×10^4 events – too scarce, e.g., to extract three source radius parameters via HBT analysis even with a well optimized spectrometer! In this context, it can be mentioned that sensitivity of HBT interferometry to first order phase transition with droplet hadronization has been discussed [85]; for a hadronization scenario with droplets evaporating *slowly* as they participate in the *transverse flow* of the matter, abnormally large val-

ues of R_{out} are expected. We emphasize that in our approach, we are able to see the signal without such particularities of dynamics. In fact, neither the concept of "slow evaporation" nor that of the transverse flow is present in the event generator we used for this sensitivity study. Another theoretical idea – to use two particle correlation in rapidity $R_2(y)$ to search for droplets – has been discussed in the context of $p\bar{p}$ collisions at $\sqrt{s} = 1.8$ TeV (at FNAL)[86]. The R_2 was reported to *decrease* with multiplicity, so that it would not be expected to be visible for dN/dy above $\approx$20; the signal would be *weaker* in a scenario with correlated droplets.

In the same multiplicity bin, with total number of hadrons at freeze-out around 1.5×10^2, a typical fraction of particles coming from the same fireball for the clustering parameters of 50 would be 3%, and, respectively, 6% for 90. In either case there is little hope of seeing any trace of such dynamics either in ensemble-averaged dN/dy or in dN/dy of a single event.

The data is consistent with clustering parameters below 50. Discussion of the implications of the results presented so far will be carried out separately in the context of the first (Section 6.4) and second order (Section 6.5) phase transition models.

6.4 Discussion: First Order Phase Transition

In 1985, L. Van Hove formulated a model of quark-gluon plasma hadronization [87] which implied very specific experimental signatures observable on EbyE basis. He developed a picture of the hadronization dynamics for a first order phase transition: a QGP cylinder expands longitudinally, until, near transition, its color field assumes a longitudinal topology with strings and color flux tubes. The string network so formed continues stretching, thus slowing down the expansion, while some strings suffer break-up. String breaking creates plasma *droplets*, as large as a few fm across, which no longer expand, but retain the longitudinal motion. They hadronize by *deflagration*[89]. This is expected to result in peculiar bumpy dN/dy distributions.

Mardor and Svetitsky [90] performed a calculation of the free energy of a hadronic gas bubble, embedded in the QGP phase, and of a QGP droplet in a hadronic gas, in the MIT bag model. They found that at temperatures of 150 MeV and below, growth of the hadron gas bubbles (and evaporation of the QGP droplets) becomes irresistible and QGP hadronizes.

In the absence of a direct, event-by-event observable-based test of these predictions, the picture had been further developed [91, 92] in order to connect it with the traditional observables such as the m_T slope parameter T and the

baryon and strangeness chemical potentials: the hadron "temperatures" T in the SPS data are higher than lattice QCD predictions for a phase transition temperature. Using a first order phase transition hydrodynamical model with a sharp front between the phases, Bilic *et al.* [91, 92] concluded that a QGP *supercooling* and hadron gas *superheating* is a consequence of the continuity equations and of the requirement that the entropy be increased in the transition. In the case of bubbles in the QGP phase, the plasma deflagrates; otherwise, it detonates. The statement that a Van Hove type of a hadronization scenario explains some observations is, however, by no means a verification of the hypothesis. An alternative explanation of the high hadron "temperatures" which does not involve overheating is the collective flow [93]. Our dynamic texture measurement tests the *QGP droplet hadronization* hypothesis [87] in a more direct way, because, as we have shown quantitatively, the measurement is sensitive to the presense or absence of the droplets in course of the hadronization (with the necessary caveat that some fraction of the hadronization texture can be washed out by rescattering in the post-hadronization phase [88]). Our result can be used to constrain phenomenological quantities which represent basic QCD properties and affect texture formation in this class of hadronization models [87, 90, 92]. Such quantities are

- the energy flux, or rate at which the QGP transmits its energy to hadrons. The Van Hove hypothesis is based on the estimates of a low flux ($\ll m_\pi/(fm^2 fm/c)$) [94, 95]. If the flux is low, the droplet is preserved until it deflagrates. If the flux is high, the droplet emits mesons continuously as it moves, and the signal is washed out.

- typical initial size of the QGP droplet. At a fixed upper energy density of the transition ϵ_0', this parameter determines the number of hadrons per fireball after hadronization – the "clustering parameter", whose experimental manifestation is explored by Fig.6.5. For the phase transitions *out* of the QGP phase, this parameter will be determined by the percolation of the growing hadron gas bubbles.

- initial upper energy density of the transition ϵ_0'. At a fixed initial size of the QGP droplet, ϵ_0' controls the "clustering parameter" in much the same way as the initial size does.

The event generator results on Fig.6.5 are calculated for pure cases, that is, when all events originate from a parent distribuion with the same clustering parameter. A real situation may well be a combination of a variety of pure cases, for example, the case of a certain mean clustering parameter in x fraction of events, and no phase transition in $1-x$ fraction of events. To conclude this

section, we remark that the operation of the power spectrum averaging over events is linear, therefore in this case

$$P^{\lambda}(m)_{true} = xP_X^{\lambda}(m)_{true} + (1-x)P_0^{\lambda}(m)_{true}. \tag{6.4}$$

Ideally, event mixing should destroy dynamic textures fully, in that case

$$P^{\lambda}(m)_{mix} = P_X^{\lambda}(m)_{mix} = P_0^{\lambda}(m)_{mix} \tag{6.5}$$

It however is not the case if the subevent granularity of the mixing is coarse compared with the correlation length of the dynamic texture. (Spikes which are narrower than pixel size can not be removed by mixing the pixels.) Because only very contrived "dynamic textures" have precise scale localization (a chessboard is an example), Eq.6.5 is merely an approximation in all practical cases. In this approximate sense one can say, based on Eq.6.4 and Eq.6.5, that the DWT dynamic texture of a composite sample is a weighted average of the respective dynamic textures of the component samples. This means that the non-observation of clustering texture signifies smallness of the clustering parameter or rarity of the phenomenon.

6.5 Discussion: Second Order Phase Transition

The specific experimental signature of second order phase transition (known since the discovery of critical opalescence [18]) is the emergence of critical fluctuations of the order parameter with an enormous increase of the correlation lengths. Scalapino and Sugar formulated a statistical theory of multiple particle production in hadron-hadron collisions[14], based on the phenomenological free energy functional of the type used by Ginzburg and Landau [96] to describe the second order phase transition in superconductors. This theory predicts particle emission in clusters, coherently over large rapidity range.

In an SU(2) theory with *massless* u and d and infinitely massive s quark, the phase transition is of second order [100, 101]. SU(3) with three massless quarks results in a fluctuation driven[101] first order [100, 101] phase transition. There are some indications[106], based on lattice QCD work, that for a finite s-quark mass, the phase transition is of second order. Moreover, for a certain class of lattice gauge theories, a tricritical point is expected to exist for a particular coupling strength, separating the first order confinement phase transition from a second order transition with the same critical exponents as the 3D Ising model[100]. In the massless SU(2) case, critical local

fluctuations in the order parameter (which in this case can be parametrized as a four-component $(\sigma, \vec{\pi})$ field) should result in detectable observables: local fluctuations of isospin and enhanced correlation lengths [104]. Possibly, the Centauro event[2] represents just such an occurrence. However, for physical quark masses Rajagopal and Wilczek [104, 105] argued that due to closeness of the pion mass to the critical temperature, it would be unlikely for the correlation volumes to include large numbers of pions, if the cooling of the plasma and hadronization proceeds in an equilibrated manner. If, on the contrary, the high temperature configuration *suddenly* finds itself at a low temperature, a self-organized criticality regime settles in, and the critical local fluctuations develop fully[104, 105].

How can the NA44 experimental data just presented clarify this complex and uncertain picture ? The data signifies absence of dynamical fluctuations on the scales probed (which are the relevant scales), within the limit of sensitivity discussed in Section 6.3. Convincing evidence of thermal equilibration can be provided best by event-by-event observables[6], due to the very nature of the problem. [7] Our data is consistent with local thermal equilibrium, understood as an absence of physically distinguished scales between the scale of a hadron and the scale of the system, or scale invariance of fluctuations [107] ("white noise"). However to *probe* equilibration *directly* with this method, texture sensitivity at least down to the typical fireball (cluster) sizes observed in pN collisions in cosmic rays and accelerator experiments [5, 7] is necessary, but lacking. In the absence of such direct evidence, the non-observation of critical fluctuations can imply either absence of the second order phase transition or thermal equilibration – the latter voids the criticality signature, according to Rajagopal and Wilczek [104].

[6]We include flow observables in the event-by-event class

[7]The NA49 Φ_{p_T} measurement[12] addressed the issue and potentially could have revealed deviations from the local thermal equilibrium. It had, however, no potential of *proving* the equilibrium due to the logical structure of the Central Limit Theorem upon which it rests[107]: zero of the measure follows from the conditions interpretable as consistent with equilibrium – but not other way round.

Chapter 7

Conclusions

This chapter summarizes the main results and conclusions of the thesis.

The single particle measurements of charged kaons and pions (Chapters 3 and 4), and the multiparticle texture analysis (Chapters 5 and 6), both represent searches for hadronic signatures of a phase transition. However they are quite different in terms of the method and, what is more relevant to this chapter, in terms of the physics of the signature.

The strangeness enhancement or, in a more elaborate language, chemical equilibration as a phase transition signature represents an attempt to use hadronic data (highly *compressed* down to the number of particles of certain identity with certain p_T and y, produced per collision) to identify the nature of the degrees of freedom responsible for the hadron production.

The texture signatures of a phase transition exploit analogies between the multiparticle physics of the heavy ion collision and that in the macroscopic condensed matter systems. This is inspired by the notion of universality in the phase transitions, explored with a great success in the condensed matter physics over the past decades. Technically, the texture analysis carried out here relies on the recent advances in the presently booming area of industrially-applicable mathematics of efficient image processing. Here, the "smart" multi-step (multi-scale !) *data compression*[1] itself becomes, in a sense, the process of measurement, and the results of the compression steps throughout the process turn out to be related with the multiparticle degrees of freedom.

[1]The DWT transformation in itself is not yet a compression since the number of expansion coefficients necessary to reconstruct the original image equals the number of original pixels. The common DWT compression techniques are based on suppressing the small expansion coefficients. The power spectrum (used in this work) is based on a summation of squared expansion coefficients and thus, effectively suppresses the impact of the small coefficients by squaring everything, and at the same time reduces the amount of data by the summation.

The results of our research can be summarized as follows:

- a considerable enhancement of K^+ production over π^+ is observed as compared to $p+p$ collisions at the same energy. This is not necessarily a sign of a QGP phase transition: alternative explanations exist, as has been discussed in detail in Chapter 4. In the modern phenomenology, the issue of chemical equilibration, rather than strangeness enhancement by itself, became the subject of investigation. This has also been discussed in Subsection 4.3, and some caveats have been made. Letessier and Rafelski [73] claim on the basis of a statistical model fit to the hadron abundance data that the QGP is formed in the $Pb+Pb$ collisions. The value of our measurement [26] lies in the fact that it provides the quantitative information required for such studies. I believe that the enhanced K^+ production in $Pb+Pb$ should be ascribed to the hadron gas rescattering.

- no signal of non-trivial dynamic texture has been revealed by the Discrete Wavelet Transform analysis of the $Pb+Pb$ data, within the sensitivity limit dominated by systematic errors due to the imperfections of the experimental apparatus. I personally was impressed by the sensitivity of this novel method despite the experimental imperfections. Viewed by this method, the final states of the $Pb+Pb$ collisions appear to be fairly homogeneous, so that if the phase transition takes place, it is either smooth or its effects are moderated by the hadron gas rescattering which then needs to be taken seriously.

Clearly, each of the two results leaves a lot of freedom in the interpretation and they do not contradict each other. Does the "negative" dynamic texture result contradict other CERN data, such as J/Ψ suppression[108], where the strongest claim for the QGP evidence was made ? No, because neither of the results is logically a sufficient condition of existence/non-existence of QGP in the $Pb+Pb$ collisions, and the strongest claim just mentioned in fact merely states that deconfinement is a "natural explanation" of the J/Ψ data.

Finally, I wish to express my intuitive feeling that much of the ambiguities present in the interpretations of the heavy ion data may be a consequence of too high a degree of data compression, applied to made the data analyzable by human brain, following a cultural heritage of the previous epoch of scarce computing power. Consequently, the "smart" compression algorithms, and the analysis techniques based on them, however technical this may sound for the last sentence of a PhD thesis, may well be one of the most promising paths of further development in the heavy ion experiment.

Bibliography

[1] E. L. Feinberg, Sov. Phys. Uspekhi, **14**, 455 (1972).

[2] C. M. Lattes, Y. Fujimoto and S. Hasegawa, Phys. Rep. **65**, 151 (1980).

[3] G. Wataghin, Z. Phys. **88**, 92 (1934).

[4] W. Heisenberg, Z. Phys. **101**, 533 (1936).

[5] G. Cocconi, Phys. Rev. **111**, 1699 (1958).

[6] N. Suzuki, M. Biyajima, A. Ohsawa, Progr. of Theor. Phys., **94**, (1985).

[7] D. Drijard *et al.*, Nucl. Phys. **B155**, 269 (1979).

[8] H. A. Gustafsson *et al.*, Phys. Rev. Lett. **52**, 1590 (1984).

[9] E877 Collaboration, Phys. Rev. Lett. **73**, 2532 (1994). [hep-ex/9405003].

[10] NA49 Collaboration, Phys. Rev. Lett. **80**, 4136 (1998). [nucl-ex/9711001].

[11] N. M. Astafeva, I. M. Dremin and K. A. Kotelnikov, Mod. Phys. Lett. A **12** 1185-1192 (1997); I. M. Dremin, O. V. Ivanov, S. A. Kalinin, K. A. Kotelnikov, V. A. Nechitailo and N. G. Polukhina, Phys. Lett. B **499**, 97 (2001) [hep-ph/0007060].

[12] NA49 Collaboration, Phys. Lett. B **459**, 679 (1999) [hep-ex/9904014].

[13] R. G. Palmer, Adv. Phys. **31**, 669 (1982).

[14] D.J.Scalapino, R.L.Sugar, Phys. Rev. D **8**, 2284 (1973).

[15] P. Carruthers, I. Sarcevic, Phys. Lett. B **189**, 442 (1987).

[16] M.Stephanov, K.Rajagopal, E.Shuryak, Phys. Rev. Lett. **81**, 4816 (1998).

[17] I. Daubechies, Ten Lectures on Wavelets (SIAM, Philadelphia, 1992) and references therein

[18] M. Altschul, Zs. phys. Chem., **11**, 578 (1893); K. von Wesendonck, Naturwiss. Rundschau, **9**, 210 (1894).

[19] J. Pando and L. Fang, Phys. Rev. E **57**, 3593 (1998); L. Fang and J. Pando, astro-ph/9701228.

[20] J.Rafelski, R.Hagedorn, in: Statistical Mechanics of Quarks and Hadrons, ed. H.Satz (North Holland, Amsterdam, 1981).

[21] J.Rafelski, B.Müller, Phys. Rev. Lett. **48**, 1066 (1982).

[22] P. Koch, B. Müller and J. Rafelski, Phys. Rep. **142**, 167 (1986).

[23] S.Z. Belenky, Nucl. Phys. **2**, 259 (1956).

[24] P. Koch and J. Rafelski, Nucl. Phys. **A444**, 678 (1985).

[25] For a recent review of HBT, see: U. Heinz and B. V. Jacak, Ann. Rev. Nucl. Part. Sci. **49**, 529 (1999) [nucl-th/9902020].

[26] NA44 Collaboration, Phys. Lett. B **471**, 6 (1999).

[27] Particle Data Group Collaboration, Phys. Rev. D **45**, (1992).

[28] communicated by A. Franz

[29] N. Maeda *et al.*, Nucl. Instrum. Meth. A **346**, 132 (1994)

[30] E. Beuville *et al.*, Nucl. Instrum. Meth. A **288**, 157 (1990).

[31] E. Chesi, P. Martinengo, Digital Read-out for Analog Multiplexing Signals, CERN, 1988.

[32] T. Akesson *et al.*, Nucl. Instrum. Meth. A **241** 17-42, (1985).

[33] R. Klanner, Nucl. Instrum. Meth. A **235**, 209 (1985).

[34] T. Kobayashi and T. Sugitate, Nucl. Instrum. Meth. A **287**, 389 (1990).

[35] M. Spegel. Cathode Pad Chambers on the Trail of the Quark-Gluon Plasma. Master's Thesis. Institute für Kernphysik, Technische Universität Wien. November 1994.

[36] A. Franz, A. Ljubicic and D. S. Zachary, Nucl. Instrum. Meth. A **384**, 371 (1997).

[37] C. W. Fabjan *et al.*, Nucl. Instrum. Meth. A **367**, 240 (1995).

[38] D. Burckart *et al.*, CERN-ECP-95-012 *Presented at the 9th Conference on Real-Time Computer Applications in Nuclear, Particle and Plasma Physics - RT 95, East Lansing, MI, USA, 23 - 26 May 1995.*

[39] V.B.Berestetsky, E.M.Lifshitz, L.P.Pitaevsky, Quantum Electrodynamics. (any edition).

[40] DECAY TURTLE (Trace Unlimited Rays Through Lumped Elements) - a computer program for simulating charged particle beam transport systems, including decay calculations. Brown, K.L.; Iselin, C.; CERN 74-2. - 5 Feb 1974. - 52 p.

[41] NA49 Collaboration, Nucl. Phys. **A610**, 188c-199c (1996).

[42] H. Dietl et al, Nucl. Instrum. Meth. A **253**, 460 (1987).

[43] Y.Sirois, Ph.D. thesis

[44] Y.Sirois, R.Wigmans. Nucl. Instrum. Meth. A **240**, 262-274 (1985).

[45] R.Hagedorn, Nuovo Cimento Suppl. **3**, 147 (1963); **6**, 311 (1963).

[46] N. K. Glendenning, J. Rafelski, Phys. Rev. C **31**, 823 (1985).

[47] NA44 Collaboration, N. Xu *et al.* Nucl. Phys. **A610**, 175c (1996).

[48] NA44 Collaboration, Phys. Lett. B **388**, 431-436 (1996).

[49] E.Hilf, L.Polley and K.Redlich, Darmstadt Hochschule Preprint (1985)

[50] L. McLerran, Nucl. Phys. A**461**, 245c (1987).

[51] G. Baym, Nucl. Phys. A**479**, 27c (1988).

[52] J. Kapusta and A. Mekjian, Phys. Rev. D **33**, 1304 (1986).

[53] G. I. Kopylov, Phys. Lett. B **50**, 472 (1974).

[54] R.Mattiello *et al.*, Phys. Rev. Lett. **63**, 1459 (1989)

[55] G. A. Milekhin, I. L. Rozental, Sov. Phys. JETP **6**, 154, (1958).

[56] C. Bormann for the NA49 Collaboration, J. Phys. G: Nucl. Part. Phys. **23** 1817-1825, (1997).

[57] H. Sorge, Phys. Rev. C **52**, 3291 (1995); we use version 2.4 of RQMD.

[58] NA49 Collaboration, Phys. Rev. Lett. **82** 2471, (1999).

[59] A. M. Rossi, G. Vannini, A. Bussiere, E. Albini, D. D'Alessandro and G. Giacomelli, Nucl. Phys. B **84**, 269 (1975).

[60] F. Wang for the E-802 Collaboration, in HIPAGS-96 (WSU-NP-96-16); F. Wang, Ph. D. thesis

[61] H. Sorge, Nucl. Phys. **A630**, 522c-534c, (1998).

[62] E866 Collaboration, Nucl. Phys. **A610**, 139c-152c, (1996).

[63] NA44 Collaboration, Phys. Rev. C **59**, 328-335 (1999).

[64] K.Werner, Phys. Rep. **232**, 87 (1993).

[65] WA85 Collaboration, Phys. Lett. B **447**, 178 (1999).

[66] NA49 Collaboration, Phys. Lett. B **444**, 523 (1998).

[67] WA97 Collaboration, Phys. Lett. B **449**, 401-406 (1999).

[68] Heinz Sorge, private communication

[69] WA97 Collaboration, Eur. Phys. J. C**11**, 79 (1999).

[70] F. Wang, H. Liu, H. Sorge, N. Xu and J. Yang, nucl-th/9909001.

[71] J. Ranft, hep-ph/9911213.

[72] U. Heinz and M. Jacob, nucl-th/0002042.

[73] J. Letessier and J. Rafelski, Int. J. Mod. Phys. E**9**, 107 (2000) [nucl-th/0003014].

[74] WA97 Collaboration, Eur. Phys. J. C**14**, 633 (2000).

[75] V.I.Goldanski, Yu.P.Nikitin, I.L.Rosental, Kinematic methods in high energy physics. (English translation exists: Harwood Academic Pub., 1989)

[76] L.D.Landau, J. Phys. USSR, **8**, 201 (1944).

[77] R.M.Sternheimer, Phys. Rev. **145**, 247 (1966).

[78] GEANT. Detector Description and Simulation Tool. CERN Program Library Long Writeup W5013. CN Division, CERN.

[79] F.James. MINUIT. Function Minimization and Error Analysis. CERN Program Library Long Writeup D506. CN Division, CERN.

[80] N. Wiener, Generalized Harmonic Analysis, and Tauberian Theorems (Cambridge, Mass., M.I.T. Press 1966).

[81] G. Uytterhoeven *et al.*, WAILI: Wavelets with Integer Lifting. TW Report 262, Department of Computer Science, Katholieke Universiteit Leuven, Belgium, July 1997.

[82] J.D. Bjorken, Phys. Rev. D **27**, 140 (1983).

[83] Luc Devroye, Non-uniform random variate generation (New York, Springer-Verlag, 1986)

[84] N. Borghini, P. M. Dinh and J. Ollitrault, Phys. Rev. C **62**, 034902 (2000).

[85] G. Bertsch, Nucl. Phys. **A498**, 173c (1989).

[86] P.V. Ruuskanen, D. Seibert, Phys. Lett. B **213**, 227 (1988).

[87] L. Van Hove, Z. Phys. C **27**, 135 (1985).

[88] E. V. Shuryak and M. A. Stephanov, Phys. Rev. C **63**, 064903 (2001). [hep-ph/0010100].

[89] L. Van Hove, Z. Phys. C **21**, 93 (1983).

[90] I. Mardor, B. Svetitsky, Phys. Rev. D **44**, 878 (1991).

[91] N. Bilic *et al.*, Phys. Lett. B **311**, 266 (1993).

[92] N. Bilic *et al.*, Z. Phys. C **63**, 525 (1994).

[93] NA44 Collaboration, Phys. Rev. Lett. **78**, 2080 (1997).

[94] B. Banerjee, N.K. Glendenning, T. Matsui, Phys. Lett. B **127**, 453 (1983).

[95] B. Müller, J.M. Eisenberg, Nucl. Phys. **A435**, 791 (1985).

[96] V.L. Ginzburg, L.D. Landau, Zh. Eksp. Teor. Fiz. **20**, 1064 (1950).

[97] L.D. McLerran, B. Svetitsky, Phys. Lett. B **98**, 195 (1981); Phys. Rev. D **24**, 450 (1981).

[98] J. Kuti, J, Polonyi, K. Szlachanyi, Phys. Lett. B **98**, 199 (1981).

[99] J. Engels, F. Karsch, H. Satz, I. Montray, Phys. Lett. B **101**, 89 (1981).

[100] B. Svetitsky, L. Yaffe, Nucl. Phys. B **210**, 423 (1982).

[101] R. Pisarski and F. Wilczek, Phys. Rep. D **29**, 338 (1989).

[102] T. Hatsuda, T. Kunihiro, Phys. Rev. Lett 55, 158 (1985).

[103] F. Wilczek, Int. J. Mod. Phys. A **7**, 3911 (1992) [Erratum-ibid. A **7**, 6951 (1992)].

[104] K. Rajagopal, F. Wilczek, Nucl. Phys. **B399**, 395 (1993).

[105] K. Rajagopal and F. Wilczek, Nucl. Phys. **B404**, 577 (1993) [hep-ph/9303281].

[106] F.R. Brown *et al.*, Phys. Rev. Lett. **65**, 2491 (1990).

[107] T. A. Trainor, hep-ph/0001148.

[108] NA50 Collaboration, Phys. Lett. B **477**, 28 (2000).

Appendix A

Re-calibrating UCAL to correct for the light absorbtion.

The algebra here provides technical background for the material discussed in 3.4.2. By A and C I denote the amplitude and calibration constant in case of no light absorbtion, and by a and c – the actual ones, respectively. If the light intensity in scintillator gets attenuated with distance x

$$a = Ae^{-x/L},$$

and the scintillator length is S, then the amplitude observed in a single channel (averaged over all positions in x and eliminating the pedestal) is not A as it were in the absence of attenuation, but $a = AL/S(1 - \exp(-S/L))$. Each UCAL tower is served by two PMT tubes, so we have a_1 and a_2; their gains are matched so that $< a_1 >=< a_2 >$. Calibrating a channel [1], I require that

$$(A_1 + A_2)L/S(1 - \exp(-S/L))c = E_0, \tag{A.1}$$

where c is to be determined and E_0 is known. We will denote $(A_1 + A_2)C$ as E_{cal} to indicate that this is the energy observable which we know how to calibrate. [2]

The left and right PMT register the light which passes the distance x and $S - x$, respectively (if the source is point-like). We use the product of the two so that our new observable is

$$E_\times = c\sqrt{A_1 e^{-\frac{x}{L}} A_2 e^{-\frac{S-x}{L}}} = c\sqrt{A_1 A_2} e^{-\frac{S}{2L}} \tag{A.2}$$

[1] in a dedicated run where natural radioactivity of U is measured by the scintillator

[2] if not for the light attenuation, it would have been sufficient.

It is independent of x, but has yet to be calibrated, i.e. related to E_{cal}. Next we notice that $C = cL/S(1 - \exp(-S/L))$ from A.1, and that in the absence of absorption for the gain-matched tubes $\sqrt{A_1 A_2} = (A_1 + A_2)/2$, and therefore

$$E_\times = \frac{\exp(-S/2L)}{2L/S(1 - \exp(-S/L))}(A_1 + A_2)C = \frac{< \sqrt{a_1 a_2} >}{< a_1 + a_2 >}(A_1 + A_2)C, \quad \text{(A.3)}$$

where we recognized that the S and L-dependent prefactor can be expressed in terms of the easily measurable averages. This means that calibration can be restored for the product with the help of the expression:

$$E_\times = \frac{< \sqrt{a_1 a_2} >}{< a_1 + a_2 >} E_{cal} \quad \text{(A.4)}$$

By itself, this result is natural and predictable. Its value lies in the fact that absorbtion length is now related to observables.

Appendix B

Subtracting background effects in the DWT power spectra.

This is a more technical discussion of the problem introduced in Subsection 5.7.2, and the same notation is used. The search for a good background subtraction technique underwent a painfull involution from an ideal, but impossible, to an imperfect, but doable.

Assuming that the interaction signals are a sum of the "physics" signal with the background distributed randomly according to $F(x)$, the three distributions – $F(x)$ (non-interactions), $G(x)$ (minimum bias sample of interactions), and $P(x)$ ("valid beam" (VB) sample) – are related in the following way :

$$P(x) = \alpha \int_{x_{min}}^{x_{max}} F(\xi)G(x-\xi)\, d\xi + (1-\alpha)F(x) \tag{B.1}$$

Due to finiteness of binning, Eq. B.1 is, practically, a system of linear equations:

$$P_x = \alpha \sum_{\xi=x_{min}}^{x_{max}} F_\xi G_{x-\xi} + (1-\alpha)F_x, \tag{B.2}$$

where F,G and P are normalized histograms and x and ξ – discrete indices of bins. [1] In principle, knowing $P(x)$, $F(x)$ and α, one can try to determine $P(x)$ by solving this system of linear equations. Our final goal, however, is correcting the average power spectrum components (PSC).

$$P_x \mathcal{P}_{P,x} = \alpha \sum_{\xi_{min}}^{\xi_{max}} F_\xi G_{x-\xi}(\mathcal{P}_{F,\xi} + \mathcal{P}_{G,x-\xi}) + (1-\alpha)F_x \mathcal{P}_{F,x} \tag{B.3}$$

[1] ξ_{min} and ξ_{max} depend on x and on the choice of binning.

This equation (B.3) reflects the fact that the mean of the PSC distribution from the physics run is the weighted sum of the PSC from the minimum bias interactions and from the empty target, and that in the interaction events, the resulting PSC is a sum of PSCs from "pure" physics and background. Having solved B.1 for $G(x)$, one should solve B.3 for $\mathcal{P}_{G,x}$, whereby the background subtraction problem would be solved.

This is the idealistic approach to background subtraction. It can not be realized in practice because Eq. B.1 – Fredholm's equation of the first kind – is a notorious ill-posed problem, whose solution is, generally, numerically unstable. This means that there is no hope of obtaining a physically meaningful solution to Eq. B.1 in the practical situation with non-zero errorbars. Despite the fact that the solution to Eq. B.1 has been obtained both numerically and using a symbolic processor such as MAPLE, it was of no value because, typically, it was a non-physical oscillating function. Therefore, the following simplfying assumption has been made. The multiplicity binning is coarse enough so that the RMS of the $F(x)$ distribution is only about 1/3 of the bin size. Therefore, approximation of $F(x)$ by a "δ-function" can be easily justified:

$$F_{x-\xi} = \delta_{x,\xi} \tag{B.4}$$

This simplifies the system of equations B.2 to

$$P_x = \alpha G_x + (1-\alpha)\delta_{x,0} \tag{B.5}$$

In other words, the P distribution is obtained from G by increasing the $x = 0$ bin only. Equations B.3 also become simpler, so that the solution for $\mathcal{P}_{G,x}$ is easy:

$$\mathcal{P}_{G,x} = \frac{(1-\alpha)}{\alpha}\frac{\delta_{x,0}}{G_x}(\mathcal{P}_{P,x} - \mathcal{P}_{F,x}) + \mathcal{P}_{P,x} - \mathcal{P}_{F,0} \tag{B.6}$$

Equation B.6 is already simple enough for all bins but one, namely, the zero bin:

$$\mathcal{P}_{G,x} = \mathcal{P}_{P,x} - \mathcal{P}_{F,0} \tag{B.7}$$

This result could have been guessed intuitively. For the zero bin, Eq. B.6 is not useful because G_0 is not known.

Appendix C

Calculus of covariances

Collected here are some identites useful in calculations of covariances between random quantities. Definition:

$$\mathrm{cov}(a,b) = \mathfrak{M}[(a - \mathfrak{M}[a])(b - \mathfrak{M}[b])] = \mathfrak{M}[ab] - \mathfrak{M}[a]\mathfrak{M}[b], \tag{C.1}$$

where the $\mathfrak{M}[\ ]$ is a mathematical expectation operator. By definition of variance $\mathfrak{D}[a]$,

$$\mathfrak{D}[a] = \mathrm{cov}(a,a) \tag{C.2}$$

The following identities are useful :

$$\mathrm{cov}(b,a) = \mathrm{cov}(a,b) \tag{C.3}$$

$$\mathrm{cov}(a,\gamma b) = \gamma \mathrm{cov}(a,b) \tag{C.4}$$

$$\mathrm{cov}(a,c+d) = \mathrm{cov}(a,c) + \mathrm{cov}(a,d) \tag{C.5}$$

Appendix D

Generating sequences of random numbers with a fixed sum.

The multifireball event generator used in Chapter 6 is not a true event generator in the sense that it does not propagate the initial state into a final state. Rather, it generates a final state subject to a set of constraints. The problem, expressed in the header of this Appendix, had to be solved in order to

1. impose momentum conservation on the final states created in the multifireball event generator
2. ensure independency of the event multiplicity on the mean fireball size

Formulation of the problem: generate N random numbers $x_i, i = 1, ..., N$, subject to the condition

$$\sum_{i=1}^{N} x_i = X, \tag{D.1}$$

so that the probability density distribution of an individual x_i approaches given function $f(x)$ (such that $\int_{-\infty}^{+\infty} f(x)\,dx = 1$ and the variance of x is finite) in the limit of large N.

The multivariate probability density distribution can be presented [83] as a product of conditional distributions

$$f(x_1, ..., x_N) = f_1(x_1) f_2(x_2|x_1) f_3(x_3|x_1, x_2) ... f_N(x_N|x_1, x_2, ..., x_{N-1}), \tag{D.2}$$

where, e.g., $f_2(x_2|x_1)$ denotes distribution for x_2 obtained from $f(x_1, ..., x_N)$ if one keeps x_1 fixed at a certain value. In the following, I will deliberately omit the normalization factor. The extra complexity it brings in is not warranted in

this context: you get exactly one random number per subroutine call, therefore normalization factor has no meaning and only the functional shape of the distribution matters. Here $\mathfrak{D}[x]$ is variance of x. For the k-th conditional distribution,

$$\begin{aligned} f_k \quad & (x_k|x_1, x_2, ..., x_{k-1}) \propto \\ \propto \quad & f(x_k) \int \delta(x_1 + x_2 + ... + x_{k-1} + x_k + ... + x_N - X) \prod_{i=k+1}^{N} f(x_i)\, dx_i \propto \\ \propto \quad & f(x_k) \exp\left(-\frac{(\sum_1^{k-1} x_i + x_k + X(N-k)/N - X)^2}{(N-k)\mathfrak{D}[x]} \right) \end{aligned} \tag{D.3}$$

The last transition is based on an (approximate and non-rigorous !) use of the Central Limit Theorem (CLT for short). Indeed, having N numbers x_i distributed according to $f(x)$ with variance $\mathfrak{D}[x]$ and their sum being X, one expects the sum $\sum_{k+1}^{N} x_i$ to be distributed around $X(N-k)/N$, with variance $(N-k)\mathfrak{D}[x]$. Then, x_k (the only free quantity other than $\sum_{k+1}^{N} x_i$) is distributed around $X - x_k - \sum_{k+1}^{N} x_i$ and the same variance, since the total sum is strictly fixed at X. This use of CLT is

- non-rigorous because the CLT is valid for *independently* sampled random numbers – in contradiction with Eq. D.1.
- approximate because the CLT is a *limit* of large N.

From the practical point of view, these caveats mean that for small N, the generated distribution of x may deviate from $f(x)$ somewhat. Nevertheless this technique accomplishes its goal whereas its approximate nature is of no concern for the application in question.